Summer 2020

A 3D Image-Guided System to Improve Myocardial Revascularization Decision-Making for Patients with Coronary Artery Disease

Haipeng Tang

A 3D IMAGE-GUIDED SYSTEM TO IMPROVE MYOCARDIAL REVASCULARIZATION DECISION-MAKING FOR PATIENTS WITH CORONARY ARTERY DISEASE

by

Haipeng Tang

A Dissertation
Submitted to the Graduate School,
the College of Arts and Sciences
and the School of Computing Sciences and Computer Engineering
at The University of Southern Mississippi
in Partial Fulfillment of the Requirements
for the Degree of Doctor of Philosophy

Approved by:

Chaoyang Zhang, Committee Chair
Weihua Zhou
Huiqing Zhu
Bikramjit Banerjee
Robert Bober
Zhaoxian Zhou

August 2020

ABSTRACT

OBJECTIVES. Coronary artery disease (CAD) is the most common type of heart disease and kills over 360,000 people a year in the United States. Myocardial revascularization (MR) is a standard interventional treatment for patients with stable CAD. Fluoroscopy angiography is real-time anatomical imaging and routinely used to guide MR by visually estimating the percent stenosis of coronary arteries. However, a lot of patients do not benefit from the anatomical information-guided MR without functional testing. Single-photon emission computed tomography (SPECT) myocardial perfusion imaging (MPI) is a widely used functional testing for CAD evaluation but limits to the absence of anatomical information. Therefore, the integration of SPECT-MPI and fluoroscopy angiography becomes necessary to guide MR. This study aims to develop a 3D image-guided system that integrates fluoroscopy angiography with SPECT-MPI to improve MR decision-making.

METHODS. Major coronary arteries on fluoroscopy angiograms were extracted with a deep learning-based image segmentation model and then reconstructed into 3D artery anatomy using computer stereo geometry calibration and reconstruction algorithms. 3D LV epicardial surface was extracted from SPECT-MPI using a dynamic programming-based algorithm. Artery-surface fusion was completed with non-rigid registration based on a scaling iterative closest points (S-ICP) algorithm and post-processing techniques based on a line-surface overlay algorithm. The accuracy of artery-surface fusion was evaluated via both computer simulation and real patient data. For technical evaluation, simulated fluoroscopy angiograms and nuclear myocardial perfusion images were integrated using the reconstruction and fusion approaches and then validated against the digital X-CAT

phantom. For clinical validation, computed tomography (CT) angiograms were used as the ground truth: LV & right ventricular (RV) epicardial surfaces and arteries were manually extracted on CT angiograms and then registered with the SPECT epicardial surfaces; the locations of fluoroscopic and CT arteries on the SPECT epicardial surface were compared and evaluated.

RESULTS. In the technical evaluation, the distance-based mismatch error between simulated fluoroscopy and phantom arteries is 1.86±1.43 mm for left coronary arteries (LCA) and 2.21±2.50 mm for right coronary arteries (RCA). In the clinical validation, thirty patients with coronary artery disease (CAD) were enrolled. The mean distances between the fluoroscopic and CT arteries were 3.84 ± 3.15 mm for LCA and 5.55 ± 3.64 mm for RCA. The concordance between the fluoroscopic and CT arteries in the clinical 17-segment model agreed well with a Kappa value of 0.91 (95% confidence interval (CI): 0.89 to 0.93) for LCA and a Kappa value of 0.80 (95%CI: 0.67 to 0.92) for RCA.

CONCLUSION. A 3D image-guided system for MR decision-making has been developed that reconstructs 3D arterial anatomy from fluoroscopy angiograms, extracts LV epicardial surface from SPECT myocardial perfusion images, and fuses the arterial anatomy with LV epicardial surface. The system is technically accurate to guide MR decision-making and clinically feasible to be used in the catheterization laboratory. With the precise integration of anatomical and physiological information, it has a great promise to improve the decision-making and outcome of MR in clinic practice.

Keywords: myocardial revascularization; fluoroscopy angiography; myocardial perfusion imaging; image fusion

ACKNOWLEDGMENTS

I would like to thank Dr. Chaoyang Zhang, Dr. Weihua Zhou, and all the other committee members, Dr. Huiqing Zhu, Dr. Bikramjit Banerjee, Dr. Robert Bober, and Dr. Zhaoxian Zhou for their suggestions and advice to improve my work during the whole process. I gratefully acknowledge both of my advisors, Dr. Zhang and Dr. Weihua Zhou, for their generous help in the past four and a half years. Along the path of research that has led to this dissertation, they have constantly been there to provide me guidance, support, and suggestions. I also would like to thank Dr. Huiqing Zhu, Dr. Bikramjit Banerjee, Dr. Robert Bober, and Dr. Zhaoxian Zhou for their technical support of algorithm development, and clinical support of high-quality data and clinical advice during my doctoral research.

I am forever indebted to my family, who have been extremely supportive and helpful. I am grateful to my mother and mother in law who help take care of my baby daughter, which enabled me to put more focus on my dissertation research. I am also grateful to my sweet daughter who is always clever and obedient. I am especially grateful to my wife, Xiaohui Liu, for her endless love, support, and encouragement.

TABLE OF CONTENTS

LIST OF TABLES

LIST OF ILLUSTRATIONS

LIST OF ABBREVIATIONS

LV	Left ventricular
SPECT	Single-photon emission computed tomography
PET	Positron emission tomography
SA	Short axis
VLA	Vertical long axis
HLA	Horizontal long axis
RV	Right ventricle
LA	Left atrium
RA	Right atrium
LCA	Left coronary artery
RCA	Right coronary artery
LMA	Left main artery
LAD	Left anterior descending artery
LCX	Left circumflex artery
D1	First diagonal branch artery
D1_b1	Branch of first diagonal branch artery
D2	Second diagonal branch artery
D3	Third diagonal branch artery
SEP1	First septal perforator branch artery
SEP2	Second septal perforator branch artery
SEP3	Third septal perforator branch artery
OM1	First obtuse marginal artery

OM2	Second obtuse marginal artery
OM3	Third obtuse marginal artery
OM4	Fourth obtuse marginal artery
RI	Ramus intermedius artery
PDA	Posterior descending artery
PLB	Posterior lateral branch artery
PLB1	First branch of posterior lateral branch artery
RMA	Right marginal artery
CAD	Coronary artery disease
MR	Myocardial revascularization
PCI	Percutaneous coronary artery intervention
CABG	Coronary artery bypass graft
CT	Computed tomography
ICP	Iterative closest point
AIV	Anterior interventricular vein
CS	Coronary sinus vein
GCV	Great cardiac vein
MCV	Middle cardiac vein
CMR	Cardiovascular magnetic resonance imaging
CT	Computed tomography
FCN	Fully convolutional networks
LAO	Left anterior oblique
RAO	Light anterior oblique

CRA	Cranial
CAU	Caudal
SID	Source to image distance
SOD	Distance between source to the object
LM	Levenberg-Marquardt
OSEM	Ordered subset expectation maximization
DP	Dynamic programming
SVD	Singular value decomposition
PTCA	Percutaneous transluminal coronary angioplasty
ESV	End-systolic volume
EDV	End-diastolic volume

CHAPTER I – INTRODUCTION

1.1 Clinical background in myocardial revascularization

1.1.1 Coronary artery disease and MR decision making

Coronary artery disease (CAD) is the most common type of heart disease and kills over 360,000 people a year in the United States[1][2]. Pathologically, it is the narrowing or blockage of coronary arteries and usually caused by the buildup of cholesterol and fatty deposits (called plaques) on the inner walls of the arteries[3][4][5]. Once the narrowing or blockage is formed, the blood flow to the heart muscle is physically clogged and decreased. Without an adequate blood supply, the heart muscle becomes starved of oxygen and the vital nutrients that it needs to work properly, which is also known as myocardial ischemia. Several mild or non-obstructive CAD symptoms, chest pain or shortness of breath, may present. If blood and muscle of heart have a long-term supply/demand mismatch, a stable CAD may happen. Stable CAD is defined as an established pattern of angina pectoris, a history of myocardial infarction, or the presence of plaque documented by catheterization[6]. Almost 17 million patients in the United States have stable CAD and nearly 800,000 more will experience an initial event each year[7]. All the stable CAD patients require effective medical treatments to alleviate symptoms, prevent cardiovascular events, and reduce mortality.

Myocardial revascularization (MR) is a standard interventional treatment for patients with stable CAD, which includes two major surgeries: percutaneous coronary artery intervention (PCI) and coronary artery bypass graft (CABG)[8][9][10]. PCI is a cardiological procedure used to treat narrowing of the coronary arteries, as shown in *Figure 1.1A*. The process involves combining coronary angioplasty with stenting that is the

insertion of a permanent wire-mesh tube inside the artery. A stent delivery balloon from an angioplasty catheter is inflated at the narrowed position to force contact between the struts of the stent and the vessel wall so that the clogged artery is opened to relieve the narrowing and improve the blood flow[11][12]. CABG (*Figure 1.1B*) is a surgical procedure that improves the blood flow to the heart through grafting a vessel from left internal thoracic to the left anterior descending (LAD) branch of the left coronary artery (LCA). Another approach of CABG cuts a length of great saphenous vein from a leg and then grafts it from aorta or its major branches to the obstructed artery to restore the blood flow[13][14][15].

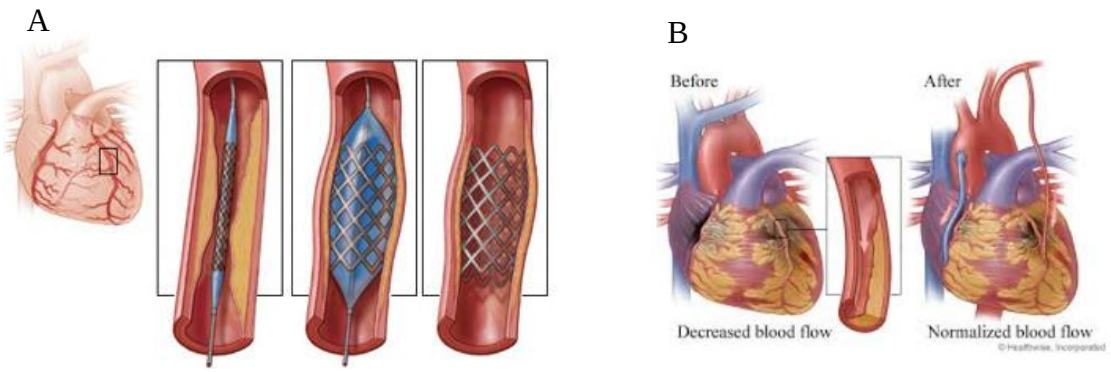

Figure 1.1 *Two types of myocardial revascularization (MR).*

(A) Percutaneous coronary intervention (PCI); (B) coronary artery bypass grafting (CABG). Figure A and B are cited from [16] and [17], respectively.

In the clinic, however, not all stable CAD patients benefit from MR. A bunch of patients after MR do not improve their heart function or might even get worse because of the restenosis and inflammation caused by the stent[18][19]. It is quite difficult to make an MR strategy for stable CAD patients between MR+medical therapy and medical therapy alone. Boden et al. [20] conducted a randomized trial involving 2287 patients who were divided into 1149 individuals undergone PCI with optimal medical therapy and 1138

individuals received optimal medical therapy alone. The result showed that PCI did not reduce the risk of death compared to optimal medical therapy alone. Frye et al. [21] assigned 2368 patients to undergo either prompt revascularization with intensive medical therapy or intensive medical therapy alone. The result exhibits that there was no significant difference in the rates of death and major cardiovascular events between patients undergoing prompt revascularization and medical therapy. Velazquez et al. [22] randomly divided 1212 patients into 610 individuals with medical therapy+CABG and 602 individuals with medical therapy alone. The result demonstrates that there was no significant difference between medical therapy plus CABG and medical therapy alone with respect to the primary endpoint of death.

All these clinical trials made MR decision based on the visually estimated percentage stenosis of arteries during fluoroscopy angiography (red arrows in *Figure 1.2A&B*). It has been proved unhelpful to improve MR decisions because the visual estimation cannot always necessarily reflect the real function stenosis. A lot of patients show critical vascular stenosis on fluoroscopy angiograms but the corresponding myocardium (heart muscle) has normal perfusion by functional testing, which leads to the huge increasing number of unnecessary treatments with percutaneous coronary stent transplant. Therefore, functional testing prior to the MR is necessary to correctly estimate the myocardial viability so as to improve the MR decision for patients with stable CAD.

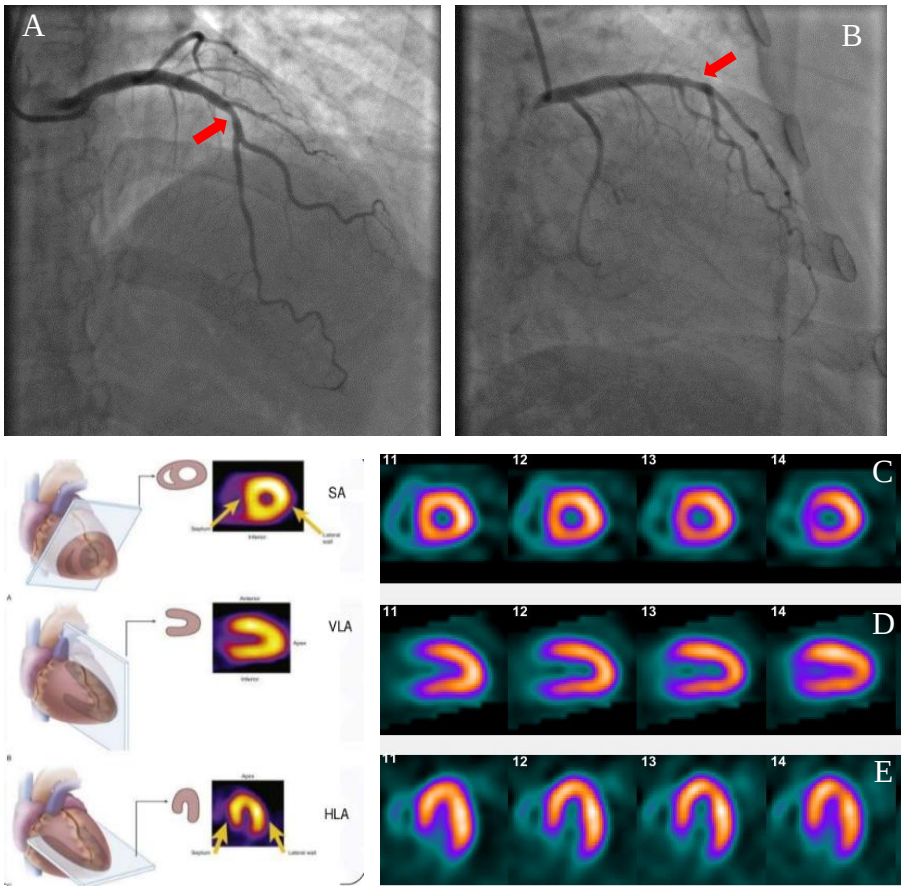

Figure 1.2 *Fluoroscopy angiograms and single-photon emission computed tomography (SPECT) images.*

(A) An angiogram from the view of LAO 0˚ and CRA 33˚; LAO = left anterior oblique, CRA = cranial. (B) An angiogram from another view of RAO 31˚ and CAU 22˚; (C) SA SPECT image, SA = short-axis slice. (D) VLA SPECT image, VLA = vertical long axis. (E) HLA SPECT image, HLA = horizontal long axis.

1.1.2 Myocardial functional testing for MR decision

Single-photon emission computed tomography (SPECT) myocardial perfusion imaging (MPI) is a non-invasive functional test for the assessment of myocardial viability[23][24]. It is the most commonly used to evaluate myocardial damage and assess the presence and the extent of myocardial ischemia[25][26]. In the procedure of SPECT MPI, a radioactive tracer is injected into the bloodstream and then taken by the myocardium, reflecting the

myocardial perfusion and viability[27]. Higher tracer uptake stands for higher myocardial viability, which shows lighter areas on the SPECT images. Being functional testing, SPECT MPI shows which areas of the heart muscle are supplied with blood and which areas are ischemic. If the arteries show severe narrowings in fluoroscopy angiography but the corresponding myocardial areas show normal perfusion, patients may not benefit from MR compared with using medicine alone. This shows mismatched information between SPECT MPI and fluoroscopy angiography. On the other hand, if myocardium show both ischemic on SPECT images and severe stenosis on fluoroscopy angiograms, patients can benefit from MR. This shows matched information between SPECT MPI and fluoroscopy angiography. The functional information of the myocardium is an important factor in MR decision-making.

Several studies have demonstrated that MR decisions based on MPI improved morbidity over anatomical assessment or medical therapy alone[28][29][30]. These trials assessed patients' risk stratification based on functional/physiological testing, and found that high-risk stable CAD patients benefited from MR decided on the basis of myocardial ischemic extent on SPECT-MPI. Moreover, it was also demonstrated that normal MPI, revascularization in stable CAD conferred a higher risk of all-cause death[31]. SPECT-MPI can identify revascularization candidates for patients with stable CAD and improve mortality and cardiac outcomes after MR.

However, SPECT MPI can only exhibit myocardial information but miss anatomical information, which means the severity and distribution of artery stenosis are invisible on SPECT images. Therefore, in order to improve MR decision, the arterial anatomical information from fluoroscopy angiograms needs to be integrated with myocardial

functional information from SPECT-MPI. In clinical practice, fluoroscopy angiography and SPECT MPI are performed independently and the data are in two dimensions (2D and 3D, shown in Figure 1.2), therefore, image datasets are clinically segregated. Physicians have to mentally combine the information of artery stenosis from angiograms with that of myocardial perfusion from SPECT. Obviously, mental integration of the 2D coronary arteries projection images with the slice-by-slice myocardial perfusion images is difficult, imprecise, and non-reproducible. The MR decision based on mental 2D-3D integration may fail to make.

Image fusion techniques based on computer vision have great promise to address this issue, which precisely integrates the 2D-3D modalities for physicians to improve MR decisions for patients with stable CAD.

1.2 Review of fusion techniques for left ventricular (LV) epicardial surface and coronary vessel anatomy

Over the past decade, several fusion techniques for coronary vessels and LV surface were developed and validated. They registered either arteries or veins with LV surface for clinical applications[32][33]. All the techniques were in three categories: landmark-based, standard iterative closest point (ICP), and deep learning-based methods.

1) Landmark-based method. According to the characteristics of coronary anatomy[34], LAD/anterior interventricular vein(AIV) travels in the anterior interventricular groove on LV surface, proximal left circumflex artery(LCX)/coronary sinus(CS) connected to great cardiac vein(GCV) lies in the left atrioventricular groove, and posterior descending artery(PDA)/middle cardiac vein(MCV) travels in the inferior interventricular groove. A

landmark-based method was to minimize these curve pairs to complete the registration of these two modalities. Faber et al. [35] used the landmark-based method to fuse the SPECT LV epicardial surface with 3D arterial anatomy by minimizing the distances between landmark point pairs on the epicardial surface and on the venous anatomy. Zhou et al. [36] applied a similar landmark-based method to the fusion of LV epicardial surface and 3D venous anatomy. In both studies, two drawbacks may affect the accuracy of LV surface-vessels fusion. First, both coronary veins and arteries have complicated anatomical structures with many branches and extensions. Landmark-based method can only align the major landmark points such as AIV, CS and MCV in venous system or LAD, LCX and PDA in arterial system. However, the branches and extensions of the major vessels may not be accurately aligned, which may affect the accuracy of image fusion. Second, a pair of scale-matched venous anatomy and LV epicardial surface is essential but difficult to obtain.

2) Standard ICP method. ICP is an algorithm employed to minimize the difference between two point clouds. It is a rigid transformation algorithm and widely used for registration of two objects[37]. Faber et al. [38] introduced an improved ICP to fuse 3D coronary arterial anatomy with LV epicardial surface. In that study, they used the geometrical properties of a star-shaped surface in spherical coordinates to search for the closest points in each iteration of ICP, which consequently accomplished a more accurate and efficient registration than the standard ICP. Babic et al. [39] used a standard ICP algorithm to fuse LV epicardial surface with a coronary venous tree. Toth et al. [40] used Go-ICP[41] to complete the multi-modality fusion of LV epicardial surface with venous anatomy. The Go-ICP encapsulates two branch & bounds (BnB) algorithms and the

standard ICP to implement globally optimized registration, where outer BnB operates on the rotation space SO(3) and the inner BnB operates on translation space R^3.

Nevertheless, both standard ICP and the improved ICPs mentioned above are rigid registration algorithms that require a pair of scale-matched point-cloud models. Actually, in cardiovascular imaging, it is quite difficult to obtain a pair of scale-matched models because coronary vessels and epicardial surface are separately obtained at different time points. In order to solve this problem, studies often selected the end-diastolic frame of fluoroscopic venograms and end-diastolic LV epicardial surface for further registration. Toth et al. [40] applied a principal component analysis based approach [42] to estimate the end-diastolic frame of fluoroscopic venograms and then aligned the fluoroscopic frame to the end-diastolic epicardial surface from cardiovascular magnetic resonance imaging. Zhou et al. [36] visually estimated the end-diastolic frame of fluoroscopic venograms and then registered the fluoroscopic frame with the end-diastolic epicardial surface from gated MPI. However, all these approaches cannot guarantee a pair of size-matched objects. The accuracy of image fusion may decrease or the fusion may fail when two objects have a significant scale mismatch. Therefore, a non-rigid registration that can automatically match the scales of objects is important.

3) Deep learning-based method. Toth et al. [43] used the reinforcement learning to register 2D coronary vessels with 2D projection of epicardial surface from computed tomography (CT) images. They formulated the registration task as an imitation learning problem. Agent's steps were modeled as Markov decision process. At a certain time step, the agent was in a single state (alignment) and its action was rewarded depending on a better or worse alignment by the action. The goal was to learn a policy (registration

strategy) that can predict optimal registration actions with the highest reward. This agent was modeled using a pair of convolutional neural networks (CNN) for encoding and another neural network for decoding with the features from encoding. 802 projections of CT LV volumes and corresponding X-ray images were split to 702 for training and 100 for test. The evaluation result showed good accuracy with the 2D registration error of 2.92± 2.22 mm.

However, this deep learning-based method mapped 3D LV volume onto 2D image and completed a 2D registration with X-ray images. It cannot show 3D anatomical structures of LV epicardial surface and coronary vessels. Due to the complex overlaps of vessels on 2D coronary angiograms, doctors prefer a 3D artery anatomy fusion with LV surface to better exhibit the stenosis of arteries from any views. Therefore, a 3D non-rigid registration of LV surface and coronary vessels are still necessary to guarantee precise image fusion for guiding MR.

1.3 Innovations and significance and this project

In this dissertation project, an image-guided system was developed to complete the fusion between coronary artery anatomy and LV surface (artery-surface fusion). The image-guided system includes three major steps: 1) reconstruction of 3D arterial anatomy from fluoroscopy angiograms; 2) extraction of LV epicardial surface from SPECT images; 3) non-rigid registration of arterial anatomy with SPECT LV surface.

In the reconstruction of 3D arterial anatomy, a mathematic model was developed using the principles of X-ray angiography and pinhole camera models[44][45]. An imaging geometry calibration algorithm was implemented and improved to optimize the parameters

of angiography system. A total of 15 intrinsic and extrinsic parameters were optimized with the calibration algorithm. Theoretically, the more parameters are calibrated, the more accurate artery reconstruction is. Compared to current calibration methods[46], the proposed method calibrated the most parameters so that the geometry system was more accurately optimized and the arterial anatomy was more accurately reconstructed. Besides, an epipolar constraint-based algorithm was implemented to create the correspondence between the projection points on primary and secondary angiograms. In order to avoid multiple correspondences, dynamic programming was used to optimize the correspondences. All these implemented or improved algorithms ensured accurate reconstruction of 3D arterial anatomy, which is essential to the artery-surface fusion.

In the extraction of LV epicardial surface, a dynamic programming-based algorithm[47] was improved to obtain LV epicardial surface, which extracted a more accurate LV surface compared to the conventional model-based method. The improvements included a more accurate strategy to sample LV myocardial regions using a dynamic programming-based method and a better method to extract LV myocardial surfaces.

In the fusion between arterial anatomy and LV surface, an accelerated non-rigid registration algorithm (scaling iterative closest points: S-ICP) was developed to complete the registration of these two modalities. Compared to the landmark-based method mentioned in Section 1.2, S-ICP aligned all the vessels with the LV surface instead of major vessels, which enhanced the accuracy of the registration. Compared to the regular ICP, S-ICP adjusted the scale of 3D arterial anatomy model up to or down to the optimal scale and then registered it with the 3D LV epicardial surface model by minimizing the squared distance between the two models. It solved the problem that LV epicardial surface

has a mismatch with the scale of arterial anatomy caused by the separate image acquisitions at different time points of cardiac beating.

Besides the technical innovations and improvements, the developed 3D image-guided system has an extremely important impact on MR decision makings in clinical practice. MR based on fluoroscopic angiography shows limitations due to visually estimated stenosis, absence of myocardial function information, and artery overlaps. SPECT MPI can assist angiographer to make decisions based on accurate functional information but limits to the absence of arterial anatomical information. Therefore, the fusion between fluoroscopy angiograms and SPECT MPI images integrates functional and anatomical information to help physicians target lesion vessels and make more accurate MR decisions. The outcomes of MR will be improved for patients with stable CAD.

Moreover, this artery reconstruction, surface extraction, and fusion techniques can also be applied to other 2D/3D fusion scenarios between functional and anatomical imaging, such as SPECT/PET-vein, CT-fluoroscopy arteries, CT-SPECT/PET, CMR-fluoroscopy angiograms/venograms, etc. All these multi-modality fusion can offset mutual weaknesses and provide complementary information for more accurate diagnosis in the clinic.

1.4 Dissertation Organization

Figure 1.3 illustrates the workflow of this study. First, coronary arteries were segmented from fluoroscopy angiograms and reconstructed into 3D arterial anatomy. A computer simulation was executed to evaluate the accuracy of 3D artery reconstruction. Second, LV epicardial surface was extracted from SPECT MPI images. The accuracy of LV extraction algorithm was evaluated using another computer simulation. Third, the 3D arterial anatomy

was fused with the LV epicardial surface using S-ICP registration and vessel-surface overlay algorithms. The fusion approach was validated using computer simulation and real patient data. In the validation with patient data, CT epicardial surface and artery centerlines were manually extracted from CT angiograms and then registered with the SPECT epicardial surface so that the distances between fluoroscopy and CT arteries were computed to validate the accuracy of this artery-surface fusion.

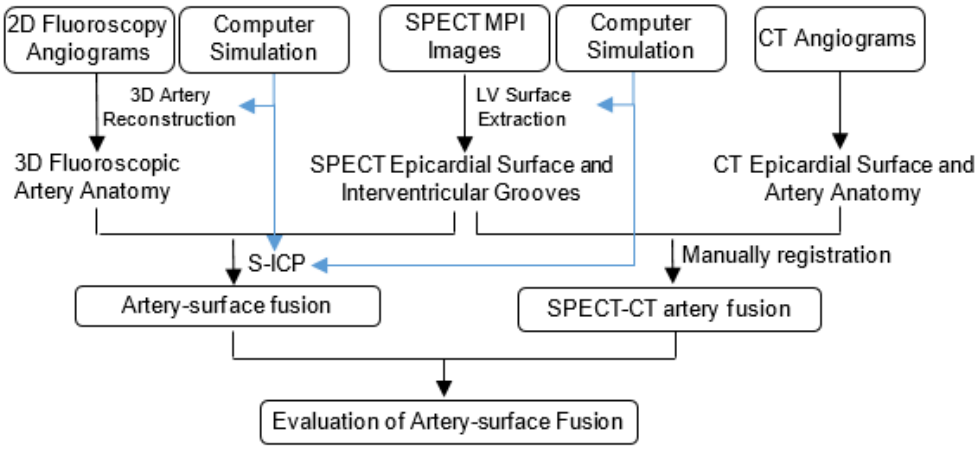

Figure 1.3 *Workflow of the Artery-Surface Fusion and Validation*

Specifically, this dissertation is organized as follows: In Chapter 2, I introduce the reconstruction of 3D arterial anatomy, including artery segmentation, centerline extraction, imaging geometry calibration, centerline reconstruction, and artery contour construction. I then introduce a computer simulation to evaluate the accuracy of the reconstruction approach.

In Chapter 3, I discuss the extraction of LV epicardial surface using a dynamic programming based-algorithm, and then introduce smoothing and rendering methods of LV epicardial surface. A computer simulation is finally introduced to evaluate the accuracy of the extraction approach.

In Chapter 4, I present the fusion between arterial anatomy and LV surface using a non-rigid registration algorithm, and then discuss the evaluation of the fusion approach using computer simulation. Moreover, in order to validate the clinical feasibility of this fusion approach, a clinical feasibility test using 30 patients' data is introduced.

In Chapter 5, I complete the dissertation by summarizing and concluding my work and providing a set of issues appropriate for future work.

CHAPTER II –RECONSTRUCTION OF 3D ARTERIAL ANATOMY

This chapter outlines the procedures to reconstruct 3D arterial anatomy from 2D fluoroscopy angiograms, including 2D image segmentation, imaging geometry calibration, artery reconstruction, and accuracy validation via computer simulation. Section 2.1 introduces the segmentation of fluoroscopy angiograms using deep learning techniques. Section 2.2 explains the mathematic modeling of fluoroscopy angiography system and the imaging system calibration by optimizing an objective function consisting of 15 intrinsic and extrinsic parameters. Section 2.3 discusses an epipolor constrain-based method to pair vessel points from primary and secondary views and then demonstrates the reconstruction of 3D arterial anatomy. Finally, Section 2.4 presents the validation of calibration and reconstruction algorithms using simulated fluoroscopy angiograms with GATE 8.2.

2.1 Coronary artery segmentation and centerline extraction on fluoroscopy angiograms

2.1.1 Artery segmentation using deep learning

It has been a challenging problem to extract vessel contours and structures from fluoroscopy angiograms for many years because of the following reasons: (1) the images are usually low contrast because of limited radiation dosage or time exposure, (2) the structure of vessel tree is complicated and deformable, (3) there are too many overlaps between vessels, (4) bones or pace-maker devices usually creates unpredictable shadows diluting contrast agent or blocking out the region of interest (ROI).

Traditional methods for vessel segmentation have been proposed [48][49] and can be classified as follows[50]–[53]: pattern recognition approach, model-based approach,

tracking and propagation-based approach, and tube-like object detection approach, etc. The pattern recognition method uses morphology filters[54]–[56] and multiscale hessian-based filters[57] to detect objects. The model-based method sets initial pixels as seed and then the vessel tree structure grows according to the seeds and specific rules, such as brightness selection rule, expert tracing, etc. The tracking and propagation-based method uses a set of parametric curves to segment vessels, such as active contour and spline models. All these traditional image processing based methods are not accurate and robust enough when working on the low contrast angiograms.

Recently, 2D/3D image segmentation based on deep learning approaches attracts researchers' attention because of the outstanding performance in natural and medical image segmentation tasks. Among all the deep learning segmentation models, end-to-end segmentation neural network frames, such as fully convolutional networks (FCN) and U-net, have shown state of the art in medical image segmentation work.

In this project, a deep learning model with Unet++[58] frame, was trained to segment coronary arteries on fluoroscopy angiograms. A dataset containing 314 fluoroscopy angiograms was used to train the model. The data was divided into 251 and 63 images for training and test, respectively. All the images with a pixel size of 512×512 were pre-processed with top-hat and N4 bias correlation to enhance the contrast. Data augmentation was used to enhance the performance of the model, which randomly rotates images from -30˚ to 30˚ and randomly flips the images around vertical and horizontal axes. The model was trained via Adam optimizer[59] with a batch size of 1, an epoch of 1000, a learning rate of 0.0001, and a decay rate of 0.05. The dice score of the trained model was 0.87 evaluated using 5-fold cross-validation. The probability map created by the trained model

was post-processed with OTSU[60] to generate binary segmentation images. Accordingly, given a fluoroscopy angiogram, coronary arteries were extracted, as shown in *Figure 2.1*.

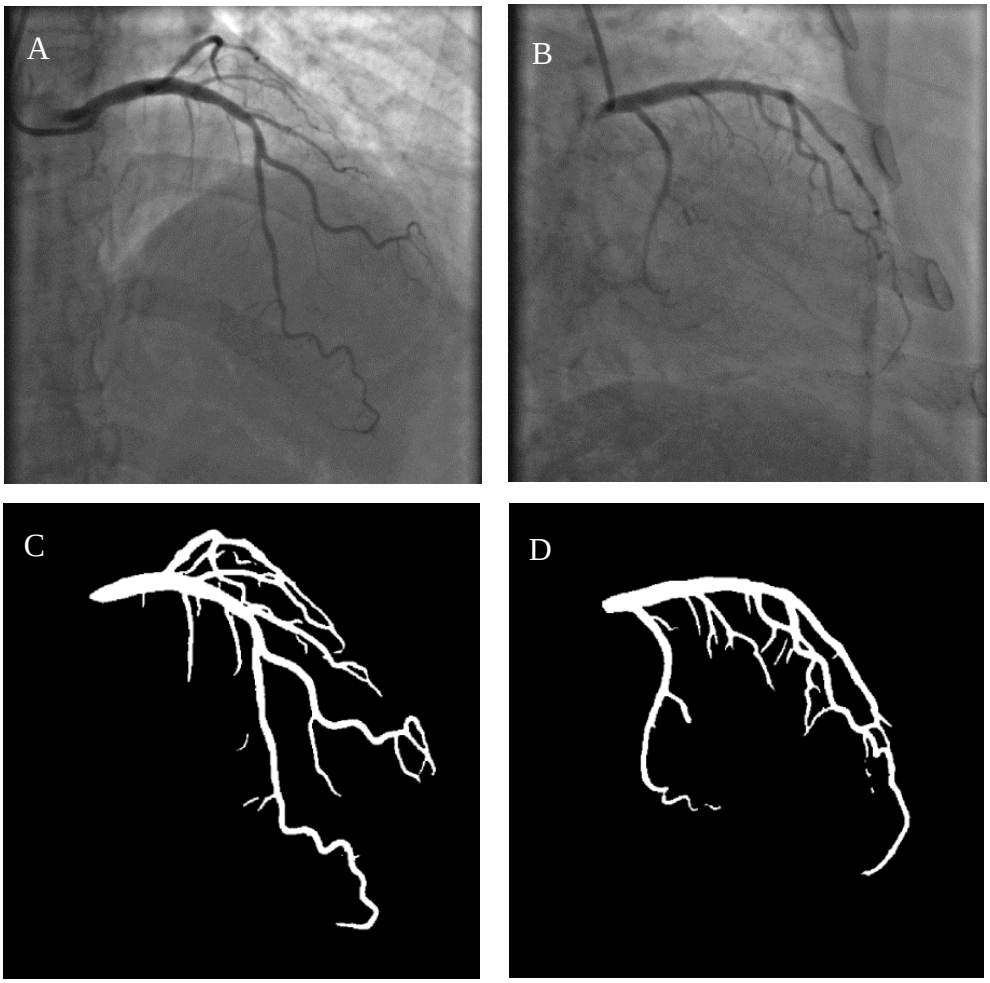

Figure 2.1 *Artery segmentation using deep learning techniques.*

(A) and (B) angiograms from two projection views; (C) and (D) Vessels extracted from the angiograms;

2.1.2 Vessel skeletonization and topology structure

In order to reconstruct arterial anatomy, it is necessary to extract arterial centerlines from the segmented artery contours. Centerlines or skeleton concisely represent the geometric topology of arteries[61]. Each point on the centerlines is at the same distance from two

points on the artery boundary on the segmentation image, so that the 3D arterial anatomy can be reconstructed based on the arterial centerlines and diameter of contour.

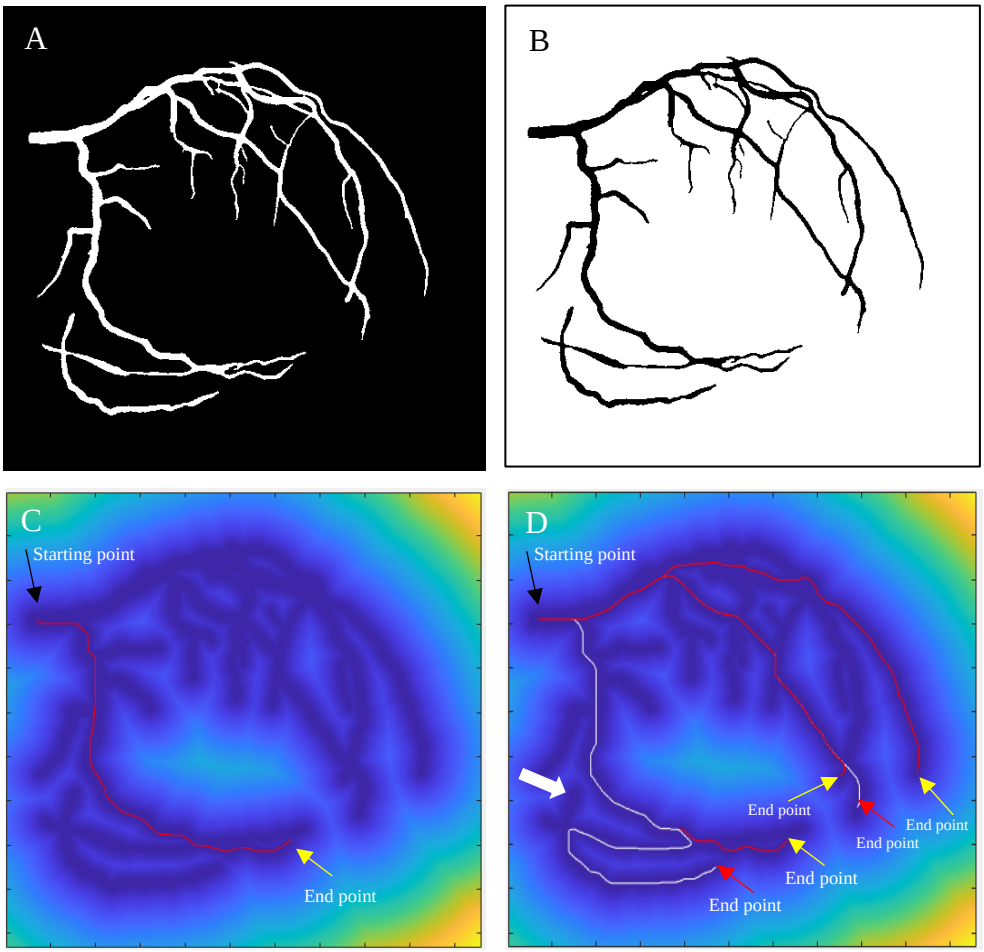

Figure 2.2 *Centerline extraction using minimum-path based algorithm.*

(A) Binary segmentation of artery tree on fluoroscopy angiogram. (B) Inversed binary image. (C) Extracted centerline (red line) using minimum-path based algorithm with given starting and end points. (D) Extracted centerlines with the same starting point and different end points; red lines are appropriately extracted centerlines, white lines are inappropriately extracted centerlines.

Extracting centerlines (or skeletonization) is a process for reducing foreground regions in a binary image to a skeletal remnant that largely preserves the extent and connectivity of the original region while throwing away most of the original foreground pixels. The

existing centerline extraction approaches can be classified as minimum path-based algorithms (fast marching)[62] and morphological thinning-based approaches[63].

I tested the feasibility of the minimum path-based algorithm. A centerline distance map was first generated by calculating the distance between pixels on the binary segmentation mask (*Figure 2.2B*). On the distance map, smaller values were assigned to the pixels closer to centerline whereas larger values were assigned to the pixels farther away from the centerline. A pair of starting and end points were manually specified. A minimal distance path from starting to end points was generated as centerline, as shown in *Figure 2.2C*. However, the overlaps between arteries are very complicated, which screw up the blood vessel paths (*Figure 2.2D*). The minimum distance path cannot represent the path because of the overlaps and disconnections on the map, as the white arrow in *Figure 2.2D*. Another issue is that this algorithm cannot guarantee an exact centerline, which means the extracted centerline points may not exactly be at the same distance from the arterial boundaries.

On the other hand, the morphological thinning algorithm is an operation that iteratively erodes pixels from the boundary of the object in binary images until the topology of the object remains unchanged[64][65]. This approach keeps the whole connectedness of the vessels and acquires accurate centerlines. Therefore, I applied the morphological thinning based method for centerline extraction. The thinning algorithm was related to a hit-and-miss transformation and could be expressed as the following operation:

Thinning (I, f) = I – hit-and-miss (I, f)

, where the subtraction is a logical subtraction defined by $X - Y = X \cap NOT\ Y$.

The thinning operation was operated by subtracting the image by a hit-and-miss transformation from the original image I. This operation was iteratively executed to erode

the boundaries of the vessels until it did not locally split local vessel points into two parts. Therefore, the arterial centerlines were extracted, as shown in *Figure 2.3*.

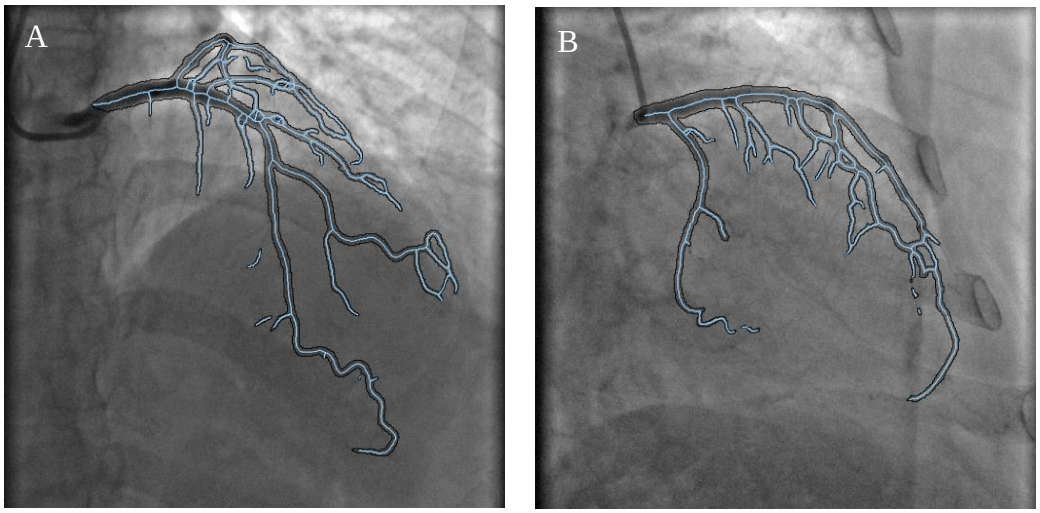

Figure 2.3 *Centerline extraction using a morphological thinning-based algorithm.*

(A) Extracted centerline on an angiogram from primary view. (B) Extracted centerline on an angiogram from secondary view.

The obtained vessel centerlines were pixel-wise points without topology structure. A semi-automatic approach was developed to complete the artery topology. An edge linking algorithm[66] was applied to link the separate skeleton pixel points, where adjacent skeleton pixel points were linked together to form vessel segments till encountering edge junctions or endpoints. The vessel segments were manually selected via a developed interactive tool to construct complete centerlines of major arteries (*Figure 2.4A*). Therefore, the centerlines of major arteries on the primary and secondary projection views were identified and paired. The topology of the arterial anatomy was then automatically established. LAD and LCX were intersected at the distal left main artery (LMA). LAD connected with its branches, including the first diagonal branch (D1), the second diagonal branch (D2), the third diagonal branch (D3), the first septal perforator branch (Sep1), the

second septal perforator branch (Sep2), etc. LCX connected with its branches, including the first obtuse marginal branch (OM1), the second obtuse marginal branch (OM2), the third obtuse marginal branch (OM3), etc. Base on the artery topology, bifurcations between the arteries were automatically identified, as shown in *Figure 2.4B.*

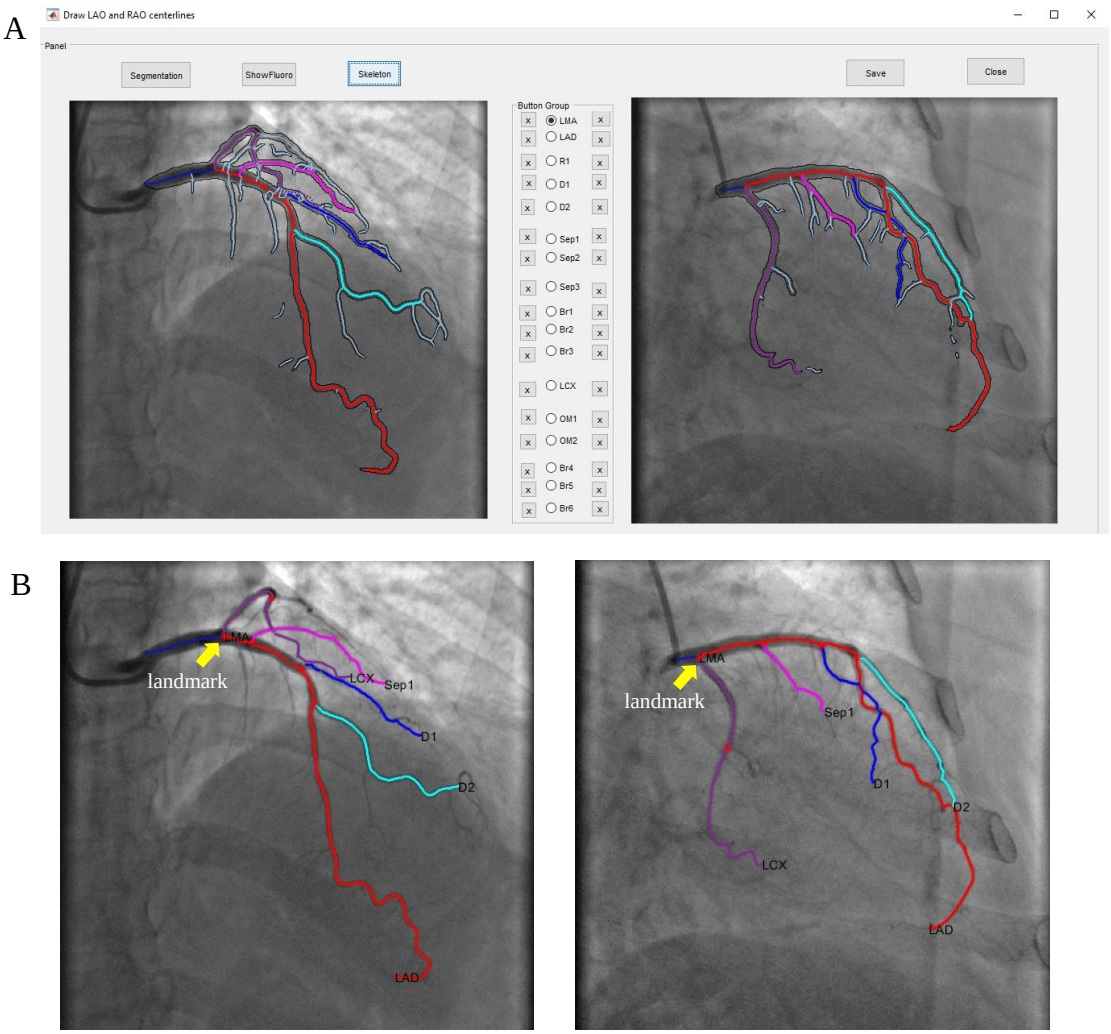

Figure 2.4 *Graphical user interface to complete vessel topology and generate landmarks.*

(A) User interface to manually click and select centerline segments (light blue lines) to identify vessels for topology. (B) Automatically generated bifurcations as landmarks (red stars) for further imaging geometry calibration.

After extracting centerlines, diameters of the arteries were then obtained using morphological operations. Each centerline point saved its coordinate values (x, y) and corresponding diameter (d).

2.2 Imaging geometry calibration of the angiography system

2.2.1 Create a mathematic model based on angiography system

The fluoroscopy angiography device is a complicated mechanical system consisting of X-ray source and image detector mounted on a mobile C-arm gantry, as shown in *Figure 2.5*. The C-arm gantry rotates along the x-axis to reach left anterior oblique (LAO) or right anterior oblique (RAO) view, and rotates along the y-axis to reach cranial (CRA) or caudal (CAU) view. The patient table translates in the x, y, and z directions to target the desired positions. Based on the angiography system, a mathematic model was created with following parameters: α is defined as LAO or RAO angle, β as CRA or CAU angle, source to image distance (SID) as the distance between the X-ray source center (*F*) to the image detector center (*O*), source to object center (*I*, also as known as ISO center) distance (SOD) as the distance between the X-ray source to the object, and column & row directions as u & v in the image coordinates. All these imaging geometry parameters can be classified into two types: extrinsic and intrinsic parameters. Extrinsic parameters are related to rotations (α, β) and translations (x, y, z) of the gantry in the angiography system with respect to the world coordinates. Intrinsic parameters, similar to the pinhole camera model [44][45], create the relationship between camera coordinates and pixel coordinates in the image frame. The extrinsic and intrinsic parameters create the relationship between the patient and the X-ray-detector coordinate system.

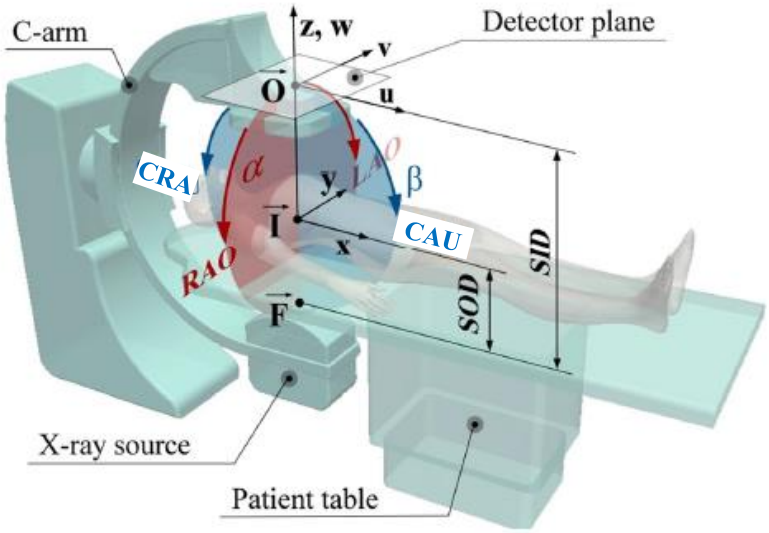

Figure 2.5 *System of fluoroscopy angiography*[67].

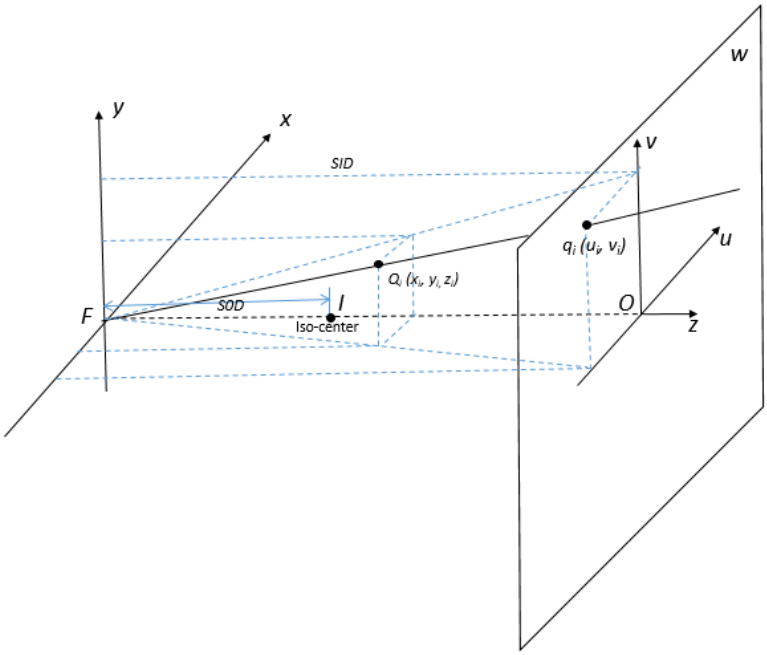

Figure 2.6 *Imaging model of monoplane angiography system*

The geometry of angiography system for a single view is shown in *Figure 2.6*. *F* is the origin of the world coordinates with respect to x, y and z directions, *I* is the isocenter referred as the rotation center of the gantry, and *O* is the center of the detector in the image coordinates (also known as principal point). A vessel centerline point $Q_i(x_i, y_i, z_i)^T$ is

projected onto detector *w* and intersected to the point $q_i(u_i, v_i)^T$. According to the triangle similarity theorems, the relationship between the point Q_i and q_i can be formulated as

$$\begin{aligned} SID \cdot \frac{x_i}{z_i} + u_c &= u_i \\ SID \cdot \frac{x_i}{z_i} + v_c &= v_i \end{aligned} \qquad \textit{Eq.1,}$$

where u_c and v_c are the center coordinates of the detector. Since the *Eq.1* is not convenient to compute, the homogeneous matrix is introduced to simplify the computation. With the homogeneous vectors of $Q_i(x_i, y_i, z_i, 1)^T$ and $q_i = (u_i, v_i, 1)^T$, *Eq.1* can be expressed as *Eq.2*:

$$\begin{bmatrix} \frac{SID}{\alpha_u} & \frac{SID}{\alpha_u} \bullet s & u_c & 0 \\ 0 & \frac{SID}{\alpha_v} & v_c & 0 \\ 0 & 0 & 1 & 0 \end{bmatrix} \begin{bmatrix} x_i \\ y_i \\ z_i \\ 1 \end{bmatrix} = (u_i, v_i, 1)^T \qquad \textit{Eq.2,}$$

where α_u and α_v are the pixel sizes of angiogram in u and v directions respectively, $\frac{SID}{\alpha_u} \bullet s$ is the radial distortion factor. *Eq.2* then can be decomposed as *Eq.3*, where *M* is defined as the intrinsic matrix of the angiography system, *[I|0]* is defined as an extrinsic matrix consisting of a 3×3 identity matrix *I* and a 3×1 zero vector 0, and P_1 is the projection matrix from 3D spatial point to 2D point on the detector. The intrinsic matrix *M* describes a geometric property of the angiography system and consists of a sequence of shear, scaling, and translation transformations, as shown in *Eq.3*. It defines the mapping between the vessels and X-ray detector coordinate system.

$$q_i = \begin{bmatrix} \frac{SID}{\alpha_u} & \frac{SID}{\alpha_u} \bullet s & u_c \\ 0 & \frac{SID}{\alpha_v} & v_c \\ 0 & 0 & 1 \end{bmatrix} [I|0]\, Q_i = M\, [I|0]\, Q_i = P_1 Q_i \qquad \textit{Eq.3}$$

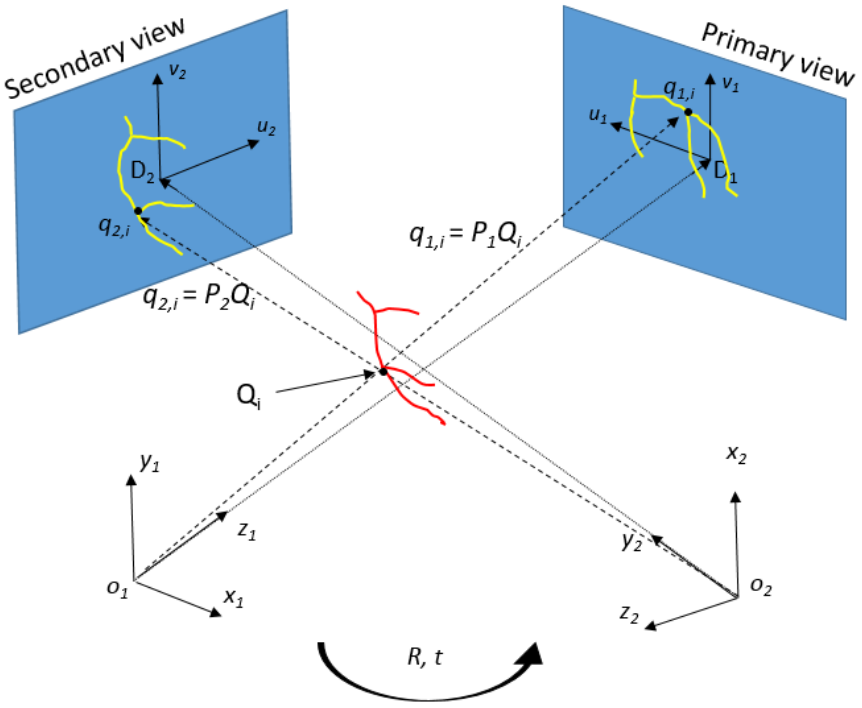

Figure 2.7 *Spatial relationship between the primary and secondary views.*

When another projection view is considered, in *Figure 2.7*, the geometry of the angiography system consists of primary and secondary projections with a relationship of rotation R and translation t. Suppose the gantry rotates along x_1 & y_1 axes and generates α_1 & β_1 angles in the primary camera coordinates, and the gantry similarly generates α_2 & β_2 with the rotations along x_2 & y_2 axes in the secondary camera coordinates. The extrinsic parameters, describing the spatial relationship between the primary and secondary coordinate frames, can be derived by a 3×3 rotation matrix R (*Eq.4*) and a 3×1 translation vector t (*Eq.5*). Therefore, based on the intrinsic and extrinsic parameters of the primary and secondary coordinates, the projection points ($q_{1,i}$ and $q_{2,i}$) of a spatial point Q_i on the primary and secondary detectors can be formulated as *Eq.6* and *Eq.7*, where M_1 and M_2 are

the intrinsic parameters, *[I|0]* and *[R|t] are* the extrinsic parameters for the primary and secondary coordinates respectively.

$$R = R_x(\alpha_1)R_y(\beta_1)R_y(-\beta_2)R_x(-\alpha_2) \qquad Eq.4$$

$$t = [0 \quad 0 \quad SOD_1]^T - R[0 \quad 0 \quad SOD_2]^T \qquad Eq.5$$

$$q_{1,i} = \begin{bmatrix} \frac{SID_1}{\alpha_u} & \frac{SID_1}{\alpha_u} \bullet s & u_c \\ 0 & \frac{SID_1}{\alpha_v} & v_c \\ 0 & 0 & 1 \end{bmatrix} [\, I \mid 0 \,]\, Q_i = M_1\, [I|0]\, Q_i = P_1 Q_i \qquad Eq.6$$

$$q_{2,i} = \begin{bmatrix} \frac{SID_2}{\alpha_u} & \frac{SID_2}{\alpha_u} \bullet s & u_c \\ 0 & \frac{SID_2}{\alpha_v} & v_c \\ 0 & 0 & 1 \end{bmatrix} [R \mid t \,]\, Q_i = M_2\, [R \mid t]\, Q_i = P_2 Q_i \qquad Eq.7$$

Therefore, given the extrinsic and intrinsic parameters of the primary and secondary views, projection matrixes P_1 and P_2 define the mapping between a spatial vessel point and the projection points on the primary and secondary detectors. As shown in *Figure 2.7*, $q_{1,i}$ and $q_{2,i}$ are the projection points of the Q_i by the P_1 and P_2. Since the projection point (P_1Q_i) of Q_i is coincident with $q_{1,i}$, the cross product $q_{1,i} \times P_1Q_i$ is equal to $\vec{0}$ and therefore the *Eq. 8* can be derived, where p_a^{bT} is the *bth* row of the projection matrix P_i, a = [1, 2], b = [1, 2, 3]. Similarly, $q_{2,i} \times P_2Q_i$ is equal to $\vec{0}$ and *Eq.9* can be formulated. Then, *Eq. 8* & *Eq. 9* are combined to derive *Eq.10*. Since Q_i is a 1×4 homogeneous vector with three unknowns(x_i, y_i, z_i), *Eq.10* is an overdetermined equation. Least squares method can be used to find the optimal approximation solution. Therefore, given a pair of 2D vessel points from the primary and secondary views, a 3D vessel point is reconstructed using this mathematic model.

$$\left.\begin{aligned} u_{1,i}(p_1^{3T}Q_i) - (p_1^{1T}Q_i) &= 0 \\ v_{1,i}(p_1^{3T}Q_i) - (p_1^{2T}Q_i) &= 0 \\ u_{1,i}(p_1^{2T}Q_i) - v_{1,i}(p_1^{1T}Q_i) &= 0 \end{aligned}\right\} \quad Eq.8$$

$$\left.\begin{aligned} u_{2,i}(p_2^{3T}Q_i) - (p_2^{1T}Q_i) &= 0 \\ v_{2,i}(p_2^{3T}Q_i) - (p_2^{2T}Q_i) &= 0 \\ u_{2,i}(p_2^{2T}Q_i) - v_{2,i}(p_2^{1T}Q_i) &= 0 \end{aligned}\right\} \quad Eq.9$$

$$\begin{bmatrix} u_{1,i}p_1^{3T} - p_1^{1T} \\ v_{1,i}p_1^{3T} - p_1^{2T} \\ u_{2,i}p_2^{3T} - p_2^{1T} \\ v_{2,i}p_2^{3T} - p_2^{2T} \end{bmatrix} Q_i = 0 \quad Eq.10$$

2.2.2 Create an objective function for imaging geometry calibration

I have created a mathematical model that can reconstruct the 3D vessel points using the intrinsic and extrinsic parameters. However, the intrinsic and extrinsic parameters read from DICOM image files are not optimal to reconstruct 3D vessels. There are several major reasons: (1) the angiography system is mechanically unstable because of variant mechanical nature of device or different assembly tolerances[68]; (2) certain intrinsic parameters, such as skew factor and the coordinates of the principal point, are unknown; (3) the isocenters of primary and secondary camera coordinates are not exactly coincident with each other; (4) table translation during image acquisition introduces errors. All these

factors can lead to inaccurate or failed reconstruction, especially table translation that frequently happens during imaging.

Therefore, a geometry calibration is necessary to optimize the extrinsic and intrinsic parameters. Based on Yang's method[45], I proposed a calibration algorithm that can calibrate 15 extrinsic and intrinsic parameters including α_1, β_1, α_2, β_2, t_x, t_y, t_z, m_x, m_y, m_z, SID_1, SID_2, u_c, v_c, and s. An objective function aiming to optimize the 15 parameters was first created, and then a nonlinear optimization algorithm was used to minimize the objective function to obtain optimal extrinsic and intrinsic parameters.

$$\arg\min F\left(SID_1, SID_2, s, u_c, v_c, \alpha_1, \beta_1, \alpha_2, \beta_2, \overline{t_x}, \overline{t_y}, \overline{t_z}, \overline{tm_x}, \overline{tm_y}, \overline{tm_z}\right)$$

$$= \sum_{i=1}^{n} \left[sqrt(u_{1,i} - P_1 Q_i)^2 + sqrt(u_{2,i} - P_2(Q_i + \overline{tm}))^2 \right]$$

$$+ \overline{w} \sum_{j=1}^{n-1} \left[\left\| \frac{u_{1,j} - u_{1,j-1}}{\|u_{1,j} - u_{1,j-1}\|} - \frac{P_1 Q_{1,j} - P_1 Q_{1,j-1}}{\|P_1 Q_{1,j} - P_1 Q_{1,j-1}\|} \right\|^2 \right.$$

$$\left. + \left\| \frac{u_{2,j} - u_{2,j-1}}{\|u_{2,j} - u_{2,j-1}\|} - \frac{P_2(Q_{2,j} + \overline{tm}) - P_2(Q_{2,j-1} + \overline{tm})}{\|P_2(Q_{2,j} + \overline{tm}) - P_2(Q_{2,j-1} + \overline{tm})\|} \right\|^2 \right] \quad Eq.11$$

Using bifurcations as calibration landmarks (*Figure 2.4*), the objective function was to reduce the following two mismatch errors, as shown in *Eq.11*. The first error was the point transfer error, which was the Euclidean distance between the artery bifurcations and the corresponding back projections of reconstructed 3D bifurcations on each of the primary and secondary images. The second error was the algebraic transfer error of the direction vectors. Since every two adjacent vessel points along the vascular path determined a vector, the number of direction vectors for n bifurcations was n-1. The algebraic transfer error was

represented as the square difference between the directional vectors defined by artery bifurcations and the corresponding back projections of reconstructed 3D bifurcations on each of the primary and secondary images. In *Eq.11*, both P_1 and P_2 consists of $SID_1, SID_2, s, u_c, v_c, \alpha_1, \beta_1, \alpha_2, \beta_2, \overline{t_x}, \overline{t_y}, \text{ and } \overline{t_z}$ (as shown in *Eq. 6* and *Eq.7*). $\overline{tm}$ is a 3×1 vector to offset the normal error caused by unpredictable table panning and unavoidable patient translation during image acquisition.

2.2.3 Optimize the objective function

A nonlinear optimization algorithm, Levenberg-Marquardt (LM) [69], was used to optimize the objective function *Eq.11*. LM algorithm is a robust and rapid convergent algorithm to solve non-linear least square problems. With initialization parameters obtained from the DICOM header, LM optimizer minimized the objective function to obtain optimal intrinsic and extrinsic parameters. Hence, the imaging geometry calibration of the fluoroscopy angiography system was completed.

2.3 Pair vessel points and reconstruct 3D centerlines

In order to reconstruct 3D vessel centerlines, the point correspondences on the primary and secondary views must be established. As shown in *Figure 2.8*, a point m_1 of vessel LAD on the primary image should have a corresponding point m_2 on the secondary image. However, it is not easy to identify the corresponding point, especially for the vessels with open endings (red arrows in *Figure 2.8*). This section introduces a point-to-point pairing method using an epipolar constraint-based method, and also introduces the reconstruction of 3D vessel centerlines using paired vessel points on both views.

2.3.1 Pair vessel points with an epipolar constraint-based approach

Since the imaging geometry of angiography system was well calibrated as mentioned in Section 2.2.3, the spatial relationship of centerline points on the primary and secondary met epipolar constraints[66][67] and therefore the correspondence could be created. According to the epipolar constraints, as shown in *Figure 2.9*, the X-ray source O_1, X-ray source O_2, and one of the vessel points m_1 on the primary view determined a plane, which was epipolar plane (yellow plane). This epipolar plane intersects with the secondary projection plane to determine a line l, which is the epipolar line. Then the intersection point m_2 between the epipolar line l and vessel curve was the correspondence of the vessel point m_1.

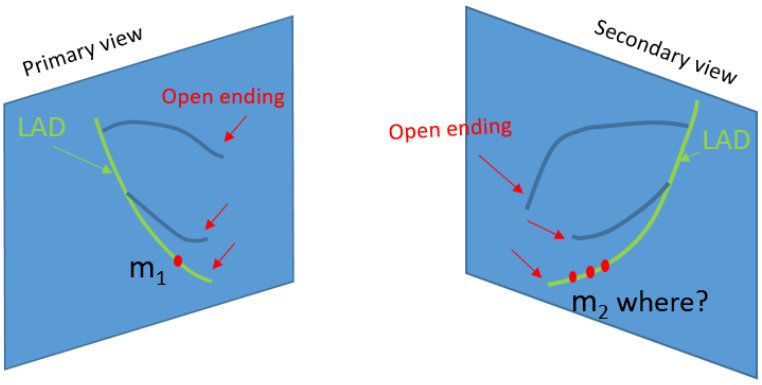

Figure 2.8 *Correspondences of vessel points on primary and secondary views*

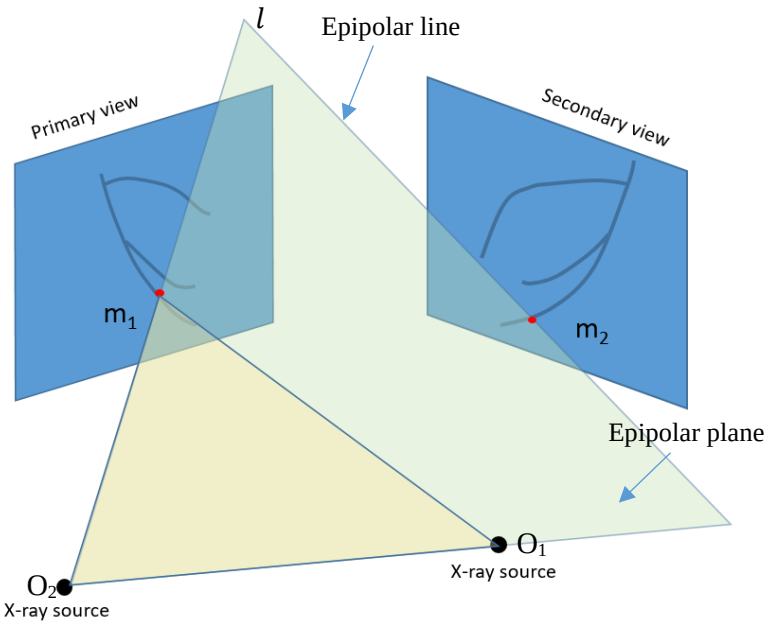

Figure 2.9 *Paring vessel points with the Epipolar constraint*

For each vessel, the point numbers of projection centerlines on the primary and secondary images are different, as the LAD shown in *Figure 2.8*. The centerline with fewer points was first interpolated with the same number of points as the longer one. Then, the centerline paths on the primary and secondary views were defined by an ordered set of m points $P = [u_1, u_2, u_3, \ldots u_m;\ (i = 1{:}m)]$ and $S = [v_1, v_2, v_3, \ldots v_m; (j = 1{:}m)]$, respectively. According to the epipolar constraints, $[u_1, u_2, u_3, \ldots u_m;\ (i = 1{:}m)]$ should be corresponded with $[v_1, v_2, v_3, \ldots v_m; (j = 1{:}m)]$ in sequential order along the path. However, it was not guaranteed that the centerline points P were perfectly matched with S in some cases, especially the vessel with complicated curves, the epipolar line might have multiple matchings with vessels in the second view. In order to solve this problem, a dynamic programming-based approach was used to optimize the pairing. For each point

u_i, the matching v_j should lie on or be the nearest to the epipolar line defined by u_i, X-ray source O_1 and O_2. The distance of v_j from the epipolar line is defined as matching error. All the matching errors of $v_1, v_2, v_3, \ldots v_m$ were computed and saved in $T_{m\times m}[Dis_{ui}, Dis_{vj}]$ matrix. So the optimal correspondence should have the path with the minimum sum of errors through the matrix $T_{m\times m}$. Dynamic programming algorithm was used to find the minimum cost path as shown in *Figure 2.10B.*

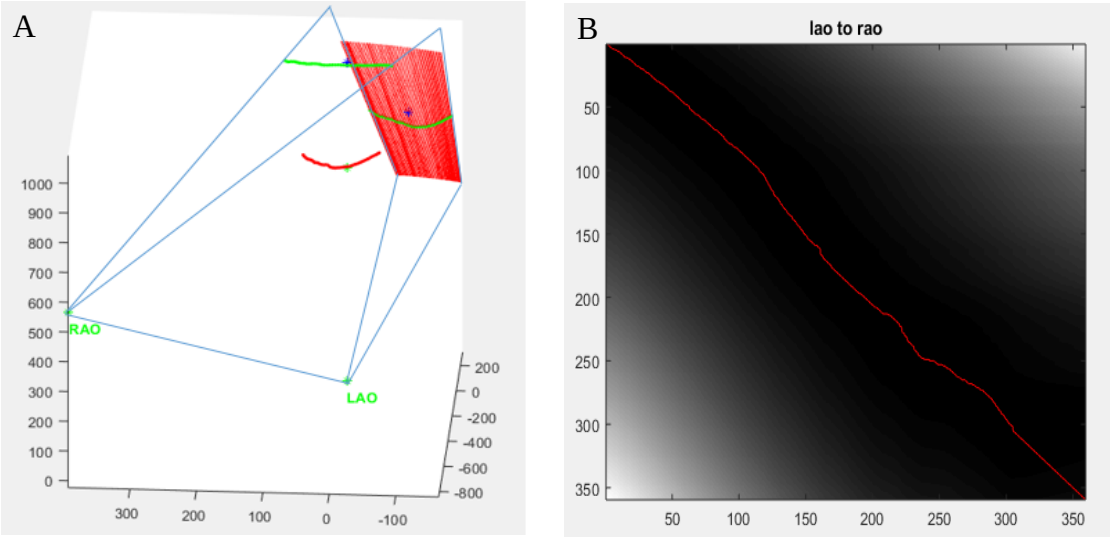

Figure 2.10 *Pairing vessel points optimized by a dynamic programming algorithm.*

(A) Blue plan is epipolar plan, straight red lines are epipolar lines, and green curves are vessel centerlines from primary and secondary views. (B) Mismatch error map *T* and optimal path (red line). Darker areas mean smaller errors.

2.3.2 Reconstruct 3D artery centerlines and render artery contours

Based on the calibrated geometry system and paired centerline points on both views, 3D vessel centerlines were reconstructed using the mathematic model created in Section 2.2.1. Given a pair of points $q_1(u_{1,i}, v_{1,i})$ and $q_2(u_{2,i}, v_{2,i}), i \in [1, n]$, the spatial centerline point $Q_i(x_i, y_i, z_i, 1)$ was computed by solving the overdetermined equation (*Eq.11*)

consisting of optimized projection matrixes P_1 and P_2, where $opt\_p_a^{bT}$ is the *bth* row of the projection matrix P_i, a = [1, 2], b = [1, 2, 3]. *Figure 2.11A* shows the reconstructed 3D artery centerlines.

$$\begin{bmatrix} u_{1,i}opt\_p_1^{3T} - opt\_p_1^{1T} \\ v_{1,i}opt\_p_1^{3T} - opt\_p_1^{2T} \\ u_{2,i}opt\_p_2^{3T} - opt\_p_2^{1T} \\ v_{2,i}opt\_p_2^{3T} - opt\_p_2^{2T} \end{bmatrix} Q_i = 0 \qquad \textit{Eq.11}$$

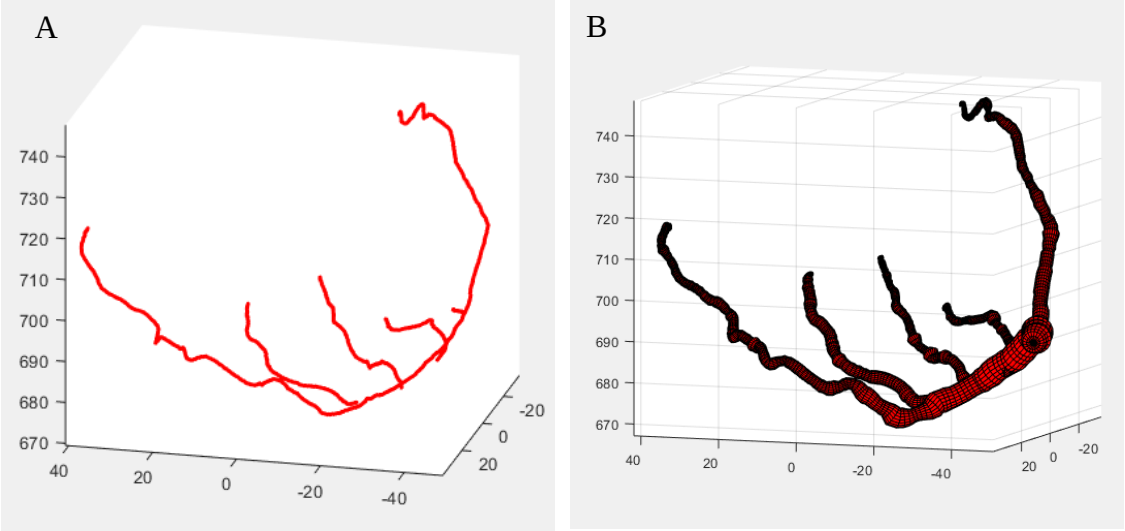

Figure 2.11 *Centerline reconstruction and contour rendering.*

(A) Reconstructed artery centerline. (B) Mesh artery surface using quadrangles.

As mentioned in Section 2.1.2, the diameters (d) of each centerline point along the vascular curve on the primary and secondary views were computed, respectively. The longer centerline on either primary or secondary image indicates fewer overlaps and exhibits clearer diameter information. For instance, in *Figure 2.4B*, LAD in the primary image better shows anatomical structure than it in the secondary image. Accordingly,

lengths of each vessel on the primary and secondary views were compared and the longer one was used to render 3D vessel contour.

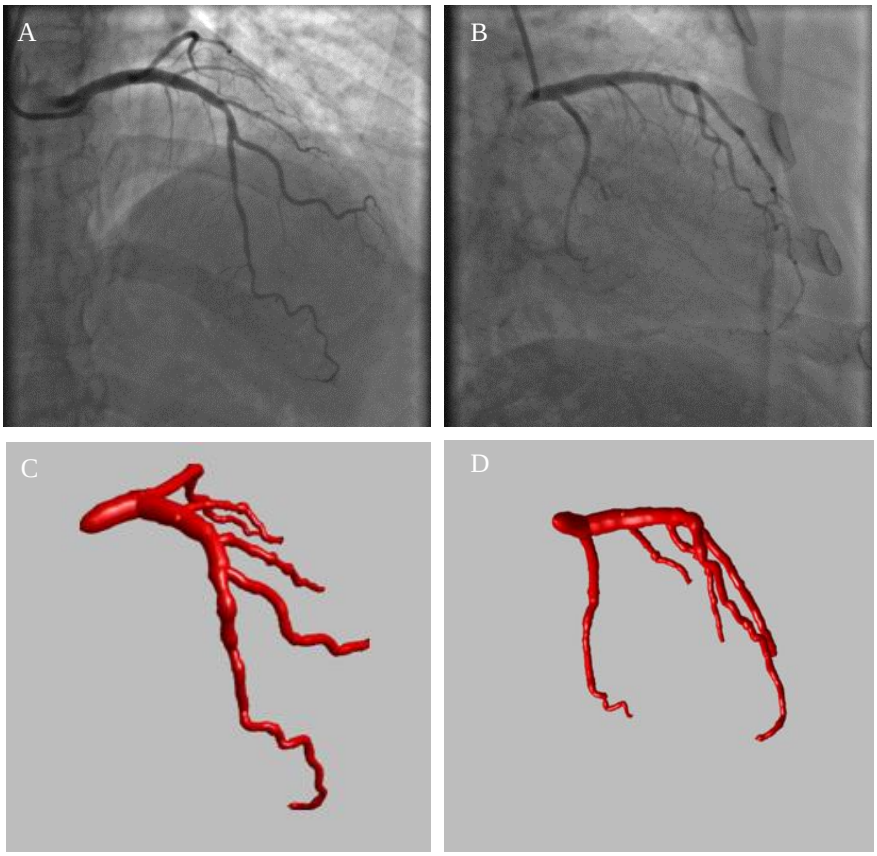

Figure 2.12 *Reconstruction of 3D fluoroscopic arterial anatomy.*

(A) and (B) Selected angiograms from the primary and secondary projection views; (C) and (D) Reconstructed 3D arterial anatomy.

The reconstructed centerline points and half its corresponding diameters (d) obtained in Section 2.1.2 were used to create a series of circles perpendicular to the centerline along the vascular curve. 40 quadrangles were created between every two adjacent circles to mesh the artery surface, as shown in *Figure 2.11B*. The reconstructed 3D arterial anatomy is shown in *Figure 2.12.*

2.3.3 Development of graphical user interface

A graphical user interface (GUI) for arterial anatomy reconstruction was developed using MATLAB GUI designer. A series of buttons and functions were implemented to enhance the ease-of-use of this artery reconstruction tool, such as “Load LCA/right coronary artery (RCA) image”, “LCA/RCA skeleton”, “LCA/RCA Topology”, “Reconstruct LCA/RCA”, etc. It is a process chain for operators to reconstruct 3D coronary arteries. Appendix A shows a few GUI screenshots of this tool.

2.4 Computer simulation of fluoroscopy angiography for evaluation

Computer Simulation is usually considered effective, flexible, and precise to validate the correctness of new algorithms. In this section, fluoroscopy angiography simulations were designed to evaluate the accuracy of the reconstruction algorithm using a GATE simulator [70] and X-CAT digital phantom [71]. Fluoroscopy angiograms of LCA and RCA from common views were first simulated, and then 3D arterial anatomies were reconstructed using the proposed 3D artery reconstruction approach. The reconstructed arteries were then compared with the X-CAT phantoms (gold standard) to evaluate the accuracy of the reconstruction algorithm.

2.4.1 Generate LCA and RCA digital phantoms using X-CAT

X-CAT is a 4D digital human body phantom developed by Duke University for medical imaging research [71]. It provides sufficient parameters to control and adjust phantom in aspects of physiology effects and anatomy structure. In order to simulate the injection of contrast during angiogram acquisition, coronary arteries should be assigned to a higher attenuation coefficient. However, X-CAT does not provide an interface to adjust the

attenuation coefficient for coronary arteries. Fortunately, it provides an ON/OFF switch to include or exclude the artery in the exported phantom. Based on this mechanism, I obtained the artery phantom with the following steps: (1) generate Phantom 1 with arteries excluded; (2) generate Phantom 2 with arteries included; (3) Subtract Phantom 1 from Phantom 2 to obtain artery indexes in Phantom 2 and then add a coefficient of 0.5 to the voxels with the indexes. Accordingly, a coronary artery phantom including LCA and RCA was obtained as shown in *Figure 2.13A*. The voxel size of the phantom is $0.781 \times 0.781 \times 0.781 mm^3$.

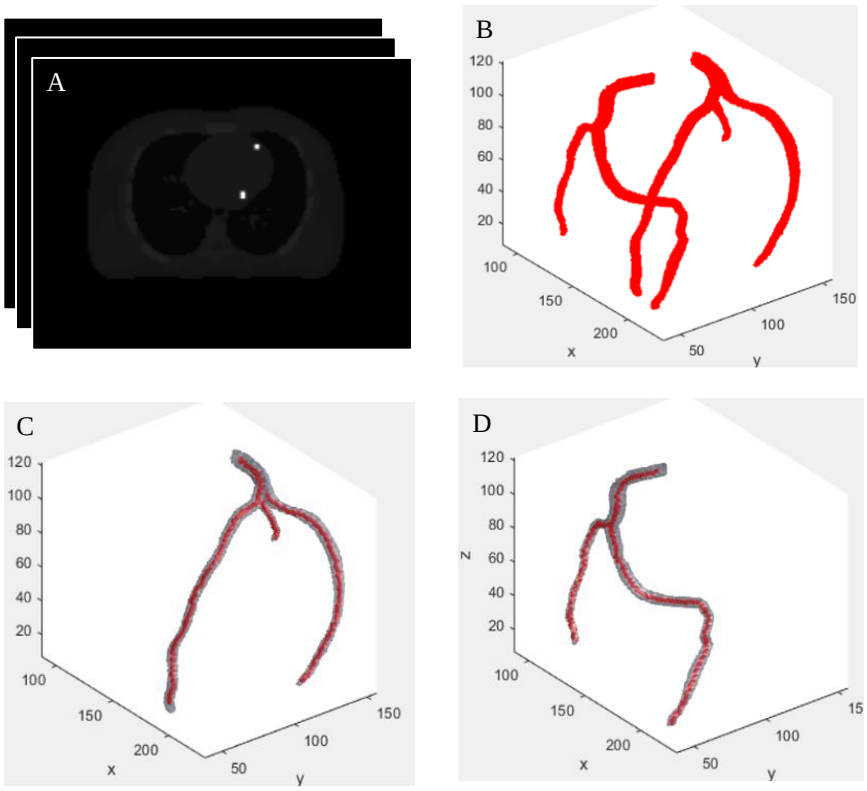

Figure 2.13 *X-CAT phantom and arterial anatomy extraction*

(A) X-CAT phantom slices containing all body organs. The attenuation coefficient of coronary arteries is enhanced. (B) Extracted LCA and RCA phantom. (C) Separated LCA phantom. (D) Separated RCA phantom. LCA = left coronary artery. RCA= right coronary artery.

In the clinical fluoroscopy angiography, LCA and RCA angiograms are acquired separately, which means LCA and RCA in the phantom need to be divided. A connected

component detection algorithm[72]was used to separate LCA and RCA from the phantom so that LCA and RCA phantoms were obtained as shown in *Figures 2.12 B~D.*

2.4.2 Simulate LCA and RCA fluoroscopy angiography using a GATE simulator

GATE is a Monte Carlo simulation platform dedicated to numerical simulations of emission tomography (PET/SPECT), computed tomography (CT), optical imaging, and radiotherapy [73]. It is an essential tool in emission tomography to assist in the design of new medical imaging devices, assess new implementations of image reconstruction algorithms, and optimize scan protocols.

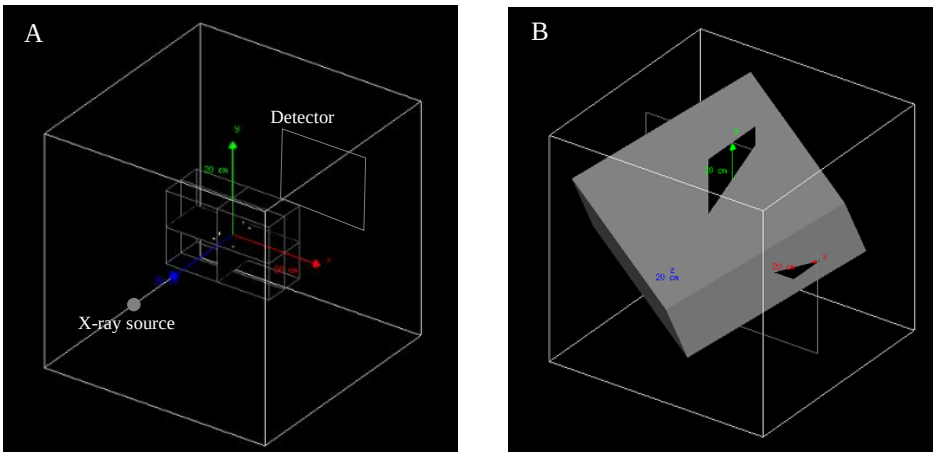

Figure 2.14 *Simulation setup of fluoroscopy system in Gate*

(A) Setup of X-ray source, detector, and X-CAT phantom in Gate environment. (B) Inversely rotated X-CAT phantom for simulations of primary and secondary views.

In the simulation experiment, a fluoroscopy angiography system was created in GATE environment and the X-CAT phantom was placed at the center of the system, as shown in *Figure 2.14A*. The X-ray source position, detector position, SID, and SOD were determined based on conventional fluoroscopy angiography protocol. For LCA, the primary and secondary angles were set as LAO45˚ & CRA30˚ to observe LAD artery and its affiliated

branches, and set as RAO30˚ & CAU35˚ to observe LCX artery and affiliated branches. The simulated fluoroscopy angiograms were shown in *Figures 2.15A and B*. For RCA system, a regular view from LAO1˚ & CRA29˚ for checking distal RCA (posterior descending artery (PDA) and posterolateral branch (PLB)) was simulated, and another view from RAO33˚ & CAU5˚ for observing middle RCA was simulated (*Figure 2.15 C and D*). All the simulated images have a pixel size of 0.34 mm and a resolution of 512×512. It is noted that all the rotations were implemented via rotating phantom to inverse angles, which is easier and more flexible to rotate the phantom rather than the detector and X-ray source.

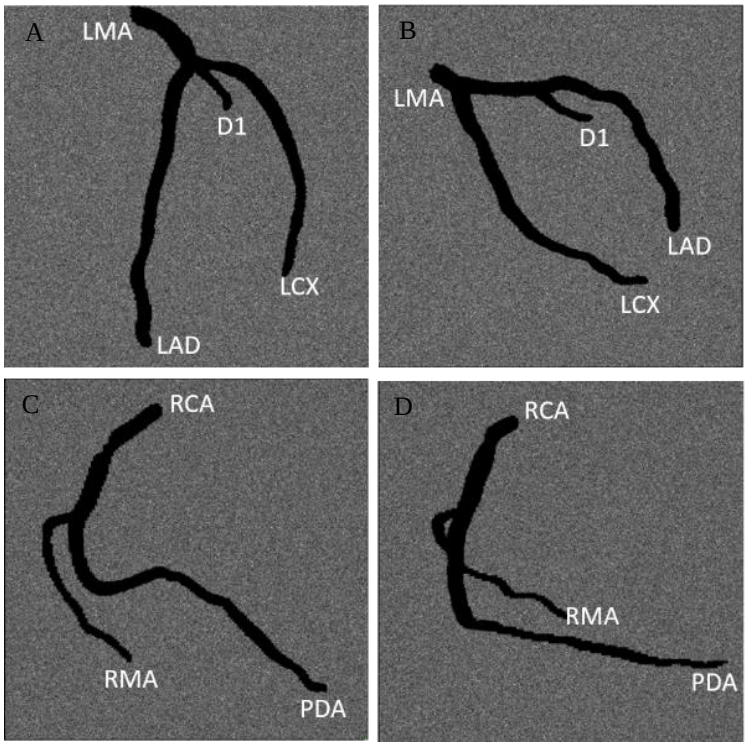

Figure 2.15 *Simulated fluoroscopy angiograms.*

(A) Simulated fluoroscopy angiogram of LCA from LAO 45˚ and CRA 30˚. (B) Simulated fluoroscopy angiogram of RCA from RAO 30˚ and CRU 35˚. (C) Simulated fluoroscopy angiogram of RCA from LAO 1˚ and CRA 29˚. (D) Simulated fluoroscopy angiogram of RCA from RAO 33˚ and CAU 5˚.

2.4.3 Validate the reconstruction algorithm using simulated fluoroscopy angiograms

With the simulated images, LCA and RCA centerlines were reconstructed using my 3D artery reconstruction approach. The 3D LCA and RCA centerlines (*Figure 2.13*) from X-CAT phantoms were extracted using a 3D thinning tool[74]. In order to evaluate the accuracy of the reconstruction algorithm, the mean distance between reconstructed centerlines and the corresponding phantom centerlines (gold standard) was computed as shown in *Figure 2.16*, which was considered as distance-based mismatch error.

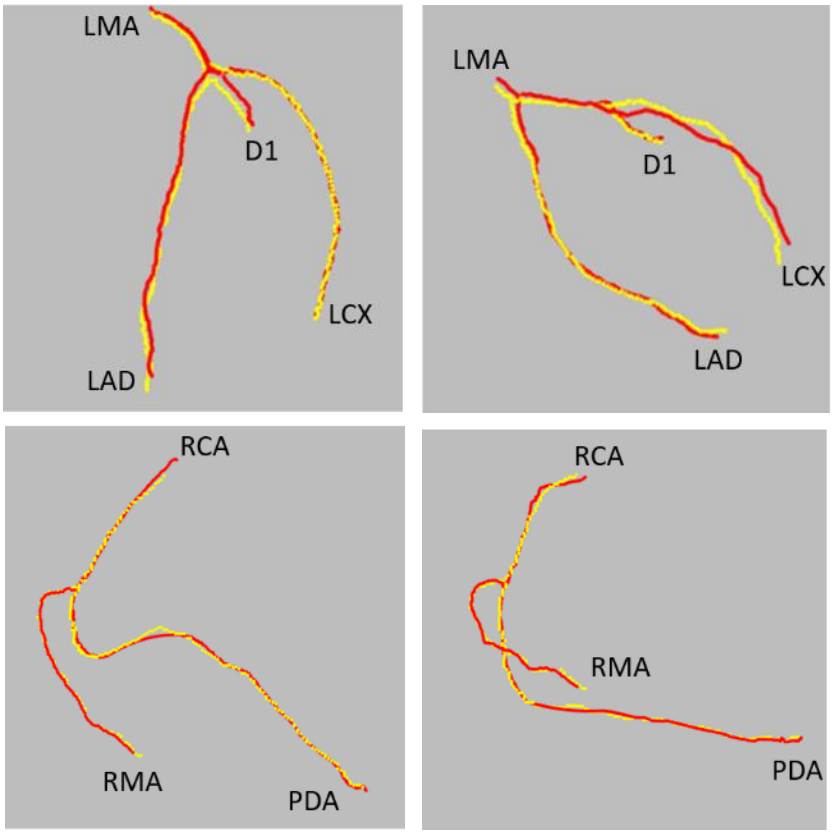

Figure 2.16 *Comparison of reconstructed centerlines and the gold standard in the X-CAT phantom.*

(A) and (B) are the comparisons between reconstructed LCA artery centerlines (red lines) and X-CAT phantom centerlines (yellow lines). (C) and (D) are the comparisons between RCA centerlines (red lines) and X-CAT phantom centerlines (yellow lines).

2.5 Results and Discussions

Table 2.1 lists the distance-based mismatch errors between simulated fluoroscopy and phantom arteries. In LCA system, LMA, LAD, D1, and LCX had mismatch errors of 1.97±0.52, 2.32±1.14, 1.99±0.65, and 0.93±0.43 (unit: mm), respectively. A total of 368 fluoroscopy-phantom artery point pairs were evaluated with an overall mismatch error of 1.67±1.07 mm (min: 0.13, max: 4.85). In RCA system, RCA, right marginal artery (RMA), and PDA had mismatch errors of 1.94±1.68, 0.27±0.40, and 0.27±0.43 (unit: mm), respectively. A total of 392 point pairs were evaluated with an overall mismatch error of 1.22±1.06 mm (min: 0, max: 8.12).

Table 2.1

Distance-based mismatch errors of simulation fluoroscopy-phantom arteries

LCA system	Point pairs	Mean±SD(mm)	Minimum	Maximum
LMA	11	1.97±0.52	0.65	2.50
LAD	163	2.32±1.14	0.22	4.85
D1	34	1.99±0.65	0.32	2.78
LCX	160	0.93±0.43	0.13	2.08
Overall	368	1.67±1.07	0.13	4.85
RCA system	Point pairs	Mean±SD	Minimum	Maximum
RCA	157	1.94±1.68	0.17	8.12
RMA	93	0.27±0.40	0	2.02
PDA	142	0.27±0.43	0	1.99
Overall	392	1.22±1.06	0	8.12

Abbreviation: LMA = left main artery; LAD = left anterior descending; D1 = diagonal branch 1; LCX = left circumflex; RCA = right coronary artery; PDA = posterior descending artery; PLB = posterolateral branch.

In this chapter, I explained the reconstruction and evaluation of the arterial reconstruction algorithm. The improved mathematic model, system calibration, and vessel pairing algorithms ensured a precise reconstruction of 3D arterial anatomy. From the evaluation results, the 3D artery using my reconstruction algorithm showed a small mismatch error compared to the gold standard from the X-CAT phantom. An accurate 3D arterial anatomy is essential for the precise fusion between arterial anatomy and LV surface. Moreover, based on the reconstruction approach, a 3D artery reconstruction tool was developed. It provides a concise and friendly graphical user interface for operators to reconstruct 3D arteries, which enhances the usability and applicability of this tool.

It is noted that several factors may affect the accuracy of 3D artery reconstruction. Fluoroscopy angiography usually acquires a series of frames during cardiac cycles. It is important to select the frames as close as the same time point during the cardiac cycle for accurate 3D artery reconstruction. In this study, we visually selected the frames which approximately corresponded to the end-diastolic time point over the cardiac cycle. Since there were around 10~20 frames acquired in a cardiac cycle, the scale sizes of the angiograms around the end-diastolic time point were close. The reconstruction based on the end-diastolic frames from different views may barely affect the accuracy of the artery reconstruction.

With a dice score of 0.87, our deep learning-based segmentation model using Unet++ framework performed well in most cases. However, the segmentation model may fail when segmenting the vessels within regional blur or low contrast on the angiograms. Once it happened, manually drawing the centerline for correction is needed. Moreover, complicated overlaps may affect the quantification of artery contour diameter. In this

project, the artery contour was obtained through morphology operation-based method. Therefore, the area with complicated overlaps may not accurately represent the arterial contour, which declines the accuracy of artery contour quantification.

Furthermore, the spatial angle gap between the primary and secondary views may also affect the accuracy of 3D arterial anatomy. Since only two views are used to reconstruct a 3D object, the ideal spatial angle gap is orthogonal. Obviously, this is difficult to meet in clinical practice. Based on experience, it is recommended to select the projection views within the angle ranges from 45˚ to 145˚. The closer to orthogonal is, the better reconstruction is. In the clinic, LCA angiography can usually meet this condition from standard views by viewing LAD and LCX arteries. RCA angiography also meets this condition in most cases but is limited to the cases of which the spatial angles are out of the range. Once it happened, one more angiogram in the range is needed for more accurate 3D reconstruction.

CHAPTER III – EXTRACTION OF LV MORCARDIAL SURFACE FROM MYOCARDIAL PERFUSION IMAGES

This chapter explains my method to extract LV epicardial surface from nuclear myocardial perfusion images. Section 3.1 demonstrates a dynamic programming-based method to sample the LV epicardial surface. Section 3.2 presents the approaches to smoothen LV epicardial surface and render myocardial perfusion information on it. Section 3.3 introduces a computer simulation using a GATE simulator and X-CAT phantom to evaluate the accuracy of the LV surface extraction algorithm.

3.1 Extraction of LV epicardial surface on SPECT images

Model-based algorithms are commonly used to sample LV middle, endocardial, and epicardial surfaces from SPECT/PET images[75][76][77]. These algorithms first model the LV as a cylinder and sphere, sample LV mid-surface by searching for the position of myocardium with the maximum counts, and then estimate the endocardial/epicardial surface by using a fixed number of SDs of Gaussian fitting to the myocardial count profile. However, these model-based methods cannot accurately delineate the LV endocardial/epicardial surface. In this section, I used a dynamic programming-based approach to extract LV epicardial surface piloted by mid-myocardial surface.

3.1.1 Transformation from short-axis to long-axis images

Common myocardial SPECT volume after reorientation consists of a series of short-axis images from cardiac apex to base, as shown in *Figure 3.1A*. The sampling of LV myocardial surface is commonly implemented by searching for the sample points on short-axis slice in SPECT volume (*Figure 3.1C*). However, the sampling in LV apex area based

on the sphere model cannot form a closed shape, which is unsuited to the implementation of dynamic programming. Sampling on long-axis slices (*Figure 3.1B*) can ensure a closed ellipsoid to avoid this problem. Therefore, the SPECT volume was transformed from short-axis to long-axis slices by sampling every 9˚ latitudinally, as illustrated in *Figure 3.1D*.

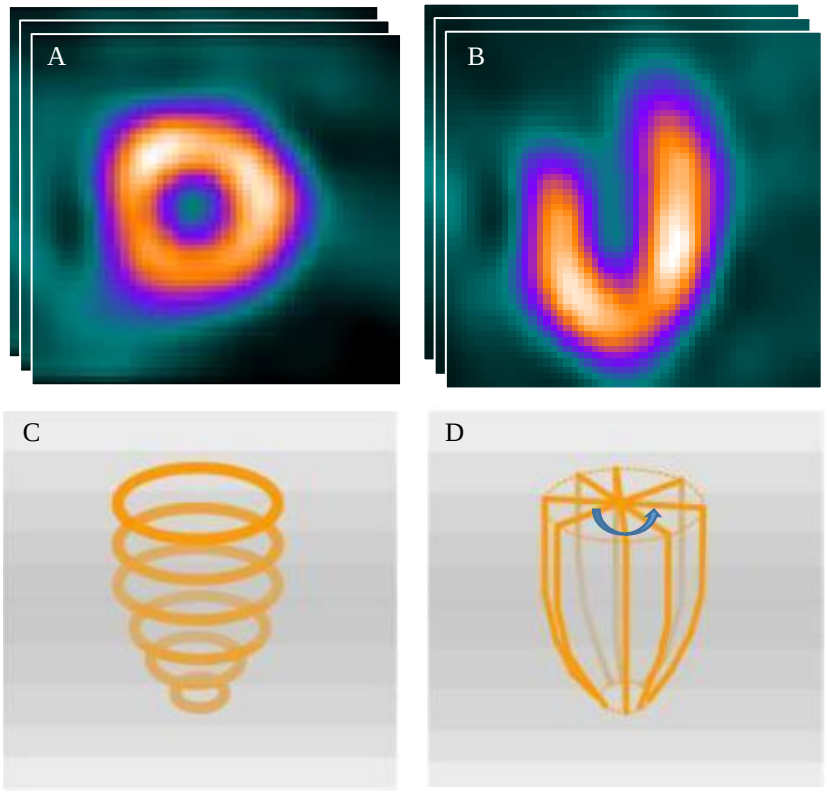

Figure 3.1 *Sampling strategy of left ventricular (LV) myocardial surface.*

(A) Short-axis SPECT image. (B) Long-axis SPECT image. (C) LV sampling on short-axis slices. (D) LV sampling on long axis slices. With permissions, C and D are cited from [78].

3.1.2 Detection of LV myocardial surface using a dynamic programming-based method

The long axis image(*Figure 3.2A*) was transformed from Cartesian to polar coordinates by longitudinally sampling every 2 ˚ with the center of LV volume, where vertical and

horizontal coordinates stand for radius and angles (*Figure 3.2B*). In the polar coordinates, the gradients of image along radial direction and reverse radial direction were computed respectively, as shown in *Figure 3.2C* and *Figure 3.2D.* The maximal differential values in the images can be used to estimate the endocardial and epicardial contours. However, the estimations of both endocardial and epicardial contours were sensitive to the noise surrounding the endocardial and epicardial surfaces. A dynamic programming-based method[78] was improved to address this issue. An initial endocardial surface was first estimated, and then mid-myocardial contour was determined using the dynamic programming-based method piloted by the estimated endocardial contour. Finally, exact endocardial and epicardial contours were detected with the piloting of mid-myocardial contours.

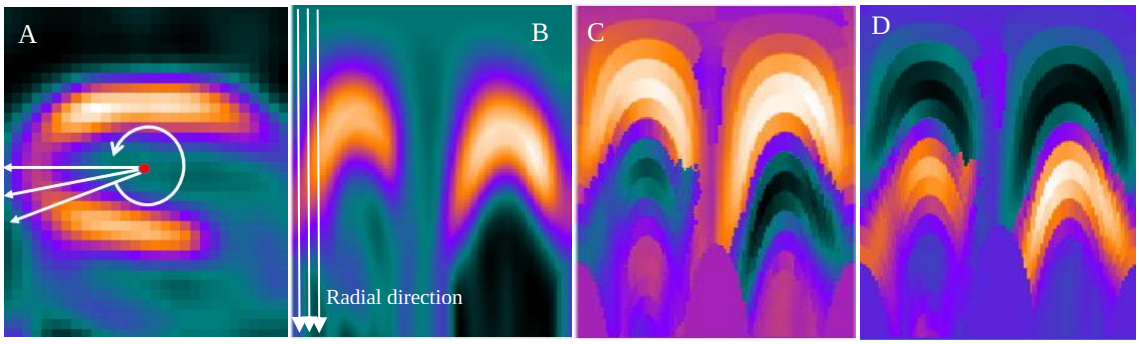

Figure 3.2 *Long axis image transformation from Cartesian to polar coordinates and detection of endocardial surface.*

(A) Transformation from Cartesian to polar coordinates by sampling 2˚ longitudinally. (B) Transformed image in polar coordinates. (C) Gradient map of image B in the radial direction. (D) Gradient map of image B in the reverse radial direction. Brighter area stands for higher gradient.

Figure 3.3D shows the initial endocardial contour which was estimated by searching for the maximum gradient along the radial direction in the polar coordinates. Although this

initial endocardial contour cannot exactly depict the inner cavity of myocardium, it illustrated the basic shape of inner cavity and therefore was used to pilot the mid-myocardium contour via a searching constrain. As shown in *Figure 3.3A*, a sliding window piloted by the initial endocardial contour was used to search for the maximum values in the transformed polar image (*Figure 3.3E*) and then saved the positions of the maximum values to the right adjacent columns in a table (*Figure 3.3B*). This procedure was completed by traversing throughout the whole polar image from top-left to bottom-right corners to generate a position table. Each element in the table saved the position of the maximum value within the sliding window in the left adjacent column. Then, the maximum value of the last column on the polar image was found. Its corresponding position value in the last column of the position table was used to backward search for the previous maximum values from the last column to the second column, as shown in *Figure 3.3C*. Accordingly, the mid-myocardial contour was identified in the polar image (as the black line *in Figure 3.3E*). A transformation from polar to Cartesian coordinates was finally executed to obtain the mid-myocardial contour in Cartesian coordinates *Figure 3.3H*.

Similarly, the dynamic programming-based method was used to identify epicardial contour piloted by mid-myocardial contour. Based on the polar image (*Figure 3.3E*), the inverse gradients between every two adjacent pixels in the radial direction were computed to generate a gradient image, as shown in *Figure 3.3F*. The sliding window searched for the positions of the maximum gradients within the window from the position of mid-myocardial contour to the end of the column on the gradient image. All the positions were saved in the position table of the gradient image. The maximum gradient value of the last column in the position table was used to backward search for the LV epicardial contour in

polar coordinates. The contour was finally transformed back to the Cartesian coordinates, as shown in *Figure 3.3I*.

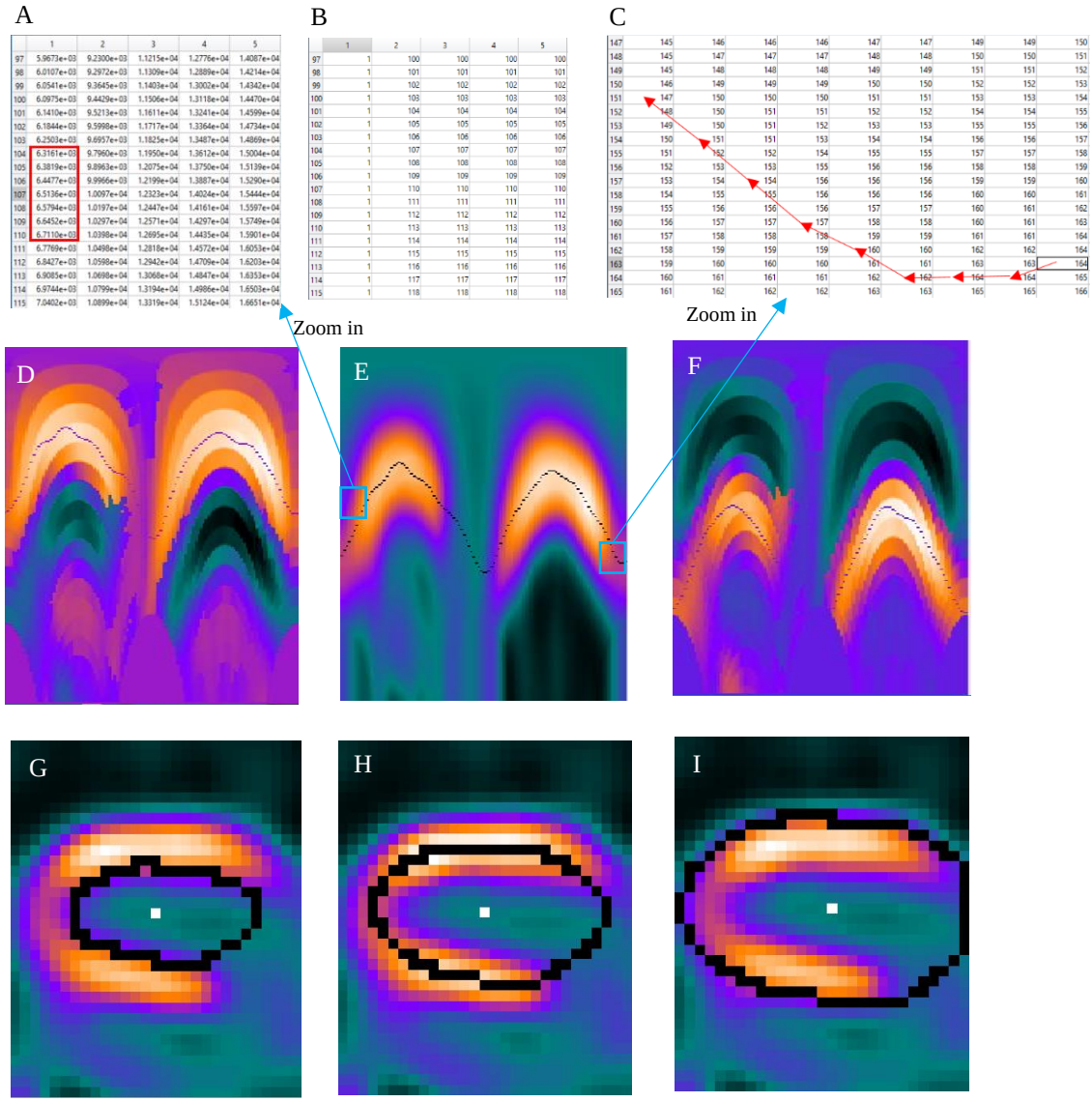

Figure 3.3 *Dynamic programming based algorithm to extract the LV surfaces.*

(A) A glance of long-axis image in polar coordinates. The red box is a sliding window. (B) A glance of the position table. Each value in the image represents the position of maximal gray value or gradient value within the sliding window in the left adjacent column. (C) Backward searching for the positions with maximum value in the polar image. (D) Gradient map of long-axis image in the radial direction. (E) Long-axis image. (F) Gradient map of long-axis image in the reverse radial direction. (G) LV endocardial contour. (H) LV mid-myocardial contour. (I) LV epicardial contour.

3.1.3 Smoothening and rendering of 3D LV epicardial surface

The topology of LV epicardial sampling points was determined by the sampling strategy as mentioned in Section 3.1.1 and Section 3.1.2. The LV epicardial surface was sampled by 20 axisymmetric slices around the central axis, as shown in *Figure 3.4A*. For each slice, LV epicardial surface was sampled starting from apex, bypassing the base, and ending back to apex. The triangles between every adjacent two longitudinal slice points were drawn, as shown in *Figure 3.4B*.

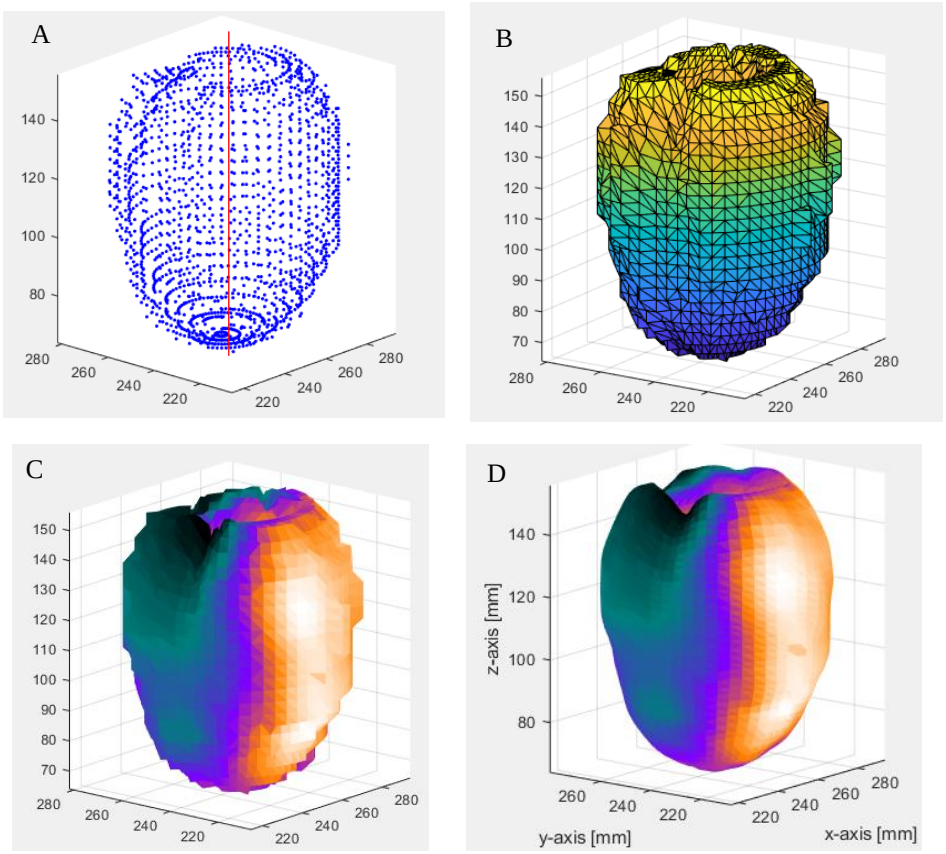

Figure 3.4 *Smoothing of LV epicardial surface*

(A) Sampling points of LV epicardial surface. (B) Triangulation of the sampling points. (C) Rendering myocardial perfusion data on the LV surface. (D) Smoothening of the LV surface.

Myocardial perfusion values were mapped on the corresponding epicardial sampling points. Therefore, the perfusion value of each triangle face was determined by the average perfusion values of the three vertices on each triangle. A colormap was used to render the color of the LV surface, as shown in *Figure 3.4C.*

A triangulated mesh smoothing algorithm was used to smoothen the epicardial surface [79]. This approach smoothens a triangulated mesh via accurate curvature flow smoothing or Laplacian smoothing with inverse vertices distance-based umbrella weights. In order to keep the shape and curvature of the epicardial surface, I set the iteration 10 and lambda 0.3. The smoothening result is shown in *Figure 3.4D.*

3.1.4 Development of graphical user interface

A graphical user interface for LV surface extraction was developed using MATLAB GUI designer. This interface includes a series of buttons and functions: “Load ungated data”, “View slices”, “Set apex & base”, “Reconstruct surface”, etc. Appendix B illustrates several screenshots of this tool. It can load ungated SPECT/PET DICOM data and show short axis (SA) images, horizontal long axis (HLA) images, and VLA (vertical long axis) images, respectively. After determining the apex and base slices, the LV epicardial surface is extracted, shown, and saved via the interface.

3.2 Computer simulation to evaluate the accuracy of LV surface extraction algorithm

This section introduces the validation of the proposed LV surface extraction algorithm via computer simulation. Similar to SPECT, positron emission tomography (PET) is another commonly used nuclear imaging technique. It also uses radiopharmaceuticals to

create three-dimensional images using similar physical principles. The main difference between SPECT and PET images is the spatial resolution of the image. PET has a higher resolution than SPECT. For more precise evaluation, in this study, I simulated PET images to validate the proposed LV surface extraction algorithm. In the simulation experiment, X-CAT was used to generate a heart phantom and GATE simulator was applied for the simulation of PET imaging. Based on acquired true coincidences, the PET images were reconstructed using ordered subset expectation maximization (OSEM) algorithm. The PET images were then processed using the proposed algorithm to extract the epicardial surface. Meanwhile, the epicardial surface from the PET images was manually drawn, which was considered as the gold standard for the comparison to the extracted epicardial surface.

3.2.1 Generating heart phantom using X-CAT

X-CAT provides many options to simulate realistic body or organ phantoms. I first generated a whole-body phantom and cut off the slices above the shoulder and the slices below the waist. In order to acquire a realistic phantom, I enabled the heart beating effect and assign all organs to reasonable activity values based on their uptakes during imaging. Besides, I set activity values of 75 for myocardium including LV, right ventricle (RV), left atrium (LA), and right atrium (RA), 75 for kidney and spleen, 6 for the spine and cortical bone, and 2 for body and other organs. The final phantom volume consists of 128×128×100 with a voxel size of 3.1mm. *Figure 3.5* shows the SA, HLA, VLA slices of the heart phantom. Besides, in order to acquire SA images, the phantom is rotated -63 in the direction of y axis and -45 in the direction of z axis.

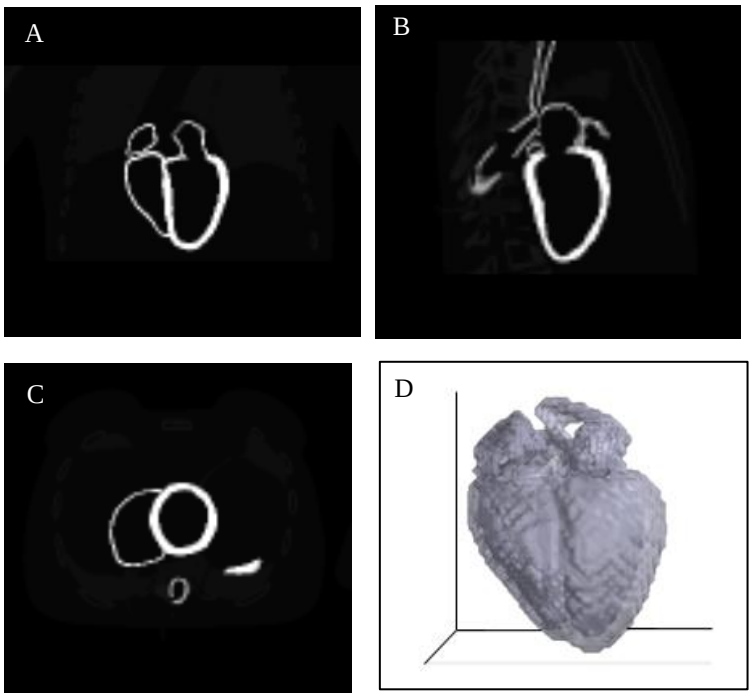

Figure 3.5 *Heart phantom generated by X-CAT*

(A) Horizontal axis image of heart phantom. (B) Long axis image of heart phantom. (C) Short axis image of heart phantom. (D) Visualization of heart phantom.

3.3.2 Simulation of PET images using GATE simulator

In GATE, I created the following architecture for PET simulation: (1) defining a scanner geometry, (2) loading X-CAT phantom geometry, (3) setting-up physics processes, (4) initialization, (5) setting-up the digitizer and coincidence sorter, (6) setting-up source, (7) defining the format of output data, (8) starting acquisition.

A Siemens ECAT system for human body was built according to the GATE mechanism that all volumes were linked together following the tree structure. In the world volume, the base of the tree, I first created a cylinder holder volume with a height of 250mm, an inner radius of 430mm, and an outer radius of 50 mm. A total of 46 box rsector volumes holding

modules and crystals were inserted into the cylinder volume, where each rsector consists of 4 modules and each module consists of 144 LSO crystals, as shown in *Figure 3.6*. After creating the scanner system, the generated X-CAT phantom was placed in the center of the world volume.

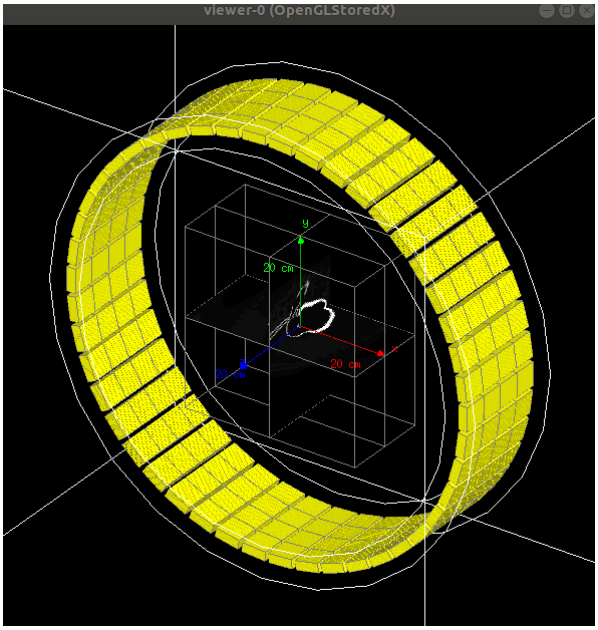

Figure 3.6 *PET system created in GATE environment*

Physical interaction processes in PET imaging were then specified in the simulation. Standard physics processes were included, such as radioactive decay, positron annihilation, electron annihilation, electron ionization, bremsstrahlung, etc. Besides, multiple scattering effects were also enabled including Compton scattering, Rayleigh scatting, photoelectric absorption.

After specifying the physics processes, a digitizer was set up to transform hits to singles with specific readout schemes and trigger logics. The digitizer contained a chain of signal processing modules including Adder, Readout, Energy Blurring, and Thresholder &

Upholder. An Adder module was first inserted into the digitizer to sum all the hits occurring within the same crystal and regroup them into a pulse with setDepth 1. The Readout module was then inserted to regroup the pulses per block with the strategy “winner-takes-all”. For the energy blurring module, energy resolution was set to 0.26 at 511 keV with Gaussian blurring of the energy spectrum of a pulse after the Readout module. A Thresholder & Upholder was finally inserted to apply an energy window to save the photons within the threshold from 350 keV to 650 keV. Accordingly, with this processing chain, hits information including energy, position, and time of detection for each particle, were processed and transformed into the singles.

From the singles list generated by Digitizer, a Coincidence Sorter was set up to search for the pairs of coincident singles (true coincidence) within a 10 ns coincidence window using the “takeWinnerOfGoods” policy. Besides, a 10 ns delay window from 500 ns offset was created to estimate the random coincidences.

The source of this simulation system was specified by the preset activity values of the organs in X-CAT phantom, as mentioned in Section 3.3.1. Energy type was set as Mono and half-life is 6586.2 s. It generated pairs of 511 keV gamma particles emitted ‘back-to-back’. After setting up the source, the output type of coincidence data was specified as ASCII and root which were used to reconstruct PET images. After setting up the simulation architecture, the simulation started to acquire PET data.

3.2.2 Reconstruction of PET images using Omega approach

Omega is an open-source software[80] to reconstruct image obtained with positron emission tomography device or simulation data. Based on the PET system created in GATE, the machine properties were specified in Omega as following: block_per_ring =

46, linear_multip = 4, crystal_per_block = 12, crystal_pitch = 4.2, crystal_pitch_z-direction = 4.2, diameter of ring = 430×2, FOV_x = 400, FOV_y = 400, FOV_axial = 199. Besides the simulated machine properties, the sinogram and image properties were then specified. Sonogram_span determines the axial compression, indicating how many sonograms are combined in the axial direction. In order to obtain high image quality, I set 3 for the span factor, which is the smallest span supported by Omega. Ring difference is related to the span value and is set to 47 (number of crystal rings - 1). Depending on the modeling of the stimulation device, the number of angular positions was set to 500 and the number of angles was set to 276. The resolution of reconstructed image was set as resolution_X=128, resolution_Y=128, resolution_Z=95. Moreover, several GATE specific settings were determined, including obtain_true_coincidence, store_scatter, reconstructe_trues, scatter_components, reconstruct_scatter, store_randoms, source, etc.

With the PET coincidence data acquired from GATE simulator, the OSEM algorithm was used to reconstruct PET images using 8 subsets and 3 iterations. The reconstructed PET images have a voxel size of 3.2 mm^3. Butterworth filter[81] was used to post-process the reconstructed images using a lowpass of 5, a highpass of 50, and an order of 5. The reconstructed PET images are shown in *Figure 3.7*.

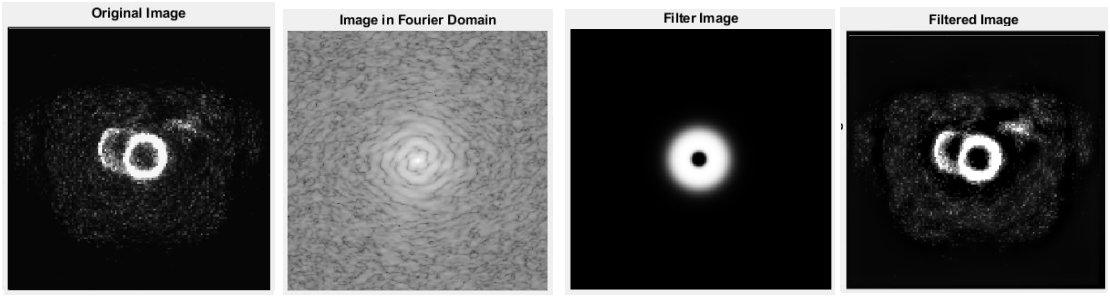

Figure 3.7 *Reconstructed PET images after processing with Butterworth filter.*

3.2.3 Accuracy validation of LV surface extraction algorithm.

Based on the reconstructed short-axis images, a MATLAB Image Segmentation tool[82] was used to manually draw the LV myocardium from the reconstructed PET images (*Figure 3.8A*). The manually LV surface points were then multiplied by voxel size of PET image and plotted as *Figure 3.8B*, which was considered as the gold standard for evaluation.

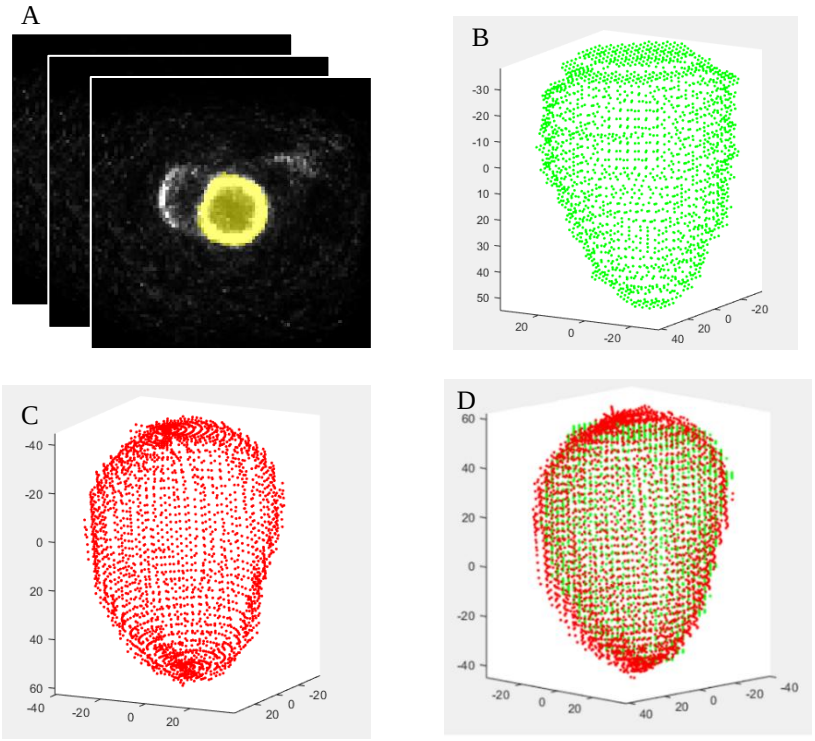

Figure 3.8 *Simulated PET images and comparison of LV epicardial surfaces*

(A) Reconstructed PET images using simulated data. (B) Manually drawn sampling points of LV epicardial surface. (C) Sampling points of LV epicardial surface extracted

On the other hand, the reconstructed PET images were processed using my LV surface extraction method to obtain the LV epicardial surface as shown in *Figure 3.8C*. The extracted LV epicardial surface was sampled with 4200 points and moved to the origin of the coordinates. Meanwhile, the manually drawn LV epicardial surface points (gold

standard) were also moved to the origin of coordinates for comparison. A rigid ICP algorithm was used to register these two LV surface point clouds. 4200 LV sampling points were paired with the gold standard LV points. The mean distance between them was computed to evaluate the accuracy of LV extraction algorithm.

3.3 Results and Discussions

In this chapter, I demonstrated the extraction of LV epicardial surface from SPECT images using the dynamic programming-based method, the simulation of PET images using GATE simulator with X-CAT phantom, and the evaluation of the LV extraction algorithm. A total of 4200 sampling point pairs were evaluated. The result shows an average mismatch error of 2.82±1.53 mm (min: 0.02, max: 14.5), which is approximately equal to the voxel size (3.2 mm^3) of the simulated PET image.

Compared to the model-based algorithm[75][76][77], LV epicardial surface extracted by the proposed extraction algorithm showed more accurate morphological features of LV. It is essential for the fusion of arterial anatomy and LV surface. S-ICP/ICP algorithm completes registration based on the morphological features of two objects. Accurate LV surface has better morphological features and fewer noises, which usually ensures a successful registration. In contrast, defective features and redundant noises may trap the registration into a local minimum, resulting in a failed registration. Moreover, accurate LV contour is helpful to not merely the fusion, but also the assessment of heart functions in the future application. Several heart shape indexes, such as systolic/diastolic shape index and eccentricity, can be precisely assessed. The more accurately assessed heart shape indexes

together with the anatomical and physiological information provide more valuable information for the diagnose of heart disease in clinical practice.

It is noted that the extraction algorithm is sensitive to noises and abnormal organ defects. If the image quality is low, such as PET images with Rubidium 82 tracer, the algorithm may fail in extracting LV epicardial surface. The messy noise or abnormal organ defects on Ru^{82} PET images may deteriorate the search trajectory of LV surface even though the search is piloted by mid-myocardial surface.

The evaluation result shows an average mismatch error of 2.82±1.53 mm between extracted LV surface and gold standard LV surface. Two factors may negatively impact the result. First, manually drawing the epicardial contour brought many uncertainties when the boundary of LV contour was blurry and in an irregular shape. It was not easy to identify the boundary and draw a smooth curve using a mouse. In other words, the gold standard LV surface may not able to precisely represent the LV epicardial surface in the PET volume, which may deteriorate the evaluation result. Second, although the scatter and random corrections were applied, reconstructed PET images may still contain much unpredictable noise, which may negatively affect the extraction of LV epicardial surface, as mentioned above, this extraction algorithm is sensitive to noise.

CHAPTER IV – IMAGE FUSION BETWEEN 3D ARTERIAL ANATOMY AND LV EPICARDIAL SURFACE

This chapter presents a non-rigid image fusion approach that integrates the 3D arterial anatomy from fluoroscopy angiograms with the LV epicardial surface from SPECT images. A landmark-based registration method was used to complete a rough alignment (Section 4.1) and then S-ICP, a non-rigid registration algorithm, was used to refine the registration (Section 4.2). A vessel-surface overlay algorithm was finally used to overlay all the arteries onto the LV epicardial surface.

In order to verify the fusion approach, technical (Section 4.3) and clinical validations (Section 4.4) were executed. In the technical validation, simulated fluoroscopy angiograms were reconstructed into 3D arterial anatomy and then fused with the LV surface from the simulated nuclear images. The artery-surface fusion was compared to the gold standard from the X-CAT phantom using my deformable fusion approach. In the clinical validation, 30 patients who underwent fluoroscopy angiography, SPECT-MPI, and CT angiography were enrolled. The SPECT-MPI and fluoroscopy angiography data were integrated using my reconstruction and fusion algorithms. 3D arterial anatomy and LV epicardial surface from the CT angiography were extracted and used as the gold standard to evaluate the accuracy of artery-surface fusion.

4.1 Initial rough registration based on landmarks

4.1.1 Landmark identification and extraction

According to the characteristics of coronary anatomy[34], LAD travels in the anterior interventricular groove, proximal LCX travels in the left atrioventricular groove, and PDA

travels in the inferior interventricular groove. These grooves are spontaneous landmarks and used to roughly register the arterial anatomy with LV surface.

A graphical user interface was developed to identify these landmark points on SPECT short-axis images as shown in *Figure 4.1*. RV anterior groove starting and end points were first identified. A linear 3D interpolation algorithm was used to interpolate groove points on each short-axis slice between the starting and end points. So a partial groove line was formed. Since the groove anatomically starts from base and ends to apex, the partial groove line was extended up to base and down to apex slices along with its back-to-back directions. Then the extended groove line between apex and base slices was overlaid onto the LV surface using a vessel-surface overlay algorithm[83], as shown in *Figure 4.1B*. Similarly, the inferior groove line determined by inferior groove starting and end points was obtained and overlaid onto the LV surface, as shown in *Figure 4.1C*. These anterior and inferior grooves on LV surface were used as landmarks for the landmark-based registration.

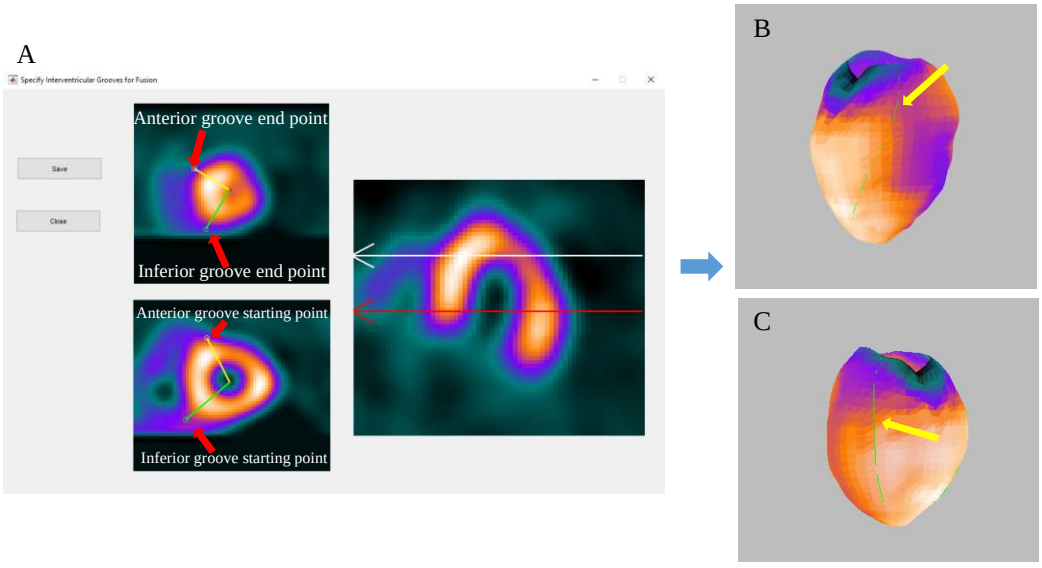

Figure 4.1 *Identification of landmarks with graphical user interface*

(A) User interface to identify groove starting and end points. (B) Anterior groove. (C) Inferior groove.

4.1.2 Objective function of landmark-based registration

The artery anatomy and LV surface were first moved to the center of the coordinates, as shown in *Figure 4.3A*. The landmark-based registration was then used to complete the initial registration. It aims to minimize an objective function defined as the sum of squared distance between the following three curve pairs: a) between LAD and anterior interventricular groove, b) between LCX and LV base, c) between PDA and inferior interventricular groove. The registration result is shown in *Figure 4.3B.*

The landmark-based registration can only align the major vessels, such as LAD, LCX, and PDA. However, the branches and extensions of the major vessels may not be accurately aligned, which affects the accuracy of the artery-surface fusion. In addition, this rigid registration requires a pair of scale-matched arterial anatomy and LV epicardial surface objects, which is difficult to obtain due to the separate image acquisitions at different cardiac frames.

4.2 S-ICP based fine registration and vessel surface overlay

The following proposed S-ICP is a non-rigid registration algorithm for two point-cloud objects. It adjusts the scale of one object up to or down to the optimal scale and then registers the object with the other object by minimizing the squared distance between them.

According to the Theorem1 [84], like the standard ICP algorithm[37], S-ICP also monotonically converges to a local minimum. To achieve a global accurate minimum, it is necessary to perform an initial registration with reasonable rotation R, scale S, and translation t. The landmark-based registration (Section 4.1) aligned the major vessels to the

corresponding interventricular grooves, which can appropriately serve as an initial registration of S-ICP.

4.2.1 Problem formulation of S-ICP algorithm

Compared to standard ICP algorithms[37], S-ICP introduces a scale factor and merges this factor into the standard ICP. A constraint optimization problem was formed with respect to rotation R, scale S, and translation t, as shown in Eq. 12, where *p* is the 3D arterial anatomy, *m* is the LV epicardial surface(*Figure 4.3B*), *k* is the *kth* iteration, and *Np* is the number of points of the 3D arterial anatomy. With the initial transformation parameters generated by landmark-based registration, the objective function $F^k(R, S, t)$ was iteratively optimized with the following two steps[84][85]. (a) The first step was to create the correspondence between *m* and *p*, based on current parameters (R^k, S^k, t^k). A Delaunay triangulation based algorithm[86] was used to solve this problem, which finds the corresponding points in *m* which are closet to *p*. (b) Based on current correspondences, the second step was to compute new transformation parameters (R^{k+1}, S^{k+1}, t^{k+1}) until a preset threshold. Section 4.2.2 explains details the iteration process.

$$(R^{k+1}, S^{k+1}, t^{k+1}) = arg\ min_{R\in SO(3), S\in I}\left[\ F^k(R,S,t) = \sum_{i=1}^{Np} || \ (S \bullet Rp_i + t) - m_i \ ||^2\ \right]$$

Eq. 12

$$(R^{k+1}, S^{k+1}) = arg\ min_{R\in SO(3), S\in I}\Big(F^k(R,S) = \ \sum_{i=1}^{Np} S^2\, \tilde{p}_i^{(T)}\tilde{p}_i - 2\sum_{i=1}^{Np} S \cdot$$

$$(R\tilde{p}_i)^{(T)}\tilde{m}_i^k + \sum_{i=1}^{Np} \tilde{m}_i^{k(T)}\tilde{m}_i^k\ \Big),$$

(where $\tilde{p}_i = p_i - p_c$, $\tilde{m}_i^k = m_i^k - m_c^k$, $p_c = \frac{1}{N_p}\sum_{i=1}^{N_p} p_i$, $m_c = \frac{1}{N_p}\sum_{i=1}^{N_p} m_i$, *T* means transpose) *Eq. 13*

4.2.2 Computation of rotation R^{k+1}, scale S^{k+1}, and translation t^{k+1}.

In order to compute (R^{k+1}, S^{k+1}, t^{k+1}), I first simplified the objective function by eliminating the translation parameter. According to Lemma 1[87], the translation transformation could be eliminated via moving the center (m_c) of point cloud *m* to the center(p_c) of point cloud *p*. So the problem *Eq. 12* was transformed into the quadric optimization problem described in *Eq. 13* concerning the computation of R^{k+1} and S^{k+1}. To minimize $F^k(R, S)$, the partial differential equation of F^k needs to satisfy $\frac{\partial F^k(R,S)}{\partial S} = 0$ and $\frac{\partial F^k(R,S)}{\partial R} = 0$. Given an S^k by the previous iteration, the necessary condition of minimizing $F^k(R, S)$ becomes $\frac{\partial F^k(R,S)}{\partial R} = 0$ which is difficult to compute. However, in the *Eq. 13*, S^k, $\tilde{p}_i^{(T)}\tilde{p}_i$, and $\tilde{m}_i^{k(T)}\tilde{m}_i^k$ are positive terms, minimizing $F^k(R, S)$ is equivalent to maximizing the term $\sum_{i=1}^{Np}(R\tilde{p}_i)^{(T)}\tilde{m}_i^k$. This problem is similar to the computation of R and t using singular value decomposition (SVD) [88] in standard ICP. Therefore, the maximization of the one-variable function $F^k(R) = \sum_{i=1}^{Np}(R\tilde{p}_i)^{(T)}\tilde{m}_i^k$ can be expressed as following:

(i). Calculate the matrix and its SVD.

$H = \frac{1}{N_p}\sum_{i=1}^{Np}(\tilde{p}_i)^{(T)}\tilde{m}_i^k$

$H = U\Lambda V$

(ii). Calculate the rotation matrix *R*

(a) if $\det(VU^T) = 1$, VU^T is a rotation: $R = VU^T$

(b) if det(VU^T) = -1, VUT is a reflection: $R = V\begin{pmatrix}1 & 0 & 0\\ 0 & 1 & 0\\ 0 & 0 & -1\end{pmatrix}U^T$

The combination of (i) and (ii) was shown in *Eq. 14*, accordingly, R^{k+1} was computed. Based on the partial differential equation $\frac{\partial F^k(R,S)}{\partial S} = 0$, S^{k+1} was computed with $\frac{\sum_{i=1}^{Np}(R^{k+1}\tilde{p}_i)^{(T)}\tilde{m}_i^k}{\sum_{i=1}^{Np}\tilde{p}_i^{(T)}\tilde{p}_i}$. Since this algorithm has a local convergence, a scale range was set to avoid failed registration. According to the parabola principle, set $a = s, if\ s \le a;\ b = s, if\ b \le a$, shown in *Eq. 15*. Finally, based on the S^{k+1} and R^{k+1}, t^{k+1} was computed through moving the centers of *m* and *p*, as shown in *Eq. 16*.

$$R^{k+1} = \begin{cases} VU^T, & \det(VU^T) = 1 \\ V\begin{pmatrix}1 & 0 & 0\\ 0 & 1 & 0\\ 0 & 0 & -1\end{pmatrix}U^T. & \det(VU^T) = -1 \end{cases} \qquad \textit{Eq.14}$$

$$S^{k+1} = \begin{cases} a, & s \le a \\ b, & s \ge b \\ \frac{\sum_{i=1}^{Np}(R^{k+1}\tilde{p}_i)^{(T)}\tilde{m}_i^k}{\sum_{i=1}^{Np}\tilde{p}_i^{(T)}\tilde{p}_i}. & a < s < b \end{cases} \qquad \textit{Eq.15}$$

$$t^{k+1} = m_c^k - S^{k+1} \cdot R^{k+1} p_c$$

$$\text{(where } m_c = \frac{1}{N_p}\sum_{i=1}^{N_p} m_i\ ,\quad p_c = \frac{1}{N_p}\sum_{i=1}^{N_p} p_i) \qquad \textit{Eq. 16}$$

$$E^{k+1} = \sum_{i=1}^{Np} \| (S^k \bullet R^k p_i + t^k) - m_i \|^2 \qquad \textit{Eq. 17}$$

After computing R^{k+1}, S^{k+1}, and t^{k+1}, the sum distance-based error E^{k+1} is computed with *Eq.17*. With a preset ε and maximum iteration number *I*, the computation of (R^{k+1}, S^{k+1}, t^{k+1}) were iterated until ε or *I*.

In order to accelerate the convergence of S-ICP, I introduced a dynamic iteration factor h to the iteration process. In each iteration, the change (Δq^{k+1}) of transformation matrix between next and current iterations was computed. If the difference of errors was smaller than ε, the artery points p was transformed h times using the Δq^{k+1}. It is noted that the range of iteration factor h is sensitive to the convergence. A high upper bound of h may lead to an oscillatory convergence curve of the iteration. Through an experiment, h was set as the range from 1 and 3, which showed two times faster convergence velocity and a stable convergence curve. *Figure 4.2* shows the pseudocode of the accelerated S-ICP algorithm.

Input: p is venous anatomy model, m is epicardial surface model.
Initialization: ε, I, R^0, t^0 by landmark-based method and preset $S^0 \epsilon [a, b]$; computed E^0; dynamic iteration factor h=0;
Find the points in m closest to p
Compute R^1 by Eq. 3
Compute S^1 by Eq. 4
Compute t^1 by Eq. 5
Compute E^1 by Eq. 6
Iteration:
while $| E^k - E^{k+1} | > \varepsilon \,||\, k \in [0, I]$
    Find the points in m closest to p
    Compute R^{k+1} by Eq. 3
    Compute S^{k+1} by Eq. 4
    Compute t^{k+1} by Eq. 5
    Compute E^{k+1} by Eq. 6
    Calculate $\Delta q^{k+1} = [R^{k+1} | t^{k+1}] - [R^k | t^k]$
    if $E^k - E^{k+1} > \varepsilon$
        $h=h+1 \quad h \in [1,3]$
        h *times:* $p = \Delta q^{k+1} * p$
    else
        $h=0$
end
Output: R^{k+1}, S^{k+1}, t^{k+1}

Figure 4.2 *Pseudocode of the accelerated S-ICP algorithm*

With the *S-ICP* algorithm, the computed R^{k+1}, S^{k+1}, and t^{k+1} were used to complete the non-rigid registration of LV surface with artery centerlines, as illustrated in *Figure 4.3C*.

4.2.3 Vessel surface overlay

After the registration by S-ICP, all the artery centerlines with contour diameter (d) were overlaid onto the SPECT LV epicardial surface using a vessel-surface overlay algorithm[83], as shown in *Figure 4.3D*.

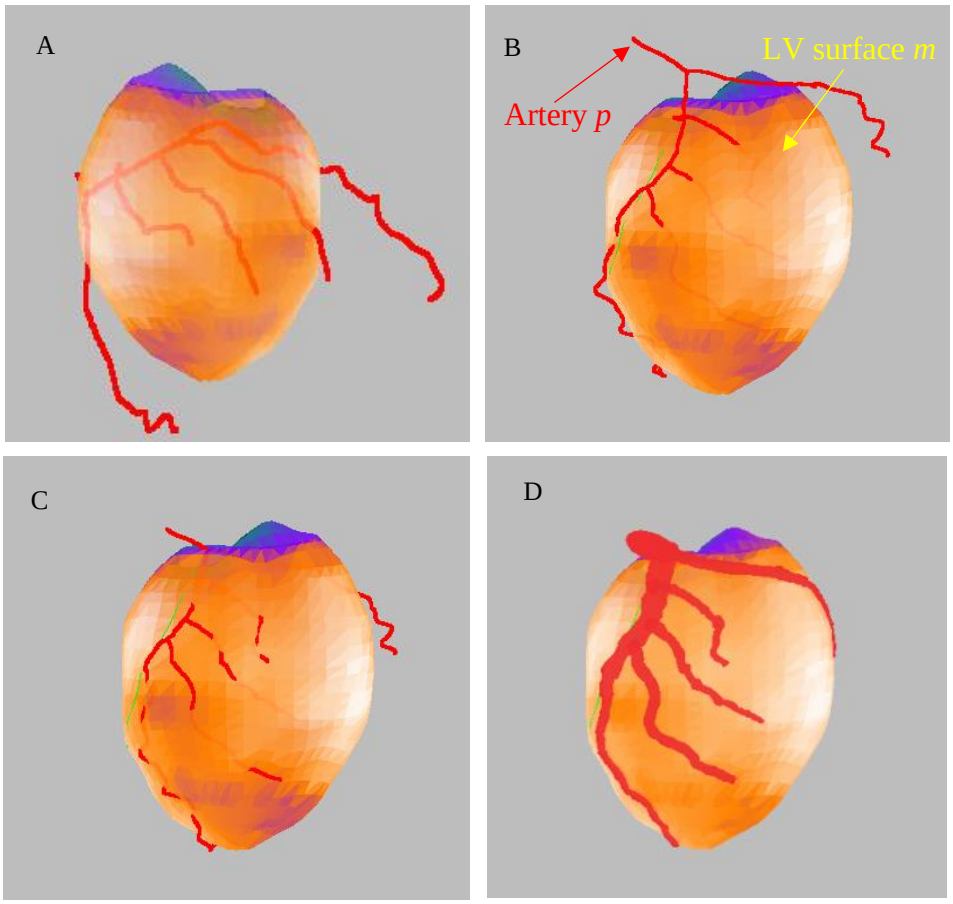

Figure 4.3 *Fusion of 3D artery anatomy and LV epicardial surface.*

(A) SPECT LV epicardial surface and reconstructed artery centerlines before registration. (B) Initial registration using landmark-based method. (C) Fine registration using non-rigid S-ICP registration. (D) Artery overlay and vessel contour rendering.

4.2.4 Development of graphical user interface for artery-surface fusion

A graphical user interface was developed for artery-surface fusion. This interface tool first loads the 3D arterial anatomy obtained from the reconstruction tool (Section 2.3.3) and LV epicardial surface obtained from the extraction tool (Section 3.1.4). Then operators need to identify the inferior and anterior groove points using the interface (Section 4.1.1). The "view fusion result" button shows the artery-surface fusion in a pop-out window. Appendix C shows several screenshots of this fusion tool.

The artery reconstruction, LV surface extraction, and image fusion tools together establish the image-guided system.

4.3 Validation of artery-surface fusion using computer simulations

In order to technically evaluate the accuracy of the artery-surface fusion, computer simulations were implemented. The simulated angiograms (Section 2.4) were reconstructed into 3D arterial anatomy (simu-arteries) using my artery reconstruction tool. The simulated nuclear images (Section 3.2) were processed using my extraction tool to extract the LV epicardial surface (simu-surface). The simu-arteries and simu-surface were loaded into my 3D fusion tool. The anterior and inferior groove points were identified and then the artery-surface fusion was completed, as shown in *Figure 4.4*.

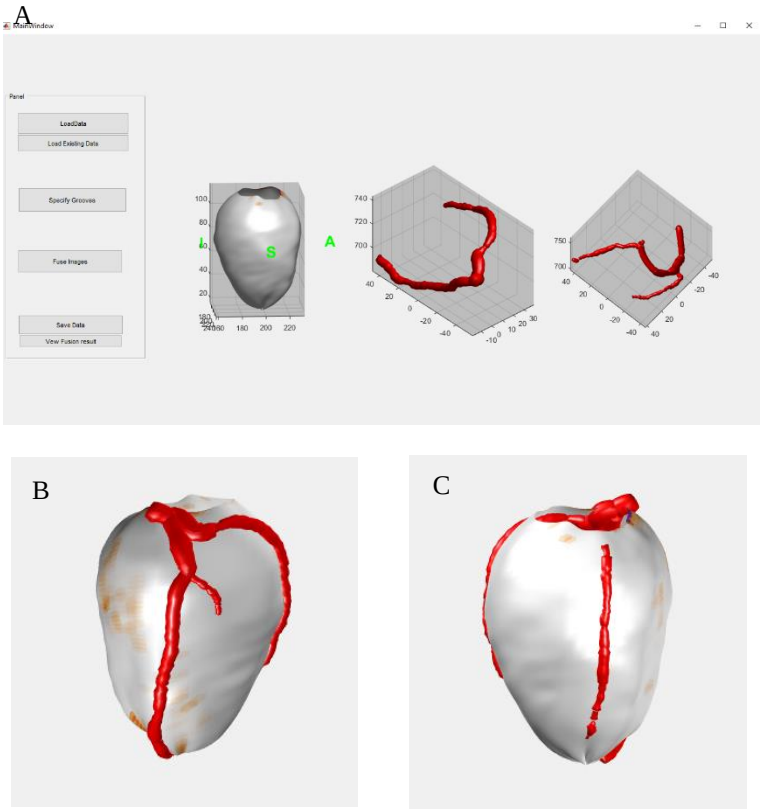

Figure 4.4 *The fusion between LV surface from simulated nuclear images (simu-surface) and arteries from simulated angiograms (simu-arteries) using the 3D fusion tool*

(A) User interface of the fusion tool. (B) Fusion of simu-surface and simu-arteries from anterior view. (C) Fusion of simu-surface and simu-arteries from inferior view.

Myocardial surface (Section 3.2.1) and arterial anatomy (Section 2.4.1) extracted from X-CAT phantom were used as the gold standard for the validation of artery-surface fusion, as shown in *Figure 4.5 A&B*. The gold standard LV surface was manually registered with the simu-surface through aligning anterior, inferior, and base curves on each of the LV surfaces. The transformation was also applied to the gold standard arterial anatomy (GS arteries). Then, the GS arteries were overlaid onto the simu-surface, as shown in *Figure 4.5 C&D*. This procedure was completed using open-source software, Paraview[89][90]. It is noted that only PDA was overlaid on the simu-LV surface in RCA system. Because

only PDA exists in the artery phantom among the arteries which travel on the LV surface. After the alignment, the distances of simu-arteries (red lines in *Figure 4.5 C&D*) from GS-arteries (yellow lines in *Figure 4.5 C&D*) were computed to technically evaluate the accuracy of the artery-surface fusion.

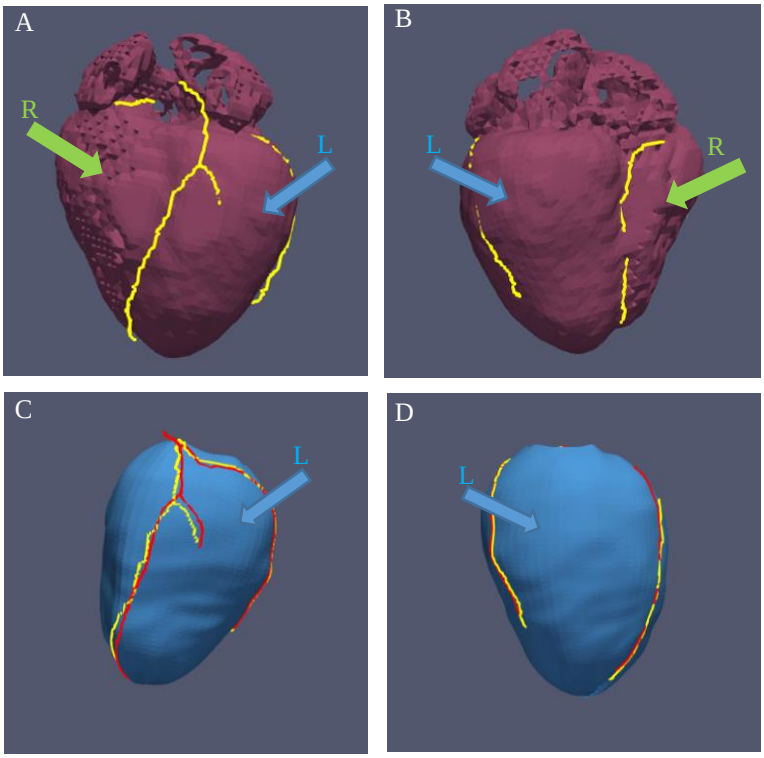

Figure 4.5 *Comparison of simulated fluoroscopy arteries and gold standard arteries.*

(A) Gold standard arterial anatomy (yellow lines) and LV&RV surfaces (wine-red surfaces) from anterior view. (B) GS-artery and LV&RV surfaces from inferior view. (C) Simu-arteries (red lines) and GS-arteries (yellow lines) overlaid on simu-surface from anterior view. (D) Simu-arteries and GS-arteries from inferior view.

4.4 Evaluation of the artery-surface fusion using real patient data

Besides the technical evaluation via computer simulation, this section explains the clinical feasibility of the image-guided system via real patient data. 30 patients who

underwent SPECT MPI, fluoroscopy angiography, and CT angiography were enrolled. All the SPECT images and fluoroscopy angiograms were processed and fused using the modules of artery reconstruction, LV surface extraction, and artery-surface fusion in the image-guided system. The CT epicardial surfaces and arteries were used as the gold standard to evaluate the accuracy of artery-surface fusion. The locations of fluoroscopy and CT arteries on the SPECT LV epicardial surface were compared.

4.4.1 Patient image acquisition

30 patients (21 males, and age = 63.0±8.68 years) were enrolled. All the patients had either stable or exertional angina before they underwent SPECT MPI, fluoroscopy angiography, and CT angiography.

SPECT scan was performed approximately 30 min after injection of 20 to 30 mCi of Tc-99m sestamibi. With a standard resting and stress protocol, SPECT images were acquired on a dual-headed camera (CardioMD, Philips MedicalSystems, Milpitas, California) with the acquisition parameters: 20% energy window around 140 KeV, 180˚ orbit, 32 steps with 25s per step, 8-bin gating, and 64 projections per gate. The acquired SPECT images have a resolution of $6.4 \times 6.4 \times 6.4$ mm^3.

Fluoroscopic coronary arteriography was performed using Philips system. All patients received aspirin (300mg) and ticlopidine (180mg) or Clopidogrel (300mg) before the test. Angiography data was acquired from the standard left coronary arteries (LCA) and right coronary arteries (RCA) views after intracoronary nitroglycerin injection. Clinical treatments included percutaneous transluminal coronary angioplasty (PTCA) wire cross coronary sclerosis, balloon dialect and stent transplant. Among the 30 patients, 19 patients

did not show RCA abnormality so each of them only took one RCA angiogram for less time exposure.

CT angiography was performed using a 64-slice Siemens CT scanner with a standard protocol. The acquired CT angiography images have a voxel size of 0.32 × 0.32 × 0.75 mm^3.

4.4.2 Comparison between fluoroscopy and CT arteries on LV epicardial surface

With the fluoroscopy angiograms, 3D arterial anatomies were reconstructed using my artery reconstruction tool. In LCA system, LMA, LAD, LCX, their branches (RI, D1, D1_b1, D2, D3, SEP1, LCX, OM1, OM2, OM3, and OM4) were reconstructed. In RCA system, RCA and its branches (PDA, PLB, and RMA) were reconstructed. It is noted that several angiograms had low image quality, such as messy noise, device artifacts, and low contrast. The deep learning segmentation model might fail to segment the arteries on those angiograms. Once it happened, manual correction was involved.

SPECT images were processed using my LV extraction tool. The LV apex and base slices were first manually identified, and then SPECT LV epicardial surfaces were automatically extracted.

CT is a widely used structural imaging technique, providing high precise anatomical information. The coronary arteries and LV surfaces extracted from CT were used as the gold standard to evaluate the accuracy of artery-surface fusion. CT angiograms were manually processed by experienced operators, who were blinded from the fluoroscopy angiograms and SPECT images. They manually extracted major arteries and LV&RV epicardial surfaces using 3D slicer[91], and then registered the CT LV surface with SPECT LV surface via aligning the landmarks (LV base, frontier, and inferior grooves) on both

LV surfaces. The transformation parameters of registration were also applied to the extracted CT arteries (LAD, LCX, PDA, PLB, and their branches) which travels on the LV epicardial surface, and therefore the CT arteries were closely aligned to the SPECT LV surface. The aligned CT arteries were overlaid onto the SPECT LV epicardial surface and used as the gold standard to evaluate artery-surface fusion. *Figure 4.6* is an example illustrating the comparison of the fluoroscopy and aligned CT arteries on the SPECT LV surface.

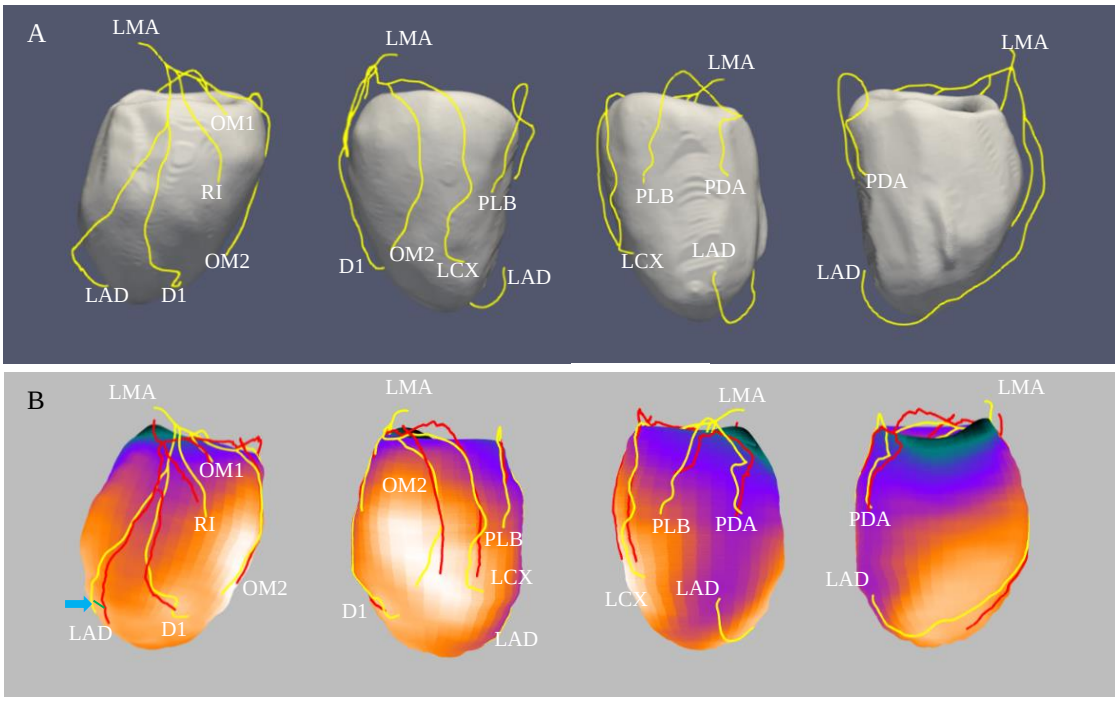

Figure 4.6 *Comparison between fluoroscopy and CT arteries on SPECT LV epicardial surface.*

(A) Coronary arteries (yellow lines) on the CT LV epicardial surface; (B) Coronary arteries from CT and fluoroscopy angiograms (red lines) overlaid on the SPECT LV epicardial surface. The Green line (illustrated by the blue arrow) represents the mismatch error between paired fluoroscopy and CT artery points. LMA = left main artery; LAD = left anterior descending; RI = ramus intermedius; D1 = diagonal branch 1; LCX = left circumflex; OM1 = obtuse marginal 1; OM2 = obtuse marginal 2; PDA = posterior descending artery; PLB = posterolateral branch.

In order to compare CT and fluoroscopy arteries, the CT and fluoroscopy artery points on the SPECT epicardial surface need to be paired. The fluoroscopy artery points were roughly fitted to a curve that can generally represent the fluoroscopy artery curve, as the blue line illustrated in *Figure 4.7*. From starting to end points of the curve, parallel planes perpendicular to the curve were continuously generated. If both fluoroscopy and CT artery points were located between any two adjacent parallel planes, they were deemed as paired fluoroscopy and CT artery points. The distance between them was computed.

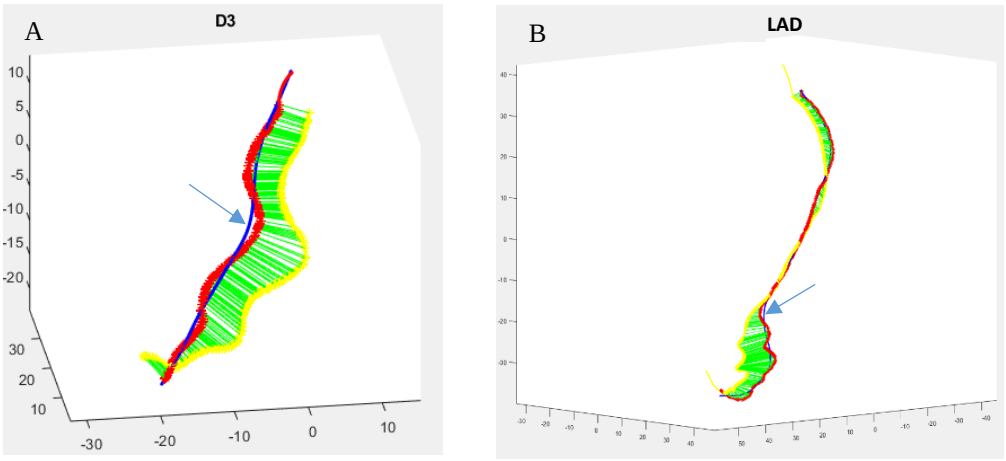

Figure 4.7 *Paring the CT and fluoroscopy artery points on SPECT LV surface for comparison*

(A) Paring CT artery (yellow line) and fluoroscopy artery (red line) points for the third diagonal artery. D3 = the third diagonal branch artery. (B) Paring CT and fluoroscopy artery points for left anterior descending artery (LAD). Green lines are the mismatch errors between paired fluoroscopy and CT artery points

4.4.3 Metrics to evaluate the accuracy of artery-surface fusion

After paring CT and fluoroscopy arteries, two metrics were used to assess the accuracy of artery-surface fusion. The first one is distance-based mismatch error between CT and fluoroscopy arteries on the SPECT LV epicardial surface. It stands for the mean distance between paired CT and fluoroscopy artery points, as the green lines illustrated in *Figure*

4.7. If the fluoroscopy and CT artery lengths were different, the distances were only computed when both of them are paired in the same parallel planes.

The second metric for the assessment of artery-surface fusion is a segment-based Kappa agreement rate using AHA 17-segment model[92][93]. The AHA 17-segment model divides the LV into 17 segments consisting of 6 basal, 6 mid, 4 apical, and an apical cap. Based on this model, the SPECT epicardial surface was divided into 17 segments. The segments that both fluoroscopy and artery arteries present were recorded and used to compute the Kappa agreement rate.

4.5 Results

4.5.1 Accuracy of artery-surface fusion using computer simulation

For the technical evaluation with the simulation data, Table 4.1 lists the distance-based mismatch errors between simu-arteries and GS-arteries overlaid on the simu-LV surface. In the LCA system, LMA, LAD, D1, and LCX had mismatch errors of 3.47±2.17, 2.30±1.74, 2.48±0.42, and 1.18±0.61 (unite: mm), respectively. A total of 368 simu-GS-artery point pairs were evaluated for LCA, overall mismatch error is 1.86±1.43mm (min: 0.04, max 6.87). In the RCA system, due to the absence of PLB artery, only PDA artery was evaluated. PDA had a mismatch error of 2.21±2.25mm (min: 0.05, max 10.74).

Table 4.1

Distance-based mismatch errors between simulation fluoroscopy and phantom arteries on the PET surface

LCA system	Point pairs	Mean±SD(mm)	Minimum	Maximum
LMA	11	3.47±2.17	0.72	6.85
LAD	163	2.30±1.74	0.04	6.87
D1	34	2.48±0.42	1.67	3.27
LCX	160	1.18±0.61	0.04	3.15
Overall	368	1.86±1.43	0.04	6.87
RCA system	Point pairs	Mean±SD(mm)	Minimum	Maximum
PDA	104	2.21±2.50	0.05	10.74

Abbreviation: LMA = left main artery; LAD = left anterior descending; D1 = diagonal branch 1; LCX = left circumflex; PDA = posterior descending artery.

4.5.2 Accuracy of the artery-surface fusion using real patient data

Table 4.2 lists the distance-based mismatch errors between fluoroscopy and CT arteries on the SPECT LV surfaces in 30 patients' data. In the LCA system, the mismatch errors of LAD and its branches, RI, D1, D1_b1, D2, D3, and SEP1, were 3.52±2.80, 3.12±2.54, 3.43±2.95, 3.78±3.40, 3.58±3.13, 5.70±2.13, and 5.17±2.02 (unit: mm), respectively. The mismatch errors of LCX and its branches, OM1, OM2, OM3, and OM4, were 4.72±3.40, 3.06±2.42, 3.69±2.76, 4.81±3.12, and 3.88±2.80 (unit: mm), respectively. The mismatch error of LMA was 4.91±2.65mm. The overall mismatch error of LCA was 3.84±3.15mm (min: 0, max: 20.46). In the RCA system, the mismatch errors of PDA, PLB, and PLB1 were 5.90±3.92, 4.83±2.89, and 7.80±2.84 (unit: mm). The overall mismatch error of RCA was 5.55±3.64mm (min: 0.11, max: 24.25).

Table 4.2

Distance-based mismatch errors between the fluoroscopy and CT arteries

LCA system	Point pairs	Mean ± SD(mm)	Minimum	Maximum
LMA	545	4.91±2.65	0.33	10.46
LAD	9005	3.52±2.80	0	19.41
RI	1104	3.12±2.54	0.03	18.39
D1	3608	3.43±2.95	0	20.46
D1_b1	132	3.78±3.40	0.07	11.73
D2	1696	3.58±3.13	0.01	13.65
D3	264	5.70±2.13	0.12	9.05
SEP1	130	5.17±2.02	3.20	12.71
LCX	6192	4.72±3.40	0	18.86
OM1	2029	3.06±2.42	0	9.61
OM2	1926	3.69±2.76	0	16.97
OM3	965	4.81±3.12	0.02	20.25
OM4	156	3.88±2.80	0.09	9.81
Overall	27752	3.84±3.15	0	20.46
RCA system	Point pairs	Mean ± SD(mm)	Minimum	Maximum
PDA	855	5.90±3.92	1.02	24.25
PLB	574	4.83±2.89	0.01	21.66
PLB1	152	7.80±2.84	2.69	13.52
Overall	1581	5.55±3.64	0.11	24.25

Abbreviation: LMA = left main artery; LAD = left anterior descending; RI = ramus intermedius artery; D1 = the first diagonal artery; D1_b1= branch of the first diagonal artery, D2 = the second diagonal artery; D3 = the third diagonal artery; SEP1 = the first septal perforator artery; LCX = left circumflex; OM1 = the first obtuse marginal artery; OM2 = the second obtuse marginal artery; OM3 =the third obtuse marginal artery; OM4 =the fourth obtuse marginal artery; PDA = posterior descending artery; PLB = posterolateral branch artery; PLB_1 = the first branch of posterolateral branch artery.

Table 4.3 lists the segment-based mismatch error between fluoroscopy and CT arteries on the SPECT LV surface. In the LCA system, the Kappa agreement rates of LAD and its branches, RI, D1, D1_b1, D2, D3, and SEP1, were 0.87, 0.92, 0.92, 1.00, 0.91, 1.00, and 1.00, respectively. The Kappa agreement rates of LCX and its branches, OM1, OM2, OM3, and OM4, were 0.91, 0.96, 0.91, 0.93, and 1.00, respectively. The overall Kappa agreement

rate of LCA was 0.91. In the RCA system, the Kappa agreement rates of PDA, PLB, and PLB1 were 0.76, 0.88, and 0.73. The overall Kappa agreement rate of RCA was 0.80.

Table 4.3

Segment-based mismatch error between the fluoroscopy and CT arteries

LCA system		CT-Y	CT-N	**LCA system**		CT-Y	CT-N
LAD	Fluoro-Y	115	12	SEP1	Fluoro-Y	5	0
	Fluoro-N	12	371		Fluoro-N	0	29
	Kappa (95%CI)	0.87 (0.83-0.92)			Kappa (95%CI)	1.00 (1.00-1.00)	
RI	Fluoro-Y	13	1	LCX	Fluoro-Y	92	7
	Fluoro-N	1	138		Fluoro-N	7	404
	Kappa (95%CI)	0.92 (0.81-1.03)			Kappa (95%CI)	0.91 (0.87-0.96)	
D1	Fluoro-Y	55	5	OM1	Fluoro-Y	29	1
	Fluoro-N	5	394		Fluoro-N	1	275
	Kappa (95%CI)	0.92 (0.87-0.98)			Kappa (95%CI)	0.96 (0.91-1.01)	
D1_b1	Fluoro-Y	5	0	OM2	Fluoro-Y	24	2
	Fluoro-N	0	29		Fluoro-N	2	210
	Kappa (95%CI)	1.00 (1.00- 1.00)			Kappa (95%CI)	0.91 (0.83-1.00)	
D2	Fluoro-Y	28	3	OM3	Fluoro-Y	14	1
	Fluoro-N	3	205		Fluoro-N	1	120
	Kappa (95%CI)	0.91 (0.82-0.99)			Kappa (95%CI)	0.93 (0.82-1.02)	
D3	Fluoro-Y	4	0	OM4	Fluoro-Y	2	0
	Fluoro-N	0	30		Fluoro-N	0	15
	Kappa (95%CI)	1.00 (1.00–1.00)			Kappa (95%CI)	1.00 (1.00–1.00)	
						CT-Y	CT-N
LCA Overall		Fluoro-Y		386		30	
		Fluoro-N		31		2222	
		Kappa (95%CI)		0.91 (0.89-0.93)			
RCA system		CT-Y	CT-N	**RCA system**		CT-Y	CT-N
PDA	Fluoro-Y	11	3	PLB_b1	Fluoro-Y	3	1
	Fluoro-N	3	119		Fluoro-N	1	63
	Kappa (95%CI)	0.76 (0.57-0.95)			Kappa (95%CI)	0.73 (0.37-1.10)	
PLB	Fluoro-Y	7	2				
	Fluoro-N	2	108				
	Kappa (95%CI)	0.88 (0.71-1.05)					
						CT-Y	CT-N
RCA Overall		Fluoro-Y		22		5	
		Fluoro-N		5		291	
		Kappa (95%CI)		0.80 (0.67-0.92)			

Abbreviation: CI = confidence interval; CT-N = total number of segments without CT arteries; CT-Y = total number of segments with CT arteries; Fluoro-N = total number of segments without fluoroscopy arteries; Fluoro-Y = total number of segments with fluoroscopy arteries; other abbreviations as in Table 4.2.

4.6 Discussion

This chapter explains my fusion approach to integrate 3D artery anatomy with LV epicardial surface. The technical accuracy and clinical feasibility of this fusion approach were evaluated. The computer simulation technically evaluated the accuracy of the artery-surface fusion. The mean distance-based mismatch error of 1.86±1.43mm for LCA and 2.21±2.50mm for RCA, which validated its technical accuracy. The clinical evaluation in 30 patients showed that artery-surface fusion had mismatch errors of 3.84±3.15mm for LCA and 5.55±3.64mm for RCA, which is much smaller than the segment size of the AHA 17-segment model (~30 × 30mm^2)[92]. The Kappa test showed good agreement rates of the fluoroscopy and CT artery locations on the SPECT LV surface. Accordingly, the image-guided system including artery reconstruction, LV surface extraction and artery-surface fusion showed high technical accuracy and strong clinical feasibility to guide MR decision-making.

4.6.1 Advantages of S-ICP for vessel anatomy and LV epicardial surface

The previous studies on the artery-surface fusion showed limitations. In landmark-based registration method[35][36], only the major vessels were aligned to the LV surface. As Faber et al. [35]proposed, they aligned the LAD, LCX, and PDA to the anterior interventricular groove, left atrioventricular groove, and inferior interventricular groove, respectively. However, the branches and extensions of the major vessels may not be accurately registered. Besides, a pair of scale-matched arterial anatomy and LV epicardial surface are essential but difficult to obtain. In the rigid ICP registration algorithm[39][40], although they aligned all the vessel points on the LV surface, the fusions were still rigid transformations. When the vessel model and LV surface model have scale mismatches, the

fusions may fail. Compared to the landmark-based and rigid ICP registration algorithms, S-ICP showed unique advantages. It adjusts the scale of arterial anatomy up or down to match the scale of LV surface and then complete the fusion by minimizing the squared distance between them. The non-rigidly registration allows more flexible registrations between arteries and LV surface rather than between the end-diastolic angiograms and SPECT images of the last gate. It is well known that the artery system has complicated anatomical structures so that there are intricate overlaps on the fluoroscopy angiograms from different views. It is not guaranteed that arteries on the end-diastolic frames have the fewest overlaps. In some cases, angiograms between end-systolic and end-diastolic time points show fewer artery overlaps from certain views. The reconstructed 3D arterial anatomy using these angiograms shows more precise contour information and helps doctors make more accurate decisions for MR. Although it may have a big scale mismatch to the LV surface, S-ICP can automatically adjust the scale of artery model and then accurately complete the artery-surface fusion, which enhances the clinical applicability of the fusion tool.

4.6.2 Local minimal convergence of S-ICP and preset scale factor S

As mentioned in Section 4.2, S-ICP monotonically converges to a local minimum. I used the registration parameters provided by the landmark-based method to initialize the registration of S-ICP, which performed well and enabled the S-ICP to avoid convergence to a local minimum. SPECT LV surface is usually an axisymmetric object. Without a reasonable initialization, it was difficult for S-ICP to capture significant morphological features from LV surface to register with 3D artery anatomy. Hence, an inappropriate or locally convergent registration may achieve. The landmark-based registration aligned the

major vessels to the corresponding interventricular and atrioventricular grooves, which initially completed a morphological alignment between LV surface and artery anatomy. S-ICP adjusted the scale of artery and complete the registration based on the current morphological features of LV, which ensured an accurate and global optimized registration rather than trapping into a local minimum.

In addition, scale *S* is another factor that affects the convergence of S-ICP registration. In order to avoid local minimum convergence, *S* should cover the range of minimum and maximum scale mismatches. I set the scale *S* within the range of 0.85 to 1.2. Most 3D arterial anatomy was reconstructed using end-diastolic angiograms. All the LV surfaces were extracted from ungated SPECT image. The scale mismatches between the two reconstructed objects were small. Hence, the scale factor range ($S \epsilon [0.85, 1.2]$) can cover the scale transformations. With this constraint and initialization by landmark-based approach, S-ICP accomplished an appropriate and globally optimized artery-surface fusion.

4.6.3 Clinical applicability

In my dissertation project, the fusion between fluoroscopy angiography and SPECT MPI using the image-guided system provided not only anatomical information regarding artery stenosis locations and degrees but also functional information on pathophysiologic lesion severity. The artery-surface fusion allows physicians to target the lesion and assess the corresponding regional myocardial viability for more accurate MR decision-making. It will help eliminate the equivocal MR decisions based on coronary fluoroscopy angiography that generally underestimates or overestimates the myocardial ischemia severity and extent, resulting in mismatches between fluoroscopy angiography and SPECT. *Figure 4.8*

shows two patient cases that have mismatched artery stenosis and perfusion abnormality among the 30 patients. For the first patient, fluoroscopy angiography showed mid-LAD stenosis of 80% (*Figure 4.8* A&B), however, the corresponding myocardial perfusion on the artery-surface fusion was normal (*Figure 4.8* C&D). After a successful stent-PCI guided by fluoroscopy angiography, obvious clinical system relief was not observed for this patient, which resulted in an unnecessary interventional procedure. For the second patient, fluoroscopy angiography did not show any structural narrowing of arteries (*Figure 4.8* E&F) but the corresponding myocardium of distal LAD on the artery-surface fusion showed an intermediate perfusion abnormality. This specific abnormal perfusion may be caused by Minorca syndrome[94], slow coronary flow, or myocarditis. Although there is no obvious structural stenosis identified, the perfusion abnormality in the apex region may result in a bad clinical prognosis after a long-term follow-up. Artery-surface fusion provides more evidence for physicians to choose optimal medical treatment. Moreover, for patients with matched artery stenosis and perfusion abnormality, 3D fusion helps physicians confirm the pathophysiologic lesion severity corresponded to the stenosis and increases their diagnostic confidence to categorize lesions and open the stenosis. Therefore, artery-surface fusion shows clinical significance for MR decision-making that helps avoid unnecessary interventional procedures, provides added evidence for optimal medical treatment, and increases the diagnostic confidence for lesion categorization or stent implantation.

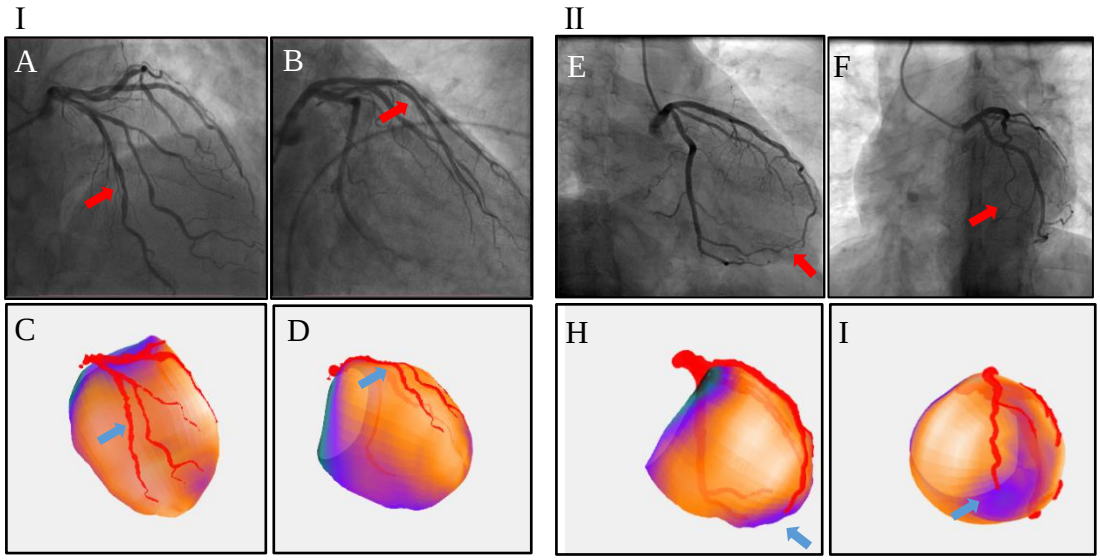

Figure 4.8 *Concordance of artery stenosis and perfusion abnormality.*

Patient I: (A) and (B) Fluoroscopy angiograms from two different views; (C) and (D) artery-surface fusions from the same views of (A) and (B). Patient II: (A) and (B) Coronary angiograms; (H) and (I) artery-surface fusions. Red arrows show stenotic lesion on fluoroscopy angiograms and blue arrows show the corresponding myocardial perfusion on artery-surface fusion.

Two essential factors may affect the applicability of the image-guided system. First, relatively clear interventricular landmarks on the short-axis image (*Figure 4.1*) are needed for the initial registration of the artery-surface fusion. Fortunately, these landmarks constantly exist and can be identified in CAD patients. Second, for 3D artery reconstruction, the spatial angle gap between the primary and secondary projection views preferably ranges from 45˚ to 145˚. The closer to orthogonal is, the better reconstruction is. LCA angiography can usually meet this condition from standard views by checking LAD and LCX arteries. RCA angiography also meets this condition in most cases but is limited to the cases of which the spatial angle gaps are out of the range. Once it happened, one more angiogram in the range is for more accurate 3D reconstruction.

The clinical validation in the 30 patients confirmed the applicability of 3D image-guided system. The artery-surface fusion had a much smaller mean mismatch error compared to the segment size of the American Heart Association (AHA) 17-segment model (~30 × 30mm^2). Even the maximum mismatch errors 20.46mm (LAD in the LCA system) and 24.25mm (PDA in the RCA system) were also in the range. Moreover, overall Kappa agreement rates of 0.91 for LCA and 0.80 for RCA also affirms the accuracy and applicability of the 3D image-guided system.

CHAPTER V – CONCLUSIONS

5.1 Summary and conclusions

The fusion between SPECT images and fluoroscopy angiograms has been a challenging task in the field of medical image processing. Several computational and mathematic approaches have been proposed for this fusion task of the 2D and 3D modalities, such as landmark-based, non-rigid ICPs, and deep learning-based approaches. All of these approaches have limitations. Landmark-based method cannot guarantee appropriate alignment for all vessels, except the major ones. Non-rigid ICPs may fail when registering two scale mismatched objects. Deep learning-based algorithms complete 2D/3D fusion via registering 2D image with 2D projection of 3D volume, which cannot provide 3D arterial anatomical structures. Another drawback is the difficulty of obtaining well-aligned multi-modal image pairs for network training. An accurate, robust, and deformable fusion of SEPCT and fluoroscopy images is still needed. In my work, I completed the fusion task with the following three steps.

The first step was to reconstruct 3D arterial anatomy from dual 2D fluoroscopy angiograms. It includes image segmentation, computer stereo geometry calibration, and artery reconstruction. A deep learning model was trained to segment arteries and a series of image processing techniques were executed to obtain artery centerlines and contour diameters. A mathematic model was created based on X-ray angiography and pinhole camera models. Based on the model, an objective function aiming to calibrate 15 intrinsic and extrinsic geometry parameters were created and optimized using a Levenberg-Marquardt algorithm. The optimized parameters were used to calibrate the imaging geometry system and vessel points were paired using an epipolar constraint-based

approach. 3D artery centerlines were therefore reconstructed using paired vessel points and artery surface was constructed using quadrangles. A computer simulation using GATE simulator and X-CAT phantom was executed to evaluate the accuracy of this reconstruction algorithm. The results showed that the average distance between reconstructed and gold standard arteries was small, indicating high precise 3D artery reconstruction.

The second step was to extract the LV epicardial surface from SPECT images. A dynamic programming-based algorithm was improved. Long-axis SPECT images were first transformed from Cartesian to polar coordinates and then the gradients of the polar image were calculated. LV epicardial contour in the polar image was identified via searching for the maximal gradients using the dynamic programming algorithm and then transformed back to Cartesian coordinates. Myocardial perfusion data was finally rendered on the LV epicardial surface. A computer simulation was executed to evaluate the accuracy of LV surface extraction algorithm. The experiment results showed that the average distance-based mismatch error between reconstructed and gold standard LV surface was small.

The third step was to fuse the reconstructed 3D arterial anatomy and the extracted LV epicardial surface. An improved S-ICP algorithm was used to complete the fusion. Two strategies from rough to fine registrations were implemented. Landmark-based registration was first used to roughly align the major arteries with LV surface. Non-rigid alignment by S-ICP was executed to refine the registration. The registered arteries were finally overlaid onto the LV surface to complete the artery-surface fusion. In order to evaluate the accuracy of the fusion, a computer simulation-based validation was executed. The validation result

showed a small distance-based mismatch error between arteries and gold standard. Accordingly, the artery reconstruction, LV surface extraction, and 3D fusion approaches together establish an image-guided system to guide MR. To evaluate the clinical feasibility of the image-guided system, a clinical validation was conducted. SPECT images and fluoroscopy angiograms in 30 patients were processed and fused using the image-guided system. The results showed a small distance-based mismatch error and a high segment-based Kappa agreement rate between fluoroscopy and CT arteries (gold standard).

To summarize, a 3D image-guided system has been developed that reconstructs 3D LV arterial anatomy from fluoroscopy angiograms, extracts LV epicardial surface from SPECT images, and fuses them for guiding MR. The technical accuracy and clinical feasibility have been validated via computer simulation and real patient data. The image-guided system is technically accurate to guide revascularization decision-making and clinically feasible to be used in the catheterization laboratory.

5.2 Future directions

There are three possible areas that I can work on in the future with respect to this topic.

- Implementing semantic segmentation of coronary arteries. The current segmentation model is a binary classification: foreground for artery and background for others. Since the binary segmentation model cannot distinguish the arterial topology, the artery topology is completed via manual identification. Semantic segmentation model can address this issue, which will semantically extract the vessels and enhance the ease of use of the 3D image-guided system.

- Improving the artery reconstruction by adding another view to the mathematic reconstruction model. The current reconstruction algorithm requires a minimum spatial angle gap between the primary and secondary views. Adding another view to the mathematic model will not only take off this limitation, but also enhance the accuracy of 3D artery reconstruction. With the semantic segmentation of arteries, the added angiogram from another view would not require more extra manual identification for vessel topology.
- Improving the extraction of LV epicardial surface. The dynamic programming-based LV surface extraction approach is sensitive to noise caused by abnormal organ uptake. The noise may deteriorate or lead to failed LV surface extraction. Improvement work on the algorithm is still needed to enhance the robustness of this algorithm.

APPENDIX A - User interfaces of 3D artery reconstruction tool

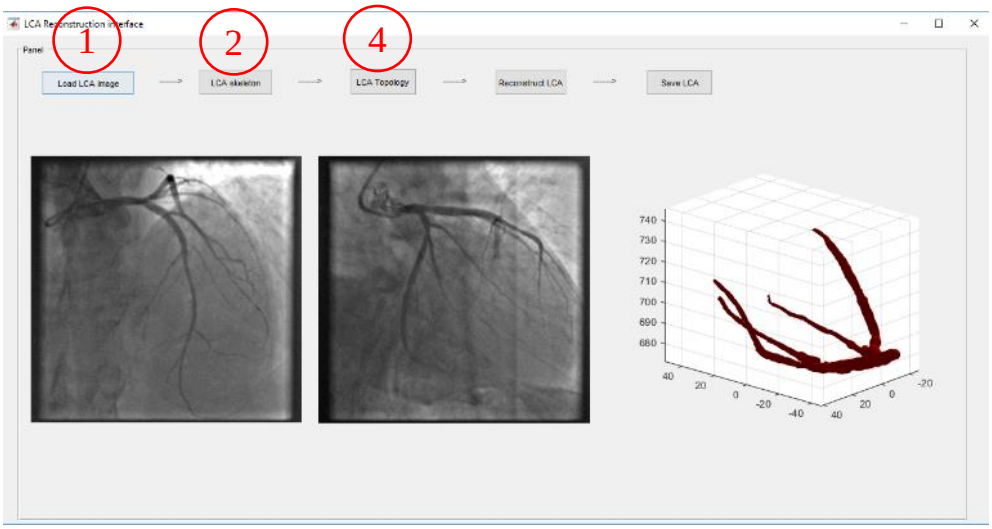

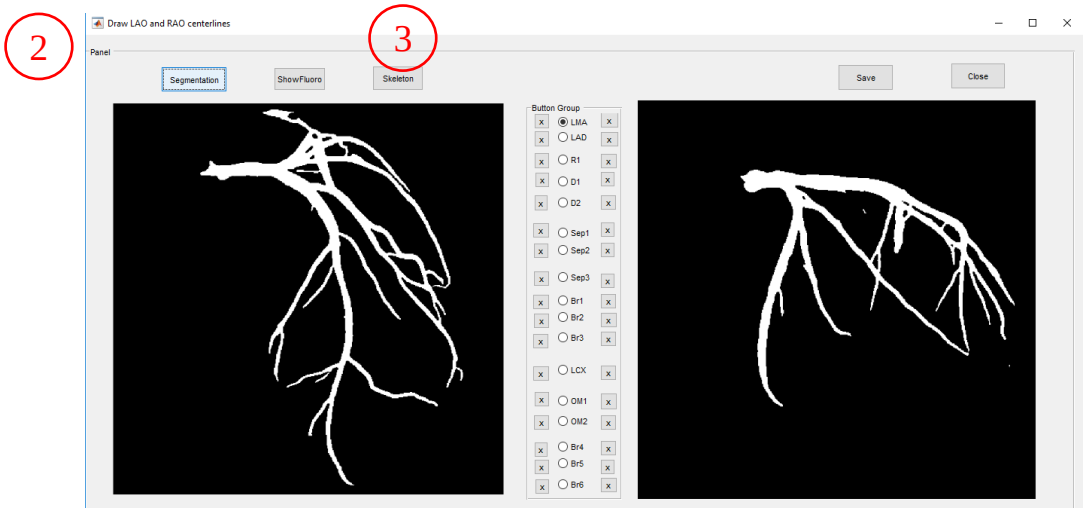

3

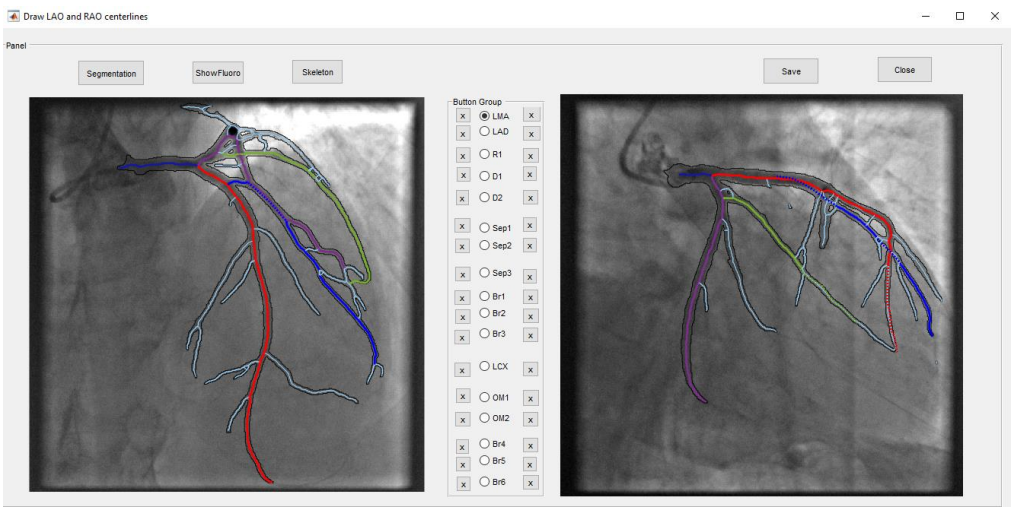
Draw LAO and RAO centerlines
Panel
Segmentation
ShowFluoro
Skeleton
Save
Close
Button Group
LMA
LAD
R1
D1
D2
Sep1
Sep2
Sep3
Br1
Br2
Br3
LCX
OM1
OM2
Br4
Br5
Br6

4

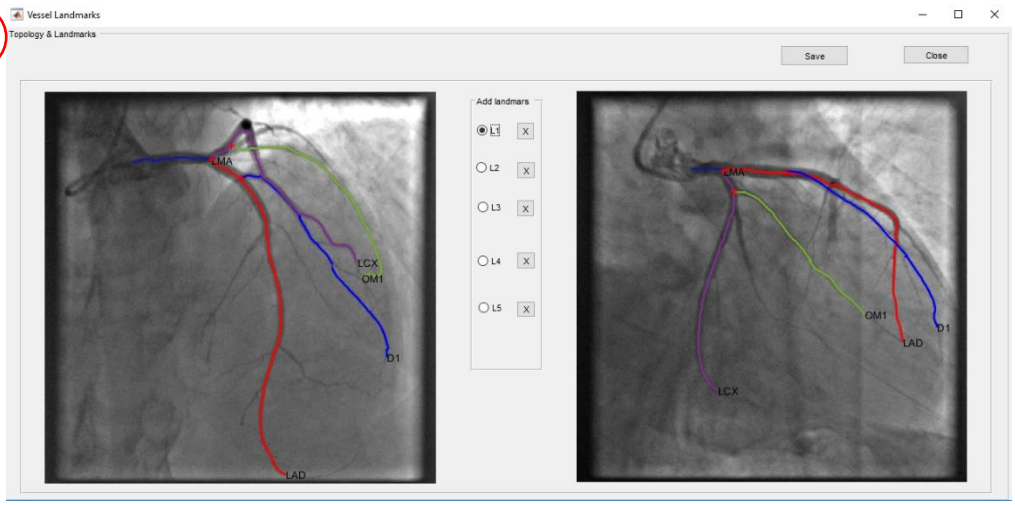
Vessel Landmarks
Topology & Landmarks
Save
Close
Add landmars
L1
L2
L3
L4
L5
LMA
LCX
OM1
D1
LAD

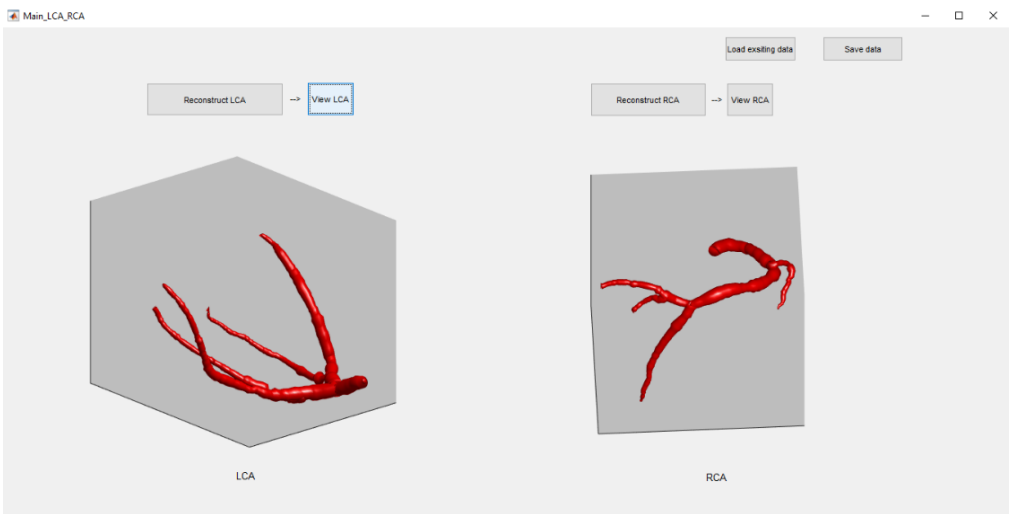
Main_LCA_RCA
Load exsiting data
Save data
Reconstruct LCA
View LCA
Reconstruct RCA
View RCA
LCA
RCA

APPENDIX B - User interfaces of 3D LV surface extraction tool

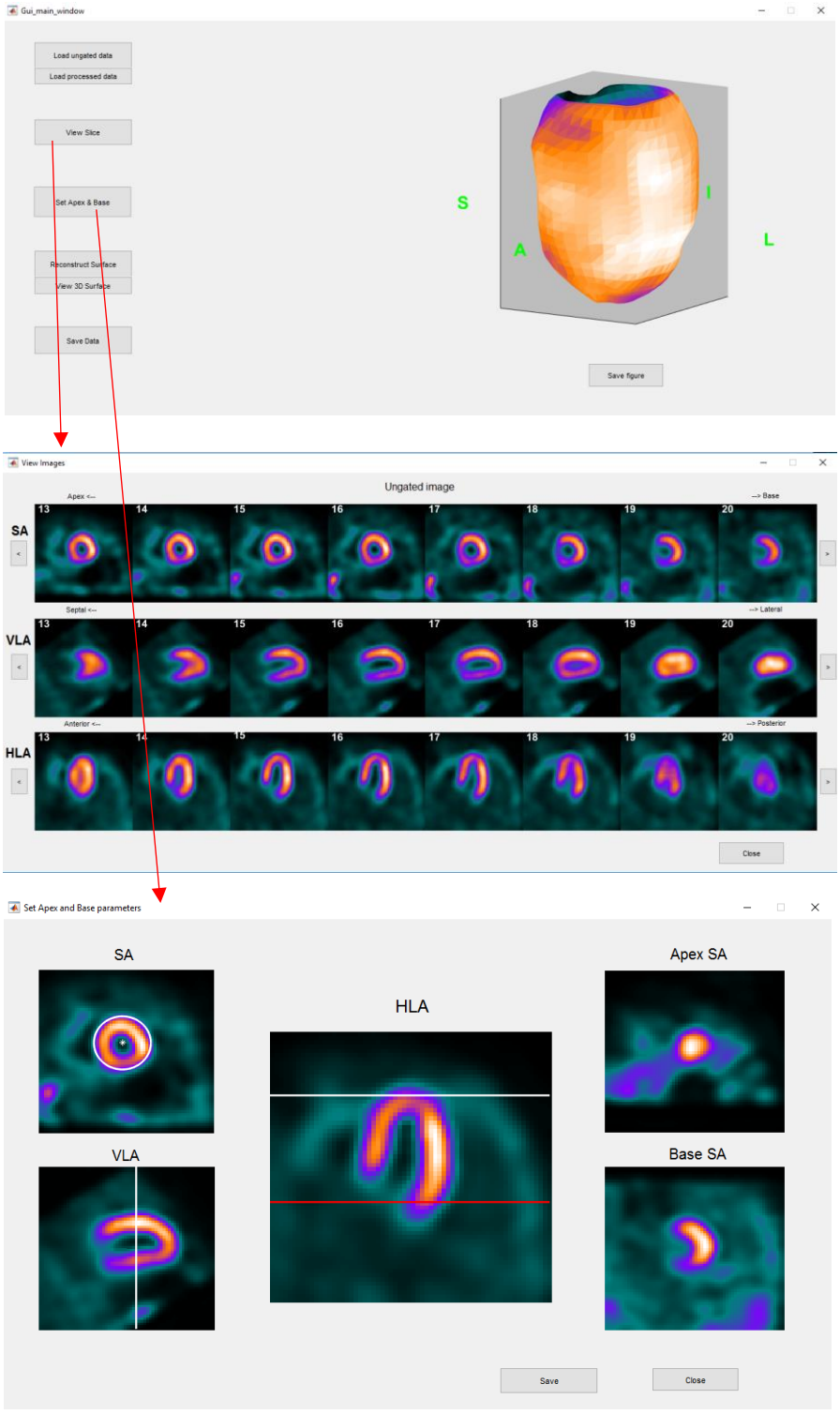

APPENDIX C - User interfaces of fusion tool

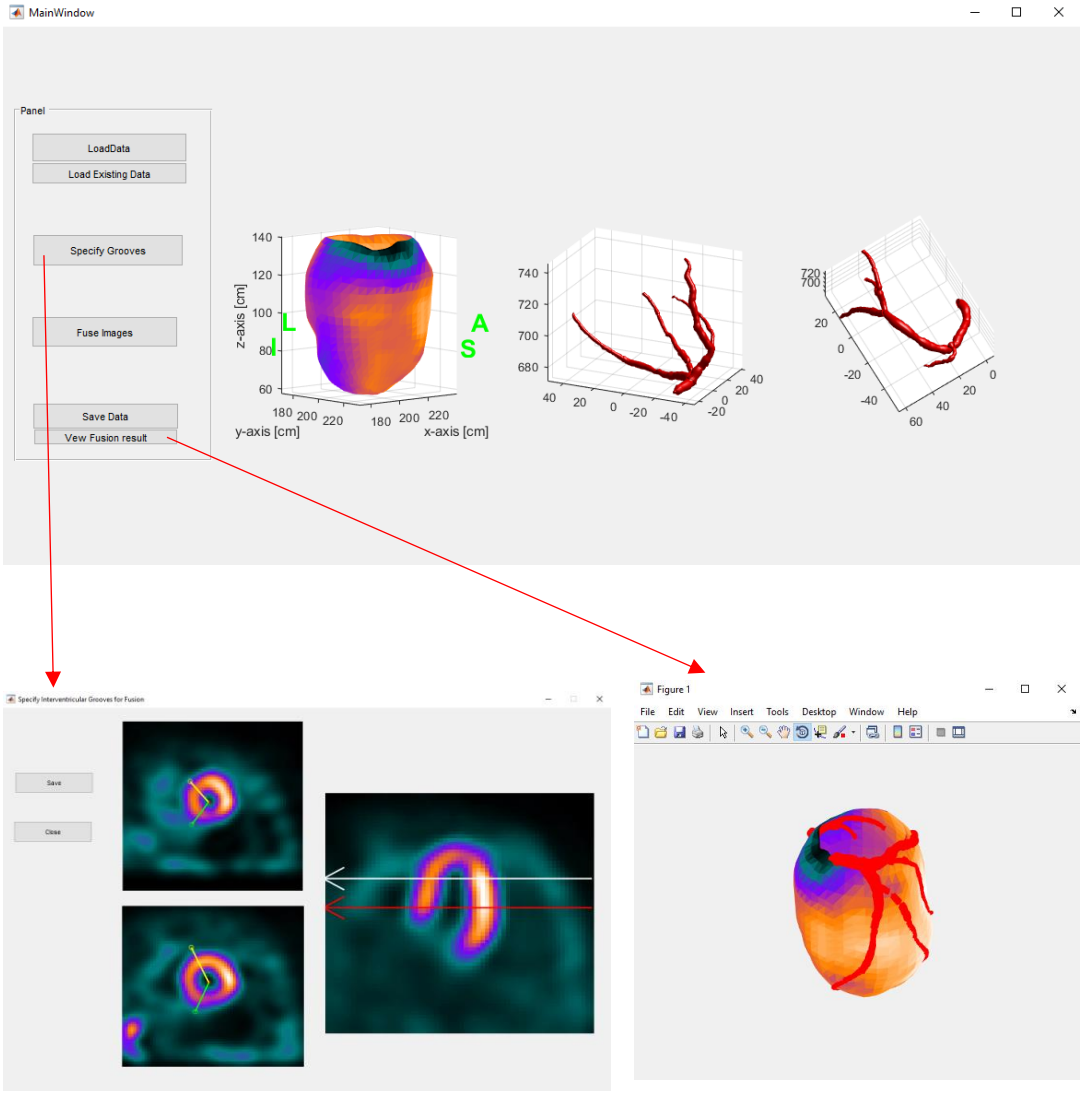

REFERENCES

[1] D. S. Benjamin EJ, Blaha MJ, Chiuve SE, Cushman M, "Heart Disease and Stroke Statistics 2017 At-a Glance," *Assoc. Am. Hear. Am. Stroke Assoc.*, 2017.

[2] "Heart Disease and Stroke Statistics-2019 At-a-Glance Heart Disease, Stroke and other Cardiovascular Diseases."

[3] "Coronary Artery Disease: Causes, Symptoms, Diagnosis & Treatments." [Online]. Available: https://my.clevelandclinic.org/health/diseases/16898-coronary-artery-disease. [Accessed: 26-Apr-2020].

[4] A. Cassar, D. R. Holmes, C. S. Rihal, and B. J. Gersh, "Chronic coronary artery disease: Diagnosis and management," in *Mayo Clinic Proceedings*, 2009, vol. 84, no. 12, pp. 1130–1146.

[5] P. A. McCullough, "Coronary artery disease," *Clin. J. Am. Soc. Nephrol.*, vol. 2, no. 3, pp. 611–616, May 2007.

[6] "Medical Management of Stable Coronary Artery Disease - American Family Physician." [Online]. Available: https://www.aafp.org/afp/2011/0401/p819.html#afp20110401p819-b1. [Accessed: 27-Apr-2020].

[7] "Medical Management of Stable Coronary Artery Disease - American Family Physician." [Online]. Available: https://www.aafp.org/afp/2011/0401/p819.html. [Accessed: 04-May-2020].

[8] W. Dos, S. Ker, T. Helena, P. Nunes, M. S. Nacif, and C. T. Mesquita, "Practical Implications of Myocardial Viability Studies."

[9] “2018 ESC/EACTS Guidelines on myocardial revascularization | European Heart Journal | Oxford Academic.” [Online]. Available: https://academic.oup.com/eurheartj/article/40/2/87/5079120. [Accessed: 04-May-2020].

[10] “US5389096A - System and method for percutaneous myocardial revascularization - Google Patents.” [Online]. Available: https://patents.google.com/patent/US5389096A/en. [Accessed: 04-May-2020].

[11] “Coronary angioplasty and stents - Mayo Clinic.” [Online]. Available: https://www.mayoclinic.org/tests-procedures/coronary-angioplasty/about/pac-20384761. [Accessed: 04-May-2020].

[12] P. W. Serruys *et al.*, “Percutaneous Coronary Intervention versus Coronary-Artery Bypass Grafting for Severe Coronary Artery Disease,” *n engl j med*, vol. 10, no. 5, pp. 961–72, 2009.

[13] “Coronary Artery Bypass Graft Surgery | Johns Hopkins Medicine.” [Online]. Available: https://www.hopkinsmedicine.org/health/treatment-tests-and-therapies/coronary-artery-bypass-graft-surgery. [Accessed: 04-May-2020].

[14] V. Guru, G. M. Anderson, S. E. Fremes, G. T. O’Connor, F. L. Grover, and J. V. Tu, “The identification and development of Canadian coronary artery bypass graft surgery quality indicators,” *J. Thorac. Cardiovasc. Surg.*, vol. 130, no. 5, pp. 1257.e1-1257.e11, Nov. 2005.

[15] A. J. Hartz and E. M. Kuhn, “Comparing hospitals that perform coronary artery bypass surgery: The effect of outcome measures and data sources,” *Am. J. Public Health*, vol. 84, no. 10, pp. 1609–1614, 1994.

[16] S. V. P. Hospital, “Coronary Angiogram & Percutaneous Coronary Intervention (PCI) A Guide for Patients.” [Online]. Available: https://images.app.goo.gl/Lg7oMufULR2b8CAM9. [Accessed: 07-May-2020].

[17] “Coronary Artery Bypass Surgery: List of Best Doctors India | MedcureIndia.” [Online]. Available: https://medcureindia.com/treatments/cardiology/coronary-artery-bypass-surgery-cabg-at-top-hospital-from-best-surgeons. [Accessed: 07-May-2020].

[18] “Myocardial revascularization in women. - PubMed - NCBI.” [Online]. Available: https://www.ncbi.nlm.nih.gov/pubmed/15227479. [Accessed: 04-May-2020].

[19] G. Mariscalco *et al.*, “Prior Percutaneous Coronary Intervention and Mortality in Patients Undergoing Surgical Myocardial Revascularization: Results From the E-CABG (European Multicenter Study on Coronary Artery Bypass Grafting) With a Systematic Review and Meta-Analysis.,” *Circ Cardiovasc Interv*, vol. 11, no. 2, p. e005650, Feb. 2018.

[20] W. E. Boden *et al.*, “Optimal medical therapy with or without PCI for stable coronary disease,” *N. Engl. J. Med.*, vol. 356, no. 15, pp. 1503–1516, Apr. 2007.

[21] “A Randomized Trial of Therapies for Type 2 Diabetes and Coronary Artery Disease,” *N. Engl. J. Med.*, vol. 360, no. 24, pp. 2503–2515, Jun. 2009.

[22] E. J. Velazquez *et al.*, “Coronary-Artery Bypass Surgery in Patients with Left Ventricular Dysfunction,” *N. Engl. J. Med.*, vol. 364, no. 17, pp. 1607–1616, Apr. 2011.

[23] J. Maddahi *et al.*, “Myocardial perfusion imaging with technetium-99m sestamibi SPECT in the evaluation of coronary artery disease,” *Am. J. Cardiol.*, vol. 66, no.

13, pp. E55–E62, Oct. 1990.

[24] A. K. Buck *et al.*, “SPECT/CT,” *Journal of Nuclear Medicine*, vol. 49, no. 8. Society of Nuclear Medicine, pp. 1305–1319, 01-Aug-2008.

[25] R. C. Hendel *et al.*, “Multicenter Clinical Trial to Evaluate the Efficacy of Correction for Photon Attenuation and Scatter in SPECT Myocardial Perfusion Imaging,” *Circulation*, vol. 99, no. 21, pp. 2742–2749, Jun. 1999.

[26] T. Hirai *et al.*, “Evaluation of myocardial infarct size in rat heart by pinhole SPECT,” *J. Nucl. Cardiol.*, vol. 7, no. 2, pp. 107–111, 2000.

[27] “Produced with the kind Support of Myocardial Perfusion Imaging (Revised Edition) A Technologist’s Guide.”

[28] T. Sharir *et al.*, “Survival benefit of coronary revascularization after myocardial perfusion SPECT: The role of ischemia,” *J. Nucl. Cardiol.*, 2019.

[29] “Home | The ISCHEMIA Study.” [Online]. Available: https://www.ischemiatrial.org/. [Accessed: 04-May-2020].

[30] S. Yandrapalli, A. Malik, and D. Jain, “SPECT myocardial perfusion imaging-based ischemia-guided early coronary revascularization improves survival: More fuel to the fire,” *Journal of Nuclear Cardiology*. Springer, pp. 1–4, 19-Dec-2019.

[31] J. A. Simonsen *et al.*, “Outcome of revascularisation in stable coronary artery disease without ischaemia: A Danish registry-based follow-up study,” *BMJ Open*, vol. 7, no. 8, Aug. 2017.

[32] M. Piccinelli, “Multimodality image fusion for diagnosing coronary artery disease,” *J. Biomed. Res.*, vol. 27, no. 6, pp. 439–451, 2013.

[33] H. Tang, S. Tang, and W. Zhou, “A Review of Image-guided Approaches for

Cardiac Resynchronisation Therapy," no. Icm, pp. 69–74, 2017.

[34] "The Radiology Assistant : Coronary anatomy and anomalies." [Online]. Available: https://radiologyassistant.nl/cardiovascular/coronary-anatomy-and-anomalies. [Accessed: 13-Apr-2020].

[35] T. L. Faber *et al.*, "Automatic unification of three-dimensional cardiac perfusion with three-dimensional coronary artery anatomy," in *Computers in Cardiology 1996*, pp. 333–336.

[36] W. Zhou *et al.*, "3D Fusion of LV Venous Anatomy on Fluoroscopy Venograms With Epicardial Surface on SPECT Myocardial Perfusion Images for Guiding CRT LV Lead Placement," *J Am Coll Cardiol Img*, vol. 7, no. 12, pp. 1239–1248, Dec. 2014.

[37] P. J. Besl and N. D. McKay, "A method for registration of 3-D shapes," *IEEE Trans. Pattern Anal. Mach. Intell.*, vol. 14, no. 2, pp. 239–256, Feb. 1992.

[38] T. L. Faber *et al.*, "Registration of multimodal 3D cardiac information using the iterative closest point approach," *Math. Model. Estim. Imaging*, vol. 4121, pp. 233–241, 2000.

[39] H. H. Babic, Odland, G. Olivier, C. Innovation, G. E. V. Ultrasound, and P. O. B. Blindern, "LEFT-VENTRICLE TO CORONARY VENOUS TREE 3D FUSION FOR CARDIAC RESYNCHRONIZATION THERAPY APPLICATIONS Aleksandar Babi ´," pp. 164–168, 2017.

[40] D. Toth *et al.*, "3D/2D Registration with superabundant vessel reconstruction for cardiac resynchronization therapy," *Med. Image Anal.*, vol. 42, pp. 160–172, Dec. 2017.

[41] J. Yang, H. Li, D. Campbell, and Y. Jia, “Go-ICP: A Globally Optimal Solution to 3D ICP Point-Set Registration,” *IEEE Trans. Pattern Anal. Mach. Intell.*, vol. 38, no. 11, pp. 2241–2254, May 2016.

[42] M. Panayiotou *et al.*, “A statistical method for retrospective cardiac and respiratory motion gating of interventional cardiac x-ray images,” *Med. Phys.*, vol. 41, no. 7, p. 071901, Jun. 2014.

[43] T. D. *et al.*, “3D/2D model-to-image registration by imitation learning for cardiac procedures,” *Int. J. Comput. Assist. Radiol. Surg.*, vol. 13, no. 8, pp. 1141–1149, 2018.

[44] G. Xu and Z. Zhang, *Epipolar Geometry in Stereo, Motion and Object Recognition*. 1996.

[45] J. Yang, Y. Wang, Y. Liu, S. Tang, and W. Chen, “Novel approach for 3-D reconstruction of coronary arteries from two uncalibrated angiographic images,” *IEEE Trans. Image Process.*, vol. 18, no. 7, pp. 1563–1572, 2009.

[46] S. Çimen, A. Gooya, M. Grass, and A. F. Frangi, “Reconstruction of coronary arteries from X-ray angiography: A review,” *Medical Image Analysis*, vol. 32. Elsevier B.V., pp. 46–68, 01-Aug-2016.

[47] Z. W. Tang S, Huang J, Hung G, Tsai S, Wang C, Li D, “Dynamic Programming-based Automatic Myocardial Quantification from The Gated SPECT Myocardial Perfusion Imaging - Fully3D2017.” .

[48] R. M. Tayebi *et al.*, “2013 Coronary artery segmentation in angiograms with pattern recognition techniques - A survey,” *Proc. - 2013 Int. Conf. Adv. Comput. Sci. Appl. Technol. ACSAT 2013*, no. June, pp. 321–326, 2013.

[49] “2011 a review of artery segmentation,” p. 300, 1384.

[50] J. C. Bezdek, L. O. Hall, and L. P. Clarke, “Review of MR image segmentation techniques using pattern recognition,” *Med. Phys.*, vol. 20, no. 4, pp. 1033–1048, Jul. 1993.

[51] U. T. V. Nguyen, A. Bhuiyan, L. A. F. Park, and K. Ramamohanarao, “An effective retinal blood vessel segmentation method using multi-scale line detection,” *Pattern Recognit.*, vol. 46, no. 3, pp. 703–715, Mar. 2013.

[52] K. K. Delibasis, A. I. Kechriniotis, C. Tsonos, and N. Assimakis, “Automatic model-based tracing algorithm for vessel segmentation and diameter estimation,” *Comput. Methods Programs Biomed.*, vol. 100, no. 2, pp. 108–122, Nov. 2010.

[53] M. Vlachos and E. Dermatas, “Multi-scale retinal vessel segmentation using line tracking,” *Comput. Med. Imaging Graph.*, vol. 34, no. 3, pp. 213–227, Apr. 2010.

[54] K. Haris, S. N. Efstratiadis, N. Maglaveras, C. Pappas, J. Gourassas, and G. Louridas, “Model-based morphological segmentation and labeling of coronary angiograms,” *IEEE Trans. Med. Imaging*, vol. 18, no. 10, pp. 1003–1015, 1999.

[55] K. Sun, Z. Chen, S. Jiang, and Y. Wang, “Morphological multiscale enhancement, fuzzy filter and watershed for vascular tree extraction in angiogram,” in *Journal of Medical Systems*, 2011, vol. 35, no. 5, pp. 811–824.

[56] M. Ashoorirad and R. Baghbani, “Blood vessel segmentation in angiograms using fuzzy inference system and mathematical morphology,” in *2009 International Conference on Signal Processing Systems, ICSPS 2009*, 2009, pp. 272–276.

[57] A. F. Frangi, W. J. Niessen, K. L. Vincken, and M. A. Viergever, “Multiscale vessel enhancement filtering,” in *Lecture Notes in Computer Science (including*

subseries Lecture Notes in Artificial Intelligence and Lecture Notes in Bioinformatics), 1998, vol. 1496, pp. 130–137.

[58] Z. Zhou, M. M. R. Siddiquee, N. Tajbakhsh, and J. Liang, "UNet++: A Nested U-Net Architecture for Medical Image Segmentation," *Lect. Notes Comput. Sci. (including Subser. Lect. Notes Artif. Intell. Lect. Notes Bioinformatics)*, vol. 11045 LNCS, pp. 3–11, Jul. 2018.

[59] D. P. Kingma and J. L. Ba, "Adam: A method for stochastic optimization," in *3rd International Conference on Learning Representations, ICLR 2015 - Conference Track Proceedings*, 2015.

[60] "A Threshold Selection Method from Gray-Level Histograms - IEEE Journals & Magazine." [Online]. Available: https://ieeexplore.ieee.org/document/4310076. [Accessed: 10-Apr-2020].

[61] C. Anderson, "Computer Vision Methods for Centerline Extraction," 2009.

[62] A. Telea and J. J. Van Wijk, "An Augmented Fast Marching Method for Computing Skeletons and Centerlines," 2002.

[63] Y. H. Ali, "Centerline Extraction : A Review," no. September, 2018.

[64] T. C. Lee, R. L. Kashyap, and C. N. Chu, "Building Skeleton Models via 3-D Medial Surface Axis Thinning Algorithms," *CVGIP Graph. Model. Image Process.*, vol. 56, no. 6, pp. 462–478, Nov. 1994.

[65] T. Y. Kong and A. Rosenfeld, *Topological algorithms for digital image processing*. Elsevier, 1996.

[66] PD Kovesi, "MATLAB and Octave functions for computer vision and image processing." Centre for Exploration Targeting, School of Earth and Environment,

The University of Western Australia, p. 230, 2000.

[67] A. M. Vukicevic, S. Çimen, N. Jagic, G. Jovicic, A. F. Frangi, and N. Filipovic, "Three-dimensional reconstruction and NURBS-based structured meshing of coronary arteries from the conventional X-ray angiography projection images," *Sci. Rep.*, vol. 8, no. 1, pp. 1–20, 2018.

[68] K. Wiesenl *et al.*, "Enhanced 3-D-reconstruction algorithm for C-arm systems suitable for interventional procedures," *IEEE Trans. Med. Imaging*, vol. 19, no. 5, pp. 391–403, May 2000.

[69] W. H. Press, *Numerical recipes : the art of scientific computing*. Cambridge University Press, 2007.

[70] "Forewords | GATE." [Online]. Available: http://www.opengatecollaboration.org/. [Accessed: 17-Apr-2020].

[71] "4D Extended Cardiac-Torso (XCAT) Phantom Version 2.0 – Duke OLV." [Online]. Available: https://olv.duke.edu/technologies/4d-extended-cardiac-torso-xcat-phantom-version-2-0/. [Accessed: 17-Apr-2020].

[72] "Find connected components in binary image - MATLAB bwconncomp - MathWorks Deutschland." [Online]. Available: https://de.mathworks.com/help/images/ref/bwconncomp.html. [Accessed: 08-May-2020].

[73] J. Sanctorum, J. De Beenhouwer, and J. Sijbers, "X-ray Phase-contrast Simulations of Fibrous Phantoms using GATE," in *2018 IEEE Nuclear Science Symposium and Medical Imaging Conference, NSS/MIC 2018 - Proceedings*, 2018.

[74] Philip Kollmannsberger, "Skeleton3D - File Exchange - MATLAB Central."

[Online]. Available: https://de.mathworks.com/matlabcentral/fileexchange/43400-skeleton3d. [Accessed: 12-Apr-2020].

[75] "Three-dimensional displays of left ventricular epicardial surface from standard cardiac SPECT perfusion quantification techniques. - PubMed - NCBI." [Online]. Available: https://www.ncbi.nlm.nih.gov/pubmed/7699467. [Accessed: 23-Mar-2020].

[76] N. P. Johnson and K. L. Gould, "Integrating noninvasive absolute flow, coronary flow reserve, and ischemic thresholds into a comprehensive map of physiological severity," *JACC Cardiovasc. Imaging*, vol. 5, no. 4, pp. 430–440, 2012.

[77] G. Germano *et al.*, "Automatic quantification of ejection fraction from gated myocardial perfusion SPECT," *J. Nucl. Med.*, vol. 36, no. 11, pp. 2138–2147, 1995.

[78] Z. W. Tang S, Huang J, Hung G, Tsai S, Wang C, Li D, "Dynamic Programming-based Automatic Myocardial Quantification from The Gated SPECT Myocardial Perfusion Imaging - Google Search," 2017. .

[79] "Dirk-Jan Kroon (2020). Smooth Triangulated Mesh (https://www.mathworks.com/matlabcentral/fileexchange/26710-smooth-triangulated-mesh), MATLAB Central File Exchange. Retrieved June 15, 2020." .

[80] "villekf/OMEGA: Open-source MATLAB Emission Tomography Software." [Online]. Available: https://github.com/villekf/OMEGA. [Accessed: 08-Apr-2020].

[81] I. W. Selesnick and C. Sidney Burrus, "Generalized digital butterworth filter design," *IEEE Trans. Signal Process.*, vol. 46, no. 6, pp. 1688–1694, 1998.

[82] “Image Segmentation - MATLAB & Simulink.” [Online]. Available: https://de.mathworks.com/discovery/image-segmentation.html. [Accessed: 08-Apr-2020].

[83] T. L. Faber *et al.*, “Three-dimensional fusion of coronary arteries with myocardial perfusion distributions: clinical validation.,” *J. Nucl. Med.*, vol. 45, no. 5, pp. 745–53, May 2004.

[84] Shihui Ying, Jigen Peng, Shaoyi Du, and Hong Qiao, “A Scale Stretch Method Based on ICP for 3D Data Registration,” *IEEE Trans. Autom. Sci. Eng.*, vol. 6, no. 3, pp. 559–565, Jul. 2009.

[85] H. Tang, R. M. Bober, C. Zhang, Z. He, J. Zou, and W. Zhou, “Scale ratio ICP for 3D registration of coronary venous anatomy with left ventricular epicardial surface to guide CRT lead placement,” in *Medical Imaging 2019: Image-Guided Procedures, Robotic Interventions, and Modeling*, 2019, vol. 10951, p. 75.

[86] “Nearest point search - MATLAB dsearchn - MathWorks Deutschland.” [Online]. Available: https://de.mathworks.com/help/matlab/ref/dsearchn.html. [Accessed: 23-Apr-2020].

[87] S. Du, N. Zheng, L. Xiong, S. Ying, and J. Xue, “Scaling iterative closest point algorithm for registration of m-D point sets,” *J. Vis. Commun. Image Represent.*, vol. 21, no. 5–6, pp. 442–452, 2010.

[88] K. S. Arun, T. S. Huang, and S. D. Blostein, “Least-Squares Fitting of Two 3-D Point Sets,” *IEEE Trans. Pattern Anal. Mach. Intell.*, vol. PAMI-9, no. 5, pp. 698–700, Sep. 1987.

[89] “Download | ParaView.” [Online]. Available:

https://www.paraview.org/download/. [Accessed: 06-May-2020].

[90] U. Ayachit, *The ParaView guide : [a parallel visualization application] ; updated for ParaView version 4.3*. Kitware, 2015.

[91] "3D Slicer." [Online]. Available: https://www.slicer.org/. [Accessed: 13-Apr-2020].

[92] M. D. Cerqueira *et al.*, "Standardized myocardial sementation and nomenclature for tomographic imaging of the heart: A Statement for Healthcare Professionals from the Cardiac Imaging Committee of the Council on Clinical Cardiology of the American Heart Association," *Circulation*, vol. 105, no. 4. Lippincott Williams & Wilkins, pp. 539–542, 29-Jan-2002.

[93] "Abstract 15074: Application of the AHA 17 Segment Model: Evaluation of Relative Segmental Mass of the Left Ventricle by Cardiac MRI | Circulation." [Online]. Available: https://www.ahajournals.org/doi/10.1161/circ.126.suppl_21.A15074. [Accessed: 08-May-2020].

[94] S. Pasupathy, R. Tavella, and J. F. Beltrame, "Myocardial Infarction with Nonobstructive Coronary Arteries (MINOCA): The Past, Present, and Future Management," *Circulation*, vol. 135, no. 16. Lippincott Williams and Wilkins, pp. 1490–1493, 18-Apr-2017.